System Design, Fabrication, and Characterization of Thermoelectric and Thermal Interface Materials for Thermoelectric Devices

Jue Wang

Dissertation submitted to the faculty of the Virginia Polytechnic Institute and State University in partial fulfillment of the requirements for the degree of

Doctor of Philosophy

In

Mechanical Engineering

Scott T. Huxtable, Chair

Jiangtao Cheng

Srinath Ekkad

Mitsuhiro Murayama

Mark R. Paul

May 4th, 2018

Blacksburg, VA

Keywords: System design, material characterization, thermal interface conductance, thermoelectric, Seebeck, electrical resistivity

System Design, Fabrication, and Characterization of Thermoelectric and Thermal Interface Materials for Thermoelectric Devices

Jue Wang

Abstract

Thermoelectric devices are useful for a variety of applications due to their ability to either convert heat directly into electricity, or to generate a temperature gradient from an electric current. These devices offer several attractive features including compact size, no moving parts, limited maintenance requirements, and high reliability. Thus thermoelectric devices are used for temperature-control, cooling, or power generation in various industrial systems such as automobiles, avionics, refrigerators, chillers, laser diodes, dehumidifiers, and a variety of sensors. In order to improve the efficiency of thermoelectric devices, many endeavors have been made to design and fabricate materials with a higher dimensionless thermoelectric figure of merit (*ZT*), as well as to optimize the device structure and packaging to manage heat more effectively. When evaluating candidate thermoelectric materials, one must accurately characterize the electrical conductivity, thermal conductivity, and the Seebeck coefficient over the temperature range of potential use. However, despite considerable research on thermoelectric materials for decades, there is still significant scatter and disagreement in the literature regarding accurate characterization of these properties due to inherent difficulties in

the measurements such as requirements for precise control of temperature, simultaneous evaluation of voltage and temperature, etc. Thus, a well-designed and well-calibrated thermoelectric measurement system that can meet the requirements needed for multiple kinds of thermoelectric materials is an essential tool for the development of advanced thermoelectric devices.

In this dissertation, I discuss the design, fabrication, and validation of a measurement system that can rapidly and accurately evaluate the Seebeck coefficient and electrical resistivity of thermoelectric materials of various shapes and sizes from room temperature up to 600 K. The methodology for the Seebeck coefficient and electrical resistivity measurements is examined along with the optimization and application of both in the measurement system. The calibration process is completed by a standard thermoelectric material and several other materials, which demonstrates the accuracy and reliability of the system.

While a great deal of prior research has focused on low temperature thermoelectric materials for cooling, such as Bi_2Te_3, high temperature thermoelectric materials are receiving increasing attention for power generation. With the addition of commercial systems for the Seebeck coefficient, electrical resistivity, and thermal conductivity measurements to expand the temperature range for evaluation, a wide range of materials can be studied and characterized. Chapter Two of this dissertation describes the physical properties characterization of a variety of thermoelectric materials, including room temperature materials such as $Bi_{0.5}Sb_{1.5}Te_3$, medium temperature level materials such as skutterudites, and materials for high temperature

applications such as half-Heusler alloys. In addition, I discuss the characterization of unique oxide thermoelectric materials, which are Al doped ZnO and Ca-Co-O systems for high temperature applications.

Chapter Four of this dissertation addresses the use of GaSn alloys as a thermal interface material (TIM), to improve thermal transport between thermoelectric devices and heat sinks for power generation applications at high temperature. I discuss the mechanical and thermal behavior of GaSn as an interface material between electrically insulating AlN and Inconel heat exchangers at temperatures up to 600 °C. Additionally, a theoretical model for the experimental thermal performances of the GaSn interface layer is also examined.

System design, Fabrication, and Characterization of Thermoelectric and Thermal Interface Materials for Thermoelectric Devices

Jue Wang

General Audience Abstract

Thermoelectric materials can directly convert heat into electricity for power generation, or they can be used for cooling or refrigeration applications when supplied with electric power. This dissertation primarily focuses on the evaluation of materials used in thermoelectric generators (TEGs). Specifically, Chapter Two of this work describes the design, development, and validation of a developed measurement system that can evaluate two important properties, the Seebeck coefficient and electrical resistivity, for a variety of thermoelectric materials. Next, Chapter Three discusses the work using other commercial measurement systems to evaluate several types of thermoelectric materials, including Bi_2Te_3 based materials, skutterudites, half-Heusler alloys, ZnO, and Ca-Co-O for a TEG module. Finally, I discuss the use of GaSn, a liquid metal alloy, as a thermal interface material to improve heat transport between dissimilar materials for TEGs. The GaSn was applied between a thermoelectric device and a heat exchanger for use in energy harvesting devices. The mechanical robustness and thermal reliability were tested, and the GaSn was shown to improve thermal performances both in experiments and through modeling.

Dedications

To beloved family members

Acknowledgements

First of all, I would like to express my deepest gratitude to my advisor Prof. Scott T Huxtable. Without his patient guidance, warm encouragement, kind support and great responsibility, I will remain to be a boy who wants to knock the door of research but has no idea of the right path. I feel extremely blessed to have him as my advisor in my PhD study. His profound knowledge, consistency and responsible attitude towards research and teaching give me lessons not only in academics, but also have had great impacts in my personal life. I would like to thank him for guiding me into the path of research and the path of pursuing perfection as well. His humbleness, kindness and rigorous scientific guidance will be my great example in the future.

I would also to express my appreciation to my committee members Dr. Jiangtao Cheng, Dr. Srinath Ekkad, Dr. Mitsuhiro Murayama, and Dr. Mark Paul for their time, insightful suggestions and warm encouragements during my PhD study. Also, I want to thank my previous committee member Dr. Francine Battaglia for serving on my committee for several years and to Dr. Shashank Priya for his continuous support.

I would like to thank Dr. Hao-Hsiang Liao, my great colleague and friend in both research and life; Dr. Yu (Grace) Zhao, a wonderful collaborator who is always motivated; Dr. Wenjie Li, a great friend and collaborator who is very creative; Dr. Ge Nie, the first one who always will give you great advice. I would also like to thank my colleagues and friends Heonjoong Lee, Myung-Eun Song, Han-Byul Kang, Dr. Harikrishna, Ashwath Kumar, Fan Gao, Long He,

Lei Zhao, Hao Ma, and Xiaofan Li. I would also bring my special thanks to Donald Leber, who instructed me a lot in both the cleanroom facilities and in the vacuum science fields, and Beth Howell, who was always helpful to me in many areas.

Most importantly, I would like to express my sincerest gratitude to my parents, Jiasheng Wang and Qing Wei, and my fiancée Yincan Mao. Without their support and love, I could not keep moving forward with gratitude and love in all these years.

Table of Contents

List of Figures

List of Tables

Chapter 1 Introduction

1.1 Background

Thermoelectric (TE) devices have the ability to directly convert thermal energy into electricity as a heat engine, or they can consume electricity to generate cooling. With increasing demands for improved energy efficiency in numerous applications, such as automobiles, power plants, thermal management of power electronics, etc. Thermoelectric devices, and the related semiconductor materials used in thermoelectric devices, have attracted significant research attention in recent years.

At the present time, thermoelectric cooling devices are already widely used in electronic devices for thermal management[1]. Compared to conventional vapor compression cooling devices, thermoelectric coolers enjoy some advantageous characteristics in that they are compact in size, light in weight, have no mechanical moving parts and no requirements for working fluids. In addition, from a more systematic point of view, since thermoelectric coolers are powered with direct current, they are able to quickly switch between cooling and heating capabilities, thus allowing for flexibility in precise temperature control applications.

In addition to cooling applications, thermoelectric devices can also function as power generators in energy harvesting applications as well. For example, in all combustion engines, a large fraction of the input chemical energy is ultimately rejected as waste heat, thus there are opportunities for thermoelectric devices to capture some of this otherwise wasted energy and to convert a fraction of that energy into useful work. For example, roughly 30% of the chemical

energy in gasoline or diesel fuels that are used in internal combustion engines is ultimately wasted as hot exhaust gas[2]. Several groups have shown that thermoelectric generators can convert some of the energy in the hot exhaust gas in vehicles into useful electrical work that could then be used to improve fuel economy and to reduce harmful exhaust emissions[3]–[6]. At another scale, small thermoelectric generators can be used to harvest waste heat from the environment or any number of industrial sources in order to provide electric power to a variety of sensors, thus eliminating the need for wiring or batteries. Thermoelectric technology and related devices bring another solution for energy production, with great reliability and scalability.

Thermoelectric power generators operate on the Seebeck effect of thermoelectric material. In a piece of thermoelectric (TE) material, free electrons or holes act as both charge and heat carriers[7]. If a temperature gradient is applied to a properly configured TE couple consisting of n-type (electron carrier) and p-type (hole carrier) elements, these carriers tend to diffuse to the cold end, resulting in an electrostatic potential. This phenomenon is defined as the Seebeck effect as shown in Figure 1-1. The Seebeck effect was discovered and subsequently named after Thomas Johann Seebeck, who discovered the effect in 1821[8]. On the other hand, by driving a current through a junction between conductors, heat may be generated or removed at the junction since heat is also carried by each charge. This effect is called the Peltier effect[9]. In this dissertation, I will mostly focus on applications that are based on the Seebeck effect, where thermal gradients are used for converting thermal energy into electricity.

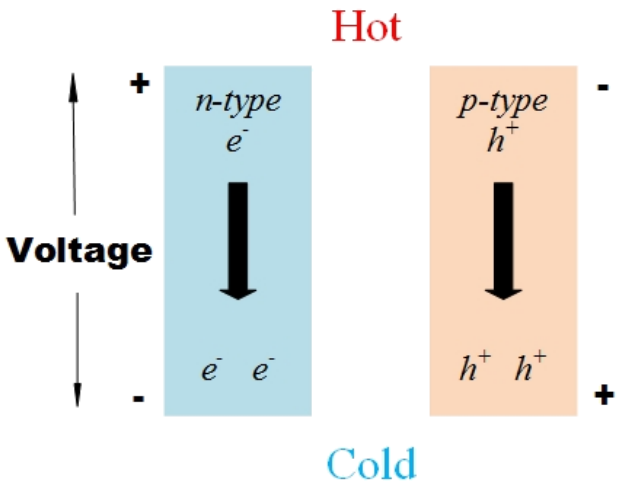

Figure 1-1 In thermoelectric materials under a temperature gradient, charge carriers (electrons or holes) move to the cold side due to heat flow, which leads to an electric current under a closed loop circuit.

The ability for a material to generate a voltage based on an imposed temperature gradient is quantified by the Seebeck coefficient, S, which is defined as $S = \Delta V/\Delta T$, where ΔV is the voltage difference and ΔT is the temperature gradient across the material. The most straightforward way to measure the Seebeck coefficient of a certain material, A, is to impose a temperature gradient across the material, and to then simultaneously measure the temperature difference and voltage generated across material A. A schematic example of this measurement using a separate material, B, to make the connections to A is shown in Figure 1-2. Similarly, if the Seebeck coefficients of the materials, A and B, are known and the voltage is measured in the same experimental setup, the absolute temperature of one end (either hot or cold) of material A can be obtained if the temperature of the other end is known. This is the working principle of a thermocouple.

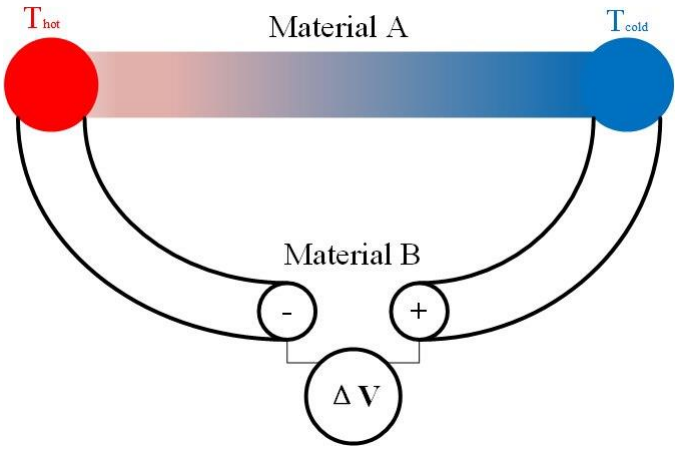

Figure 1-2 The Seebeck effect for two dissimilar materials A and B. When a temperature gradient (T_{hot} and T_{cold}) is developed across material A, a proportional voltage is generated.

The Seebeck coefficient is a parameter that only determines the magnitude of the voltage developed when the material possess a certain temperature difference. A dimensionless thermoelectric figure of merit, *ZT,* on the other hand, is a parameter used to quantify the thermoelectric material efficiency of converting heat into electricity directly. The dimensionless figure of merit is defined as

$$ZT = \frac{S^2\sigma}{k}T \quad , \tag{1-1}$$

where S is the Seebeck coefficient, σ is the electrical conductivity, κ is the thermal conductivity, and T is absolute temperature. To achieve a higher *ZT,* a large Seebeck coefficient with high electrical conductivity, and low thermal conductivity are therefore necessary conditions.

1.2 Measurement technique for thermoelectric material characterization

To characterize a certain type of thermoelectric material, the accurate measurement of the aforementioned properties are critical. These property measurements require a stable, repeatable and accurate measurement system capable of operating over a wide temperature range. However, despite significant interest in thermoelectric materials, there are many subtleties involved with performing accurate measurements. In order to properly evaluate new thermoelectric materials and to ultimately incorporate more efficient thermoelectric materials into modules and devices, accurate knowledge of transport properties, including orientation-dependent variations, across the full working temperature range are critical. While there are many factors responsible for the difficulties in property measurements, some of the the primary reasons for the unreliable transport property measurements are given below [10]:

Material nonuniformity: Due to different techniques for measuring electrical and thermal properties, these properties are often not measured in the same orientation. For example, many thermal conductivity measurements are performed in the direction normal to a sample surface, while the electrical conductivity measurements are often done in the direction parallel with the surface. These differences sometimes lead to great error in the evaluation of *ZT*, especially for anisotropic samples such as the Bi_2Te_3 and $Ca_3Co_4O_9$ families of thermoelectric materials. Yan *et al.* [11] studied the enhanced thermoelectric properties in the *ab* plane of single crystals, acquiring both higher power factor and thermal conductivity across the *ab* plane. Tang *et al.*[12] reported the anisotropic thermopower in a misfit-layered calcium cobaltite. Generally, since

many thermoelectric materials share a similar lamellar structure, the anisotropy in physical properties are quite common.

Unrealistic extrapolation: The limitation of experimental design will place bounds on the measured temperature range for some materials such as half-Heusler alloys. Projections of low-temperature and room temperature data to high temperatures are often not valid beyond the measurement capabilities. Furthermore, calibration and validation is often done at room temperature, or over a small temperature range. While these measurements are useful, one cannot guarantee that the measurement systems will remain accurate outside of these limited temperature ranges. Lying in the foundation of continuity of all three (electrical conductivity, thermal conductivity, and Seebeck coefficient) transport properties, application of extrapolation is a helpful tool to find properties at certain conditions. However, a complete temperature dependent measurement curve consists of several measurement points, whose number will be limited by the resolution of measurement units and measurement time cost. In some cases of measurement practice, the theoretical maximum value of the figure of merit *ZT* will be more sensitive to temperature variations around the target temperature point, which will be limited by the accuracy of interpolation.

Lack of standard reference materials and test procedures: The measurement errors and system mistakes are not recognized especially in the calculation of *ZT.* Lowhorn *et al.* [13] developed a Seebeck coefficient standard reference material from the temperature range of 10 K to 390 K, covering the need for reference material in the low to medium temperature range.

However, for power generation, the temperatures of interest are often well above 400 K, where validated standard materials are still lacking. Martin *et al.* [14] discussed several key points that need to be followed in thermoelectric measurements, and they compared the principles of various measurement methods. However, tradeoffs between measurement accuracy, ability to measure various materials of differing shapes and sizes, etc. are still under debate.

To better explain the details and accuracy of measurements of *ZT*, the principles of accurate thermoelectric property measurements are essential to be understood first. Ideally, all three transport properties, the Seebeck coefficient, electrical conductivity, and thermal conductivity, should be measured at the same temperature, and at the same locations and in the same directions on the sample, to overcome possible nonuniformities in sample itself. For the evaluation of *ZT,* the Seebeck coefficient plays an important role as this value is squared in the expression of figure of merit. Seebeck measurements are simple in theory, as one only needs to accurately measure temperature and voltage simultaneously on a sample. However, in practice, the measurements are notoriously difficult to perform accurately, especially in the high temperature range. To obtain a Seebeck coefficient with great accuracy and repeatability, a stable measurement environment with powerful heating elements needs to be created, eliminating as many thermal and electrical fluctuations and noise from the outside as possible. Then, since many thermoelectric samples are easily oxidized during the heating process, a protective, constant atmosphere of an inert gas or vacuum status is also necessary, while functioning as a supplementary way to reduce the possibility of introducing external error from the environment as well. Last, but not the least, two separate systems for environmental control

and data acquisition are required in order to ensure repeatability. The temperature feedback and control systems are designed to detect any temperature changes and then modify the heater output through an automated process to reduce manual labor and minimize human error. On the other hand, the data acquisition system serves as the brain of the whole measurement setup. It will complete the function of sampling data at designed temperature points, collecting and recording the measured properties, completing calculations and then transferring them into real-time curves as needed. The combination of all of these three systems would satisfy the basic measurement needs, but the compatibility of the overall setup will dictate the quality of the overall measurement process and therefore the accuracy of data.

For design of our custom-made experimental measurement system, all of these three systems are expressed in a block diagram as shown in Figure 1-3. Each assembly functions independently but works simultaneously, controlled by the main program written in LabVIEW. Also, each individual function unit will follow the instructions of a subroutine (called a Virtual Instrument, or sub-VI) so that all condition parameters and measured data will be stored and displayed.

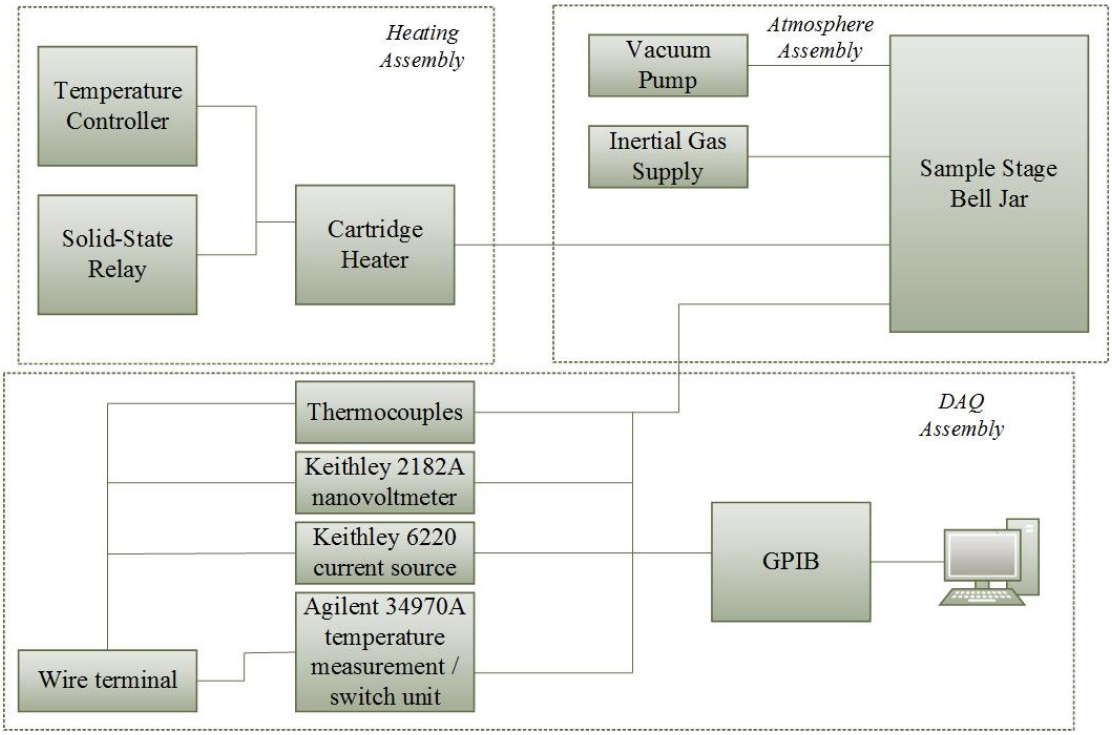

Figure 1-3 Block diagram of a custom-made experimental system for Seebeck coefficient and electrical conductivity measurements. The integration of a commercially available and easy to assemble measurement unit and self-designed components reduced the complexity of the overall system while also limiting the assembly costs.

A key point in the design of this overall system is the versatility and flexibility of each individual component. The block diagram in Figure 1-3 only presents the theoretical blueprint of what parts are necessary in the measurement system. Figure 1-4 displays the actual components in the real setup except for the connection wires/ports between different units. This design, consisting of customized self-made parts and commercially available units, is easily modifiable and it has flexibility for possible upgrades.

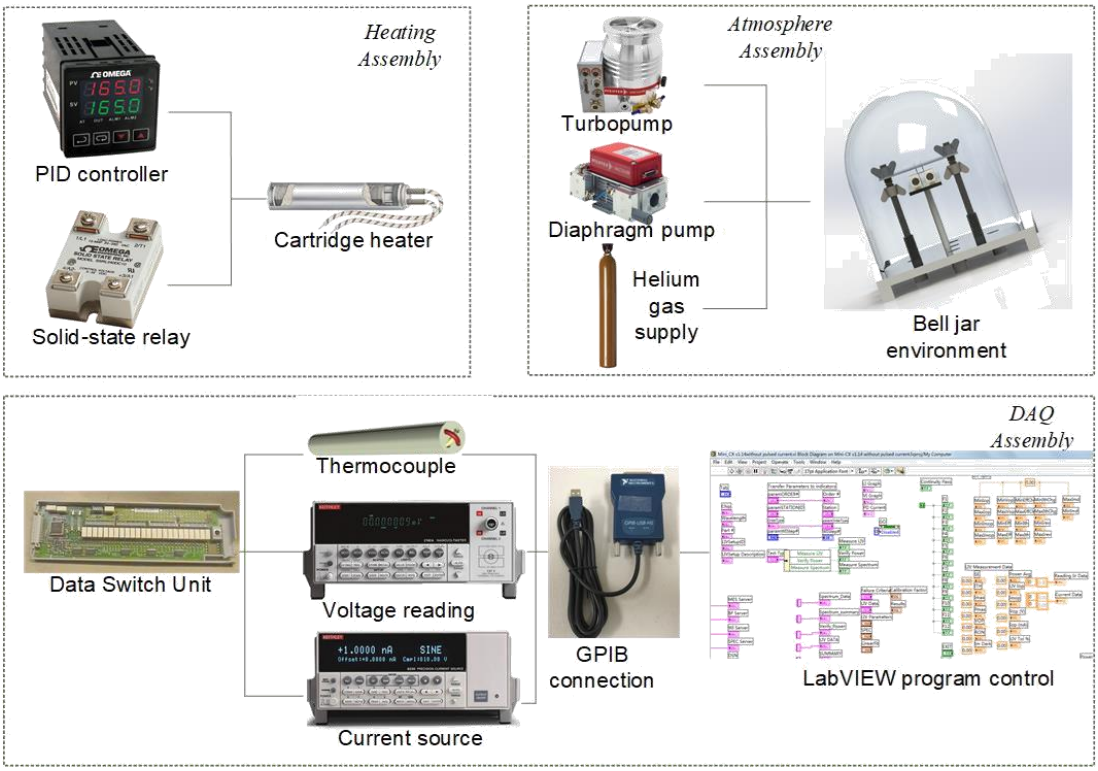

Figure 1-4 Actual systems used for the Seebeck coefficient and electrical conductivity measurement apparatus.

Several commercially available experimental systems have been designed for the measurement of thermoelectric properties of materials. The two mostly widely used commercial thermoelectric characterization systems are: the ZEM series of systems developed by ULVAC and the SBA series from Netzsch. Both of these commercial systems possess a broader measurement temperature range and an improved controlled atmosphere vessel due to the delicate design of heating chamber as compared to the new system described here. On the other hand, the self-built system, differs from the commercial systems in the design target, as the new system provides greater flexibility for measuring samples of different shapes or dimensions (as are often produced in basic research), while the commercial systems require

that samples are generally long bars with rectangular cross-section. Thus, while the new system is limited in the measurement temperature range, it can be used as a great supplementary measurement tool, where it provides rapid and inexpensive measurements for an initial evaluation of newly developed materials that are made from various fabrication techniques that produce samples of a variety of shapes and sizes. In addition, the possibility of future upgrades to the heating chamber and improved vacuum and venting devices, for more solid environment control, makes it possible to improve the measurement capabilities of the new system.

A primary concern with the design of the experimental setup is to overcome the difficulty in making accurate thermoelectric measurements on samples of various geometries. The research into thermoelectric materials range from a variety element with dramatic differences in mechanical properties, especially in strength. Typical thermoelectric materials behave like heavily doped semiconductors[15] and after post synthesis processing such as ball milling, hot pressing, spark plasma sintering and post-annealing, several secondary phases or other modifications could greatly change the mechanical properties of the materials. So after the all these material-processing processes, the prepared samples may possess varying shapes, sizes, hardness, etc. However, for all of the commercial measurement systems, including the ZEM series, Netzsch Nemesis system and laser flash diffusivity measurement equipment; they all require samples of certain dimensions, typically a disk shape within a certain thickness range (for laser flash thermal diffusivity measurements) or the samples must be long bar shapes (for Seebeck coefficient and electrical conductivity measurements) with certain cross sections in order to fulfill solid thermal and electrical contacts onto the designed sample holder.

Post-processing to change the shape of post-annealed samples requires significant manual work, often involving a great deal of waste of the original sintered samples, and may result in sample breakage or surface re-hardening during cutting and polishing processes, making the following procedure of reshaping more difficult. Moreover, for most lab-fabricated thermoelectric materials, since heavy doping is often not well controlled, the homogeneity in raw rod samples is uncertain. As a result, the final product of a ready-to-measure sample may not accurately reflect the general doping distribution of the sintering process, which means in real practice, even for samples made in the same batch, the measured thermoelectric properties may vary due to the cutting, polishing, or other reshaping processes. In order to overcome these challenges, the designed Seebeck and electrical conductivity system should adapt to the dimensional requirements of the laser flash system, which requires thin, disk shaped, samples, while not sacrificing significant accuracy. Figure 1-5 shows several comparisons of multiple commonly used geometries in measurement systems.

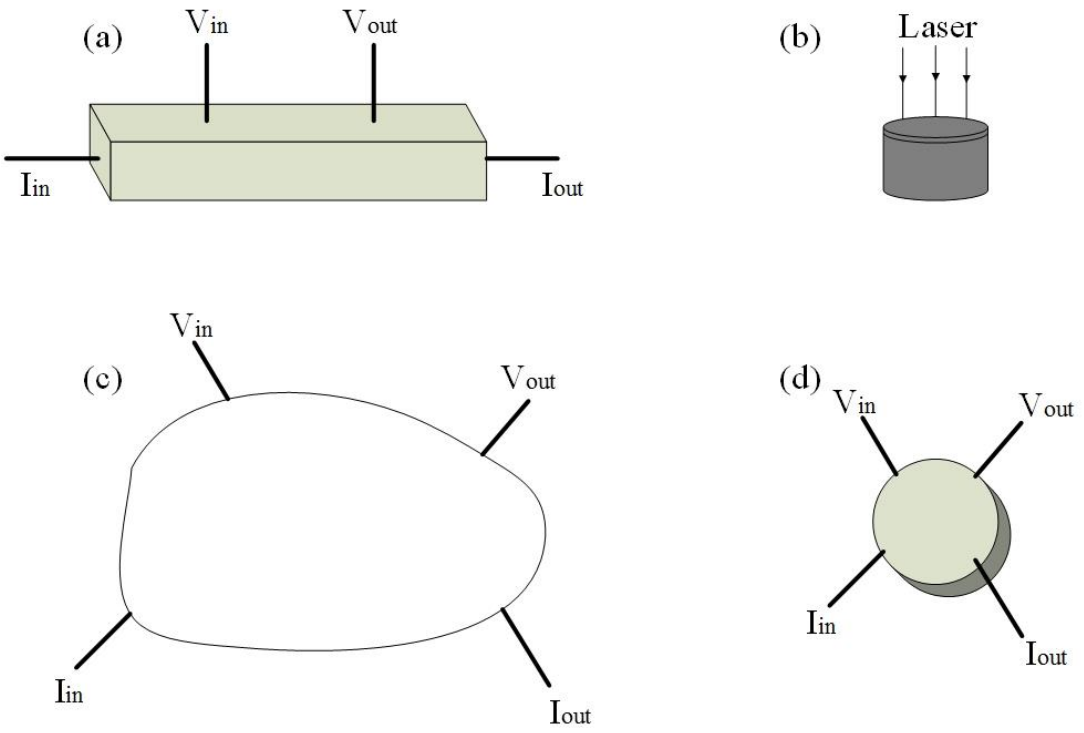

Figure 1-5 Common sample geometries. (a) Preferred geometry for four-probe electrical conductivity measurements, (b) typical sample geometry for a laser flash diffusivity measurement, (c) arbitrarily shaped lamella for van der Pauw measurement showing contact locations at the edge of the sample for electrical conductivity measurements, and (d) designed geometry for my experimental setup.

Besides the reduction in manual labor and limiting the waste of materials introduced by modifying the sample size, another significant benefit of using the new system is the confirmation of measured properties all having the same orientation. Early in 1961, Dennis[16] discussed the anisotropy of the Seebeck coefficient of Bi_2Te_3 theoretically and experimentally around room temperature. Yan *et al.*[11] expanded the experimental studies on anisotropic behavior of Bi-Te-Se samples fabricated by hot pressing. In order to prepare samples along the cleavage planes (perpendicular to the *c*-axis), they had to prepare the bulk material in a larger

diameter die with increased thickness, and they applied higher temperature to confirm that lateral flow of the small grains took place at certain orientations. Shelimova *et al.*[17] studied the anisotropic thermoelectric properties of the layered compounds in PbTe families as well. They showed that the thermal conductivities measured along the *a*-axis and the *c*-axis can differ by a factor of up to 3.8 times. However, due to the limitations of the dimensions of dies for hot-pressing and spark plasma sintering machines, it takes much more effort to produce samples for each type of measurement with the same orientation. By applying the van der Pauw measurement method, one can avoid the mistakes from the orientation of the measurement to provide a more reliable figure of merit value. The details of the design, fabrication and calibration process are discussed in the second section of this dissertation.

1.3 Characterization of high figure of merit thermoelectric materials

With the equipment of both self-designed thermoelectric characterization system and commercial Seebeck and electrical conductivity measurement unit, the full capabilities of characterization thermoelectric materials is achieved. As noted previously, thermoelectric materials and devices are already in commercial use in many applications. Different types of thermoelectric materials find applications ranging from powering small mW level sensors, to producing kW level waste heat recovery in automobiles and transportation industries, to potentially generating MW level power in power plant applications. Additionally, thermoelectric generators find many niche applications such as producing electrical power

module in space exploration, as radioisotope thermoelectric generators are essentially the only viable option in deep space environments where solar radiation is limited. However, despite the range of applications for power generation, the use of thermoelectric devices for cooling is much more widespread than for power generation due to the limitation of relatively low thermoelectric generator efficiency. Hu *et al.*[5] have demonstrated that a nanostructured PbTe-based module and segmented Bi_2Te_3/nanostructured PbTe module can have a maximum energy conversion efficiency around 11%. This is a remarkable value for thermoelectric generators, although it is far from the typical thermal efficiency of internal combustion engines of around 30%.

For a thermoelectric generator that produces electric power directly from a temperature gradient, the maximum thermal efficiency depends on the material's dimensionless figure of merit *ZT* as

$$\eta_{\max} = \frac{\Delta T}{T_h} \frac{\sqrt{1+ZT_{ave}}-1}{\sqrt{1+ZT_{ave}}+\frac{T_c}{T_h}} . \tag{1-2}$$

In this relation, T_c and T_h are cold and hot side temperatures, respectively, and ΔT is their difference. In addition, ZT_{ave} is the average figure of merit, *ZT*, of both the *p*-type and *n*-type thermoelectric materials. Since the temperatures are dictated by the environment in which the generator operates, the key to increases the thermal efficiency lies in maximizing the of figure of merit *ZT*.

According to the expression of figure of merit, *ZT,* in equation (1-1), the Seebeck coefficient will play an important role since this property is squared in the numerator. Consequently, many methods, including high energy ball milling, spark plasma sintering, cold isostatic pressing, have been examined to produce raw material with a greater density and larger Seebeck coefficient. However, methods to increase the Seebeck coefficient have the undesirable effect of also reducing electrical conductivity and vice-versa. In order to compensate for the side effects brought by the densification, more endeavors are needed to improve the value of *ZT* using additional techniques such as extra ion doping, nanoengineering, alloying, etc. in order to increase the value of Seebeck coefficient while maintaining a high electrical conductivity and a low thermal conductivity.

In the view of preserving a high electrical conductivity while keeping the thermal conductivity relatively low, the mechanisms that control thermal transport need to be clarified. Electrons and quantized lattice vibrations called phonons carry thermal energy in solids. At the nanoscale, both electrons and phonons are affected by the size of grains, boundary surfaces, and different phases as the mean free path or wavelength of these carriers is comparable to the size of the grains, etc. The total thermal conductivity, *k,* consists of the electronic contribution, k_e, and phonon contribution, k_p, separately as

$$k = k_e + k_p . \tag{1-3}$$

Since the total thermal conductivity results from the combination of two different carriers, one of which is electrons, it can be understood that materials with high electrical conductivity, such as metals, will also have high thermal conductivity, as the electrons are carriers for both heat and electricity. On the other hand, thermally insulating materials, whose carriers are mainly phonons, suffer from low electrical conductivity. All of these characteristics make semiconductor families are the most promising candidates for thermoelectric materials. Although some oxide thermoelectric materials are interesting for some applications at high temperature where resistance to oxidation is important, the majority of potential thermoelectric materials are from the semiconductor family.

As mentioned above, the benefit of using semiconductors is they can transport electricity as conductors while acting as near insulators thermally, thus improving the figure of merit, *ZT,* naturally. Typical semiconductor elements in the periodic table are from groups 13-15 as aluminum (Al), gallium (Ga) and indium (In), *et al.* are from group 13 and antimony (Sb), bismuth (Bi) are from group 15. Other intermediate elements as selenide and tellurium are also commonly used in alloys for thermoelectric materials. Although many families of materials show great potential for thermoelectric generator applications in a wide temperature range, from room temperature up to around 800 K, this dissertation will focus on three families of materials: bismuth telluride (BiTe), skutterudites (cobalt arsenide, $CoAs_3$), and half-Heusler alloys (XYZ, X and Y transition metals and Z as a p-block materials). These materials cover applications across a range of temperatures from low temperature cooling and power

generation (room temperature to 400 K), mid-range energy harvesting (400 K to 600 K) and high temperature (above 600 K) waste heat recovery.

Poudel *et al.*[18] successfully fabricated a monocrystalline P-type bismuth antimony telluride bulk alloy with a significant reduction in thermal conductivity, leading to a landmark *ZT* value of about 1.4 at a temperature around 375 K. This material was processed by mechanical milling of a commercial ingot into a nano-powder that was subsequently consolidated by hot pressing. Cao *et al.*[19] obtained a maximum *ZT* of 1.47 at 438 K for Bi_2Te_3/Sb_2Te_3 bulk nanocomposites with laminated nanostructures by hydrothermal synthesis and hot pressing. Some other efforts to improve *ZT* also involve inclusions of Bi_2Te_3, which leads to great enhancement. Wu[20] showed that another remarkably high ZT value of ~1.9 can be achieved at 773 K in $Ge_{0.87}Pb_{0.18}Te$ upon the introduction of 3 mol% Bi_2Te_3 since it promotes the solubility of PbTe in the GeTe matrix. In this dissertation, I will present some studies that examine the increase the figure of merit *ZT* through the use of excess of Te in Bi-Sb-Te compositions.

Considerable efforts have been made in producing high figure of merit skutterudite materials as well. Besides the traditional structure of $CoAs_3$, a more complex binary structure with a general chemical formula of MX_3 is a broader view of skutterudites, where M is the transition-metal cobalt (Co), rhodium (Rh) or iridium (Ir), and X is phosphorus (P), arsenic (As) or antimony (Sb). The lattice structure makes it possible to cage a small metal atom in the center of a unit cell, thus having the effect of scattering phonons to reduce thermal conductivity.

Shi *et al.*[21] proved that skutterudites of $CoSb_3$ with multiple co-fillers of Ba, La, and Yb could be synthesized and a high *ZT* ~1.7 at 850 K was realized. In practice, high power factors were achieved by adjusting the total filling fraction of fillers with different charge states to optimize carrier density, while the thermal conductivity was significantly reduced through combining filler species of different rattling frequencies to achieve a wide frequency range for phonon scattering. Wang *et al.*[6] systemically examined the filling fraction limit of skutterudites to reach a maximum *ZT* of 1.5 at 850 K for a composition of $Yb_{0.3}Co_4Sb_{12}$. Not only was the maximum *ZT* investigated, but a large average *ZT* of ~1.05 from 300-850 K was achieved as well. Another significant effort came from the research of Rogl *et al.*[22] as they found that a composition of $(R_{0.25}Ba_{0.25}Yb_{0.5})_{0.5}Co_4Sb_{12.5}$ reaches a remarkable *ZT* of 1.9 after severe plastic deformation via high-pressure torsion. Though debates still exist regarding the reproductively and accuracy for some *ZT* values found in the literature, it can be confirmed that the figure of merit was greatly improved in skutterudite thermoelectric materials. In this dissertation, I will discuss some collaborative work regarding the investigation of the filling fraction limitation in *n*-type $CoSb_3$ skutterudites to improve figure of merit.

Compared to skutterudites, half-Heusler alloys stand out not only for their high *ZT* values, but also for being relatively environmentally benign as they do not use many traditional, but harmful, thermoelectric elements such as lead (Pb) while maintaining low cost materials as magnesium (Mg), nickel (Ni) and tin (Sn) [23]. Yu *et al.*[24] synthesized a composition of $Hf_{0.6}Zr_{0.4}NiSn_{0.98}Sb_{0.02}$ to reach a *ZT* value of 1.0 at 1000 K due to the small amount of Sb doping that increases the power factor, while levitation melting and spark plasma sintering

prevented compositional segregations. Xie *et al.*[25] studied the Sb doping in ZrNiSn system and reached maximum *ZT* of 0.8 at 875 K using a composition of $ZrNiSn_{0.99}Sb_{0.01}$. I will present some research about the use of nano-inclusions added to half-Heusler alloys and the subsequent improvement in thermoelectric properties.

As mentioned before, semiconductor families of thermoelectric materials generally show a higher figure of merit, with more possibilities to merge into applications of energy harvesting. But in real applications, thermoelectric modules sometimes work under arduous conditions as with typical characteristics of high-temperatures, great thermal stress, and exposure to air causing oxidation and corrosion. All of these factors will harm the efficiency and lifespan of real thermoelectric devices, causing a decrease in power output and, ultimately, even a failure of the devices. Unfortunately, all of the semiconductor thermoelectric materials fail to resist oxidation in real applications. Not only will the exposure to air slowly oxidize the surface of material, but also the overall electrical contacts will be greatly deteriorated due to oxidation, which reduces the device performance and lifetime. In order to overcome the oxidation related shortcomings of typical semiconductors, a variety of other types of thermoelectric materials have been developed and one great representative is the oxide material family. Different from vulnerable semiconductor materials in an oxidation environment, oxides naturally prevent further oxidation due to their composition thus avoiding degradation. I will also illustrate some recent research about oxide thermoelectric materials, presenting some approaches to increase its figure of merit including the example of nanoinclusion doped calcium cobalt oxides, Al doped ZnO and a functionally graded ZnO material with a layered structure.

In the third chapter of this dissertation, I discuss our recent studies related to the above-mentioned families of thermoelectric materials for achieving a higher figure of merit, *ZT*, with a focus on characterization results of the Seebeck coefficient, electrical conductivity, and thermal conductivity and briefly explained the mechanism(s) that influence each property.

1.4 Thermal contact resistance in thermoelectric devices

When building a real thermoelectric device, having a material with a large figure of merit, *ZT*, is only one part of creating a reliable, efficient thermoelectric module. The maximum theoretical efficiency of a thermoelectric generator is limited by Carnot efficiency and the average *ZT* of the materials as shown earlier. At the present, dramatic enhancements in *ZT* have been achieved by optimization of the power factor ($S^2\sigma$) and reduction in thermal conductivity in PbTe,[26] skutterudites,[21] half-Heusler alloys,[27] and oxides.[28] However, even building a PbTe-based thermoelectric module using the best available thermoelectric material where the maximum *ZT* reaches around 1.8 for p-type PbTe and around 1.4 for n-type PbTe[5] the overall efficiency is still poor. For example, when the hot side temperature is maintained at 873 K, and the cold side temperature kept at 303 K, the maximum output efficiency only reaches 8.8%. A simple calculation using the above parameters will result in the maximum Carnot efficiency of around 18.8%. Even considering the thermal loss to the environment in simulations, the thermal efficiency still can only reach 12.2% at a 570 K temperature difference, which is already an enormous temperature difference that may only be achievable in quasi-ideal lab conditions[5]. The large difference in the maximum and actual efficiencies

demonstrates that not only are the thermal losses to the outside atmosphere by conduction, convection and radiation important, but the internal thermal contact resistances also reduce the real efficiency of the devices as well.

Internal thermal resistances within thermoelectric modules can be reduced by choosing appropriate materials. Figure 1-6 shows a diagram for a typical thermoelectric generator (TEG) module. Pairs of PN legs of thermoelectric material are well-aligned and a metallic conductive layer functions as an electrode to connect the legs, then upper and lower electrical insulation layers are constructed against a heat exchanger at the hot end and the heat sink at the cold end. The PN legs are connected electrically in series and thermally in parallel. To minimize the thermal resistance from the heat exchanger to the TEG module, a thin layer of an electrically insulating material with excellent mechanical strength and high thermal conductivity is preferred. In most applications, AlN is used as the electrical insulation layer and copper is often used as the electrode in TEG modules to connect the N and P legs.

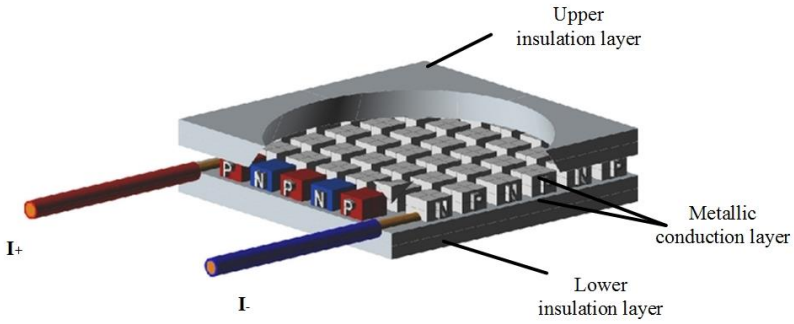

Figure 1-6 A typical overview of a thermoelectric generator (TEG) module.

The upper and lower electrical insulation layers (often AlN) prevent an electrical short between the module and the heat exchanger while the large thermal conductivity ensures that heat can move through the layer efficiently.

The thermal interfaces of thermoelectric devices are similar to issues in heat removal from power electronic devices. However, one critical difference that makes the interfaces much more challenging for thermoelectric power generation is that the TE materials are subject to much greater temperatures and much larger temperature variations. Thus, the interface materials must survive at elevated temperatures and they must also have thermal expansion coefficients that are reasonable matches with the electrical insulation layer and the heat exchanger.

Using a thermal resistance analogy, for heat to flow from the heat source to the heat exchanger, the total thermal resistance may be expressed as the following

$$R_{total} = R_{ins,u} + R_{int,u} + R_{mod} + R_{int,l} + R_{ins,l} . \quad (1\text{-}4)$$

Here the total thermal resistance comes from the combination of the thermal resistance from upper electrical insulation layer, $R_{ins,u}$, the contact resistance from at the upper interface between the insulation layer and module $R_{int,u,}$ the resistance from thermoelectric module itself, R_{mod}, and the similar thermal resistances $R_{int,l}$ and $R_{ins,l}$ at the lower insulation layer side. For determination of thermal resistance of the two insulation layers and the module itself, various methods can be applied by measuring the total thermal conductivity and surface area at different temperatures. However, these two thermal contact resistances are difficult to

determine since they are related to the contact pressure at the two interfaces, the surface roughness, waviness and flatness, surface deformations, and cleanliness[29].

Consequently, robust and reliable thermal contacts between the TEG and heat exchanger (hot side) as well as between the TEG and the heat sink (cold side) are desired in various TEG designs as non-permanent interfaces. Due to the natural surface roughness on real surfaces, there is inevitably some small air gap between the heat exchanger/source and the TEG module, as shown in Figure 1-7 (a). A thermal interface material (TIM) is applied onto the contacts of two dissimilar material to function as an interface layer to decrease the thermal resistance as it could fill the air gap thus increase the thermal conductance effectively. If the thermal interface material is applied between the interfaces of the heat source/exchanger, the interface material not only provides better thermal conductivity than air, but it can also function as a surface protection layer to environmental oxidation, as shown in Figure 1-7 (b).

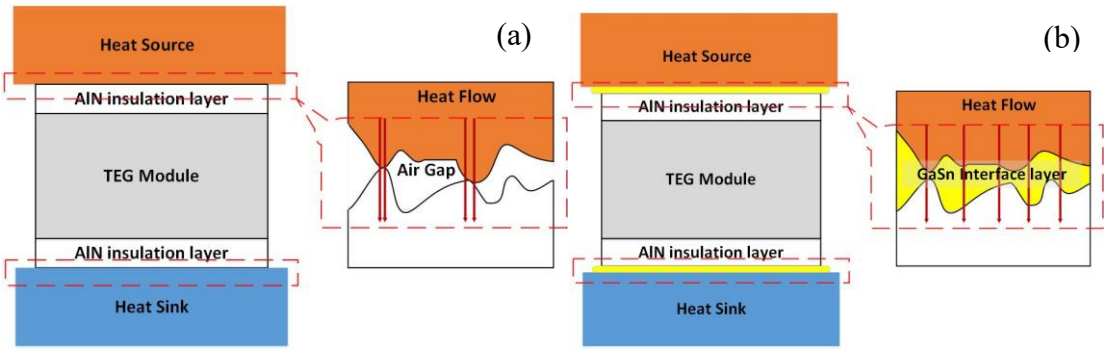

Figure 1-7 Schematic overview of the function of a thermal interface material (TIM). In this case a liquid GaSn layer is used as the TIM for a TEG module. The air gap between the heat source and TEG module can be filled by the thermal interface layer thus providing a continuous thermal path for heat flow while protecting the surface from possible oxidation.

With the implementation of a thermal interface material at solid interfaces, the thermal resistance model at the interface will change into another form, which can be better described using the term of effective total thermal resistance. The introduction of one more layer of thermal interface material is adding one thermally conductive layer to replace the air gap in principle. The effective total thermal resistance at one interface between two dissimilar materials can be concluded as the sum of the resistance due to the thermal conductivity of interface material and the contact resistance between interface material and the two contacting surfaces, so the thermal resistance of this combination can be simplified from Equation (1-4) to:

$$R_{effective} = \frac{BLT}{k_{TIM} A} + R_{c_1} + R_{c_2} \tag{1-5}$$

In this equation (1-5), *BLT* stands for the bond line thickness shown in Figure 1-8, which is the average thickness of the gap between two materials. The terms k_{TIM} and A are thermal conductivity and the surface area of the thermal interface material, respectively. Rc_1 and Rc_2 are the contact resistances of the thermal interface material at the boundary with these two surfaces. The minimization of $R_{effective}$ is an important task for the development of improved thermal performance of thermoelectric devices.

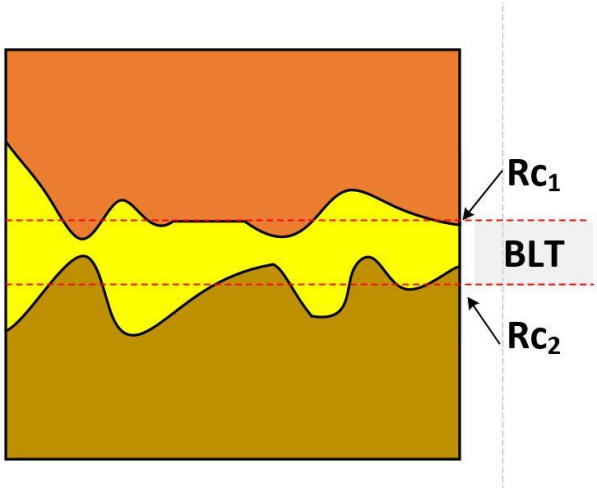

Figure 1-8 The thermal interface material inserted into the gap between two contacting bodies, which has an effective thickness called bond line thickness (BLT).

Though the thermal resistance of one layer of air gap is replaced by the sum of three thermal resistances, one from the filler (TIM) itself and other two being the contact resistances, the application of thermal interface material still has the effect of decreasing the overall thermal resistance. Thus the selection of an appropriate thermal interface material is of critical importance. Several commonly used thermal interface materials in cooling areas are listed in Table 1-1 below[30]–[32]:

Table 1-1 Comparison of several common thermal interface materials

Thermal Interface Material		Advantages	Disadvantages
Thermal Grease		• Good thermal conductivity • Low attach pressure • No curing needed	• Pumping out issue in cycling • Dry-out issue over time • Manually controlled thickness
Phase change material	Polymeric	• Lower thermal resistance • Less dry-out issue • No cure needed	• Constant pressure required • Voids can be detrimental
	Low-melting alloys	• Easy to apply • Metallic contacts • No cure needed	• May have intermetallic interfaces • Oxidation issue
Filled Polymers		• Easy to handle • Conforms well with irregular surfaces • Good dielectrics	• Curing required • Low thermal conductivity • Cannot flow freely

For applications of thermoelectric devices, without the need to insulate the packaging devices, low melting point metallic alloys are an attractive option as a thermal interface material. These liquid metal alloys provide an all-metallic path for heat transfer through the interface, easy pre-curing treatments, excellent compliance with thermal stress, as well as better performance at high temperature ranges. All of these advantages distinguish low melting alloys from other types of thermal interface material.

The excellent cooling capability of liquid metals for thermal management has been widely used in battery modules,[33] microelectronic devices,[34] and computer chip[35], [36] applications, albeit at lower temperatures than required for TEG modules. Dai *et al.*[30] studied a liquid metal based thermoelectric generator for waste heat recovery at a heat source around 200 °C and cooling plate around 100 °C with a Bi_2Te_3 device. However, liquid metal applications in TEG modules are limited compared to the perspective in power electronics area due to the higher temperatures required. There are a very limited number of studies about liquid metal interface layer applications at mid or high temperature TEG modules. Both the uncertainty of low melting point alloys performance with respect to reliability in high temperature environments and the lack of description of the deformation in the solid materials from thermal expansion forces have limited the use of liquid metals for applications as thermal interface materials for thermoelectric generators.

There are a variety of options for selecting a specific liquid metal for use as a high temperature thermal interface material. Traditional liquid metals in the past contained mercury,

which is highly toxic and harmful to the environment. In contrast, gallium-based alloys, which are lower in both vapor pressure at room temperature and toxicity, are being used more frequently today in various applications. Gallium-based liquid metal alloys are a family of eutectic alloys mainly consisting of gallium, indium and tin, typically melting at around 16 °C and having a boiling point that is above 1300 °C [37].

These physical properties give gallium-based liquid metal alloys a wide application range towards almost all existing TEG modules. From the low temperature cooling systems composed of Bi-Te thermoelectric modules, to high temperature Mg_2Si power generators, liquid metals can potentially function as interface filler materials for thermal contacts. However, the wettability (i.e. contact angle) of gallium-based liquid metals varies with different surfaces, which makes the real applications difficult. Another common challenge is the difference in the coefficient of thermal expansion that occurs at interfaces. At high temperatures, any mismatch in the coefficient of thermal expansion between the heat exchanger and the electrical insulating layer will create stress that can either warp one (or both) of the materials causing the materials to come out of contact, thus greatly reducing the heat transfer between the materials. Unlike other TIM candidates such as thermal paste, liquid metal alloys cannot attach to the surfaces directly. However, the liquid metals can flow and potentially fill gaps of reasonable dimensions that could form due to thermal expansion at the interface. Since the targeted module is designed to work at high temperature ranges, the thermal expansion differences must be carefully addressed regardless of what type of TIM is to be used. Figure 1-9 shows a schematic diagram of warpage from an AlN insulation layer when large thermal expansion mismatch occurs at

high temperature. Depending on the temperature difference between the heat source and thermoelectric package module, temperature gradients will develop within the heat exchanger and the insulation layer. The insulation layer could become very convex and the magnitude which would decrease the area of contact with the heat exchanger. The warpage depends on various factors such as the geometry of the surface, the temperature distribution along the interfaces and the magnitude of mismatch in coefficients of thermal expansion.

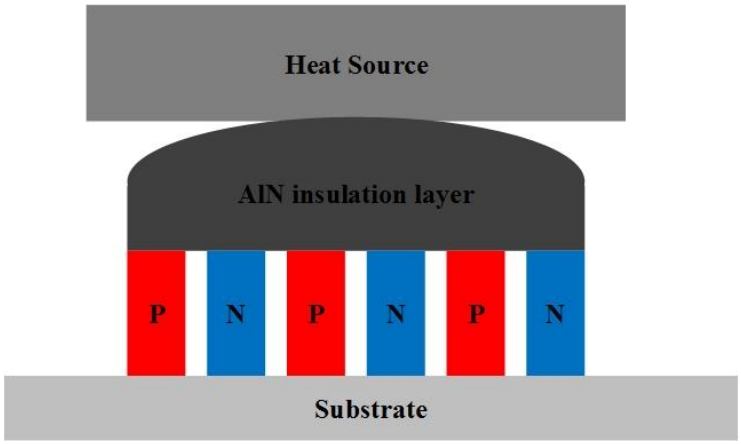

Figure 1-9 Schematic diagram showing a warped insulation layer (not to scale) due to thermal expansion. This schematic also shows that if there is not a compliant thermal interface material between the heat source and the electrical insulation layer, then the thermal linkage between the insulation layer and the heat source will be greatly reduced.

A compliant liquid metal interface with sufficient mobility is necessary in TEG module design. In the fourth chapter of this dissertation, the application of GaSn, a typical kind of galinstan (i.e. a eutectic alloy containing gallium, indium, and tin), as a thermal interface

material for TEGs is discussed. Specifically, both the mechanical and thermal behavior under static pressure are examined, discussed and verified with regard to its role to reduce thermal resistance in TEG design.

1.5 Dissertation Outline

This dissertation discusses my research related to the thermoelectric materials, thermoelectric property measurements, and the use of liquid metal alloys as high temperature thermal interface materials. In Chapter 2, the system design, fabrication and assembly for the measurement of Seebeck coefficient and electrical conductivity is discussed. Additional work regarding measurements of thermal conductivity on various target materials using the laser flash method is also included. In Chapter 3, I will focus the discussion on the development of novel thermoelectric materials with an emphasis on the characterization of the material properties. A variety of thermoelectric materials are needed to build a complete cascade or segmented thermoelectric module. Thus a variety of materials are examined, including low temperature Bi_2Te_3, middle range temperature skutterudites, and high temperature half-Heusler alloys. In addition, several oxidation resistant thermoelectric materials such as ZnO, calcium cobalt oxide, and perovskites are also studied. In Chapter 4, the research about the evaluation of thermal performances of GaSn liquid metal as thermal interface layer is presented. The mechanical and thermal performance of the GaSn layer is examined in a sandwich structure and the results are analyzed quantitatively. Finally, a summary of this work and future work expectations are briefly illustrated in Chapter 5.

Chapter 2 Design of experimental system for thermoelectric characterization

2.1 Introduction

With a continuing increase in the demand for efficient energy sources, numerous possibilities have emerged for a variety of applications. Given the large variety of systems that produce substantial amounts of waste heat, thermoelectric materials, which can directly convert heat into electricity without moving parts, have received significant attention. Measuring the Seebeck coefficient and electrical resistivity for bulk thermoelectric samples is an essential part for examining promising thermoelectric materials. Thermoelectric materials can be characterized by the dimensionless figure of merit, *ZT*, which gives a measure of the energy conversion efficiency for the material and is expressed as[7]

$$ZT = \frac{S^2\sigma}{k}, \tag{2-1}$$

where *S* represents the Seebeck coefficient, σ is the electrical conductivity, *k* is the thermal conductivity, and *T* is the absolute temperature. Thus, in order evaluate thermoelectric materials, one must measure these material properties over the temperature range in which the material will be used. Accurate measurements of each property are challenging, and in this work we focus on measurements of the Seebeck coefficient and the electrical conductivity for temperatures between 300 K and 600 K.

A variety of techniques have been developed for measurements of the Seebeck coefficient, each with their own advantages and disadvantages.[38]–[42] While there is an assortment of methods for measuring the Seebeck coefficient, the general idea is to measure the voltage generated by the sample while the sample is under a temperature gradient. Thus, despite some differences in measurement protocols regarding the accuracy and repeatability, some key guidelines are commonly followed during Seebeck coefficient measurements[38]:

1) Voltage and temperature must be measured at the same locations and at same time;

2) Excellent thermal (isothermal) and electrical (ohmic) contacts must be maintained between the probes and the sample;

3) The measurement system must be stable, and noise from the measurement and data-acquisition systems must be minimized as voltages generated in samples are typically in the range of a few μV.

With the above considerations in mind, one can examine the thermoelectric properties of material *a* using leads from a reference material *b* that are in isothermal and ohmic contact with *a*. When a thermal gradient is applied to the sample such that one end is hot at a temperature of T_h and the other end is cold at a temperature T_c, an electric potential, $V_{ab}(T_c, T_h)$ will develop between the junctions of the two materials[38]

$$V_{ab}\left(T_c,T_h\right) = \int_{T_c}^{T_h} S_{ab}\left(T\right)dT = \int_{T_c}^{T_h}\left[S_b\left(T\right) - S_a\left(T\right)\right]dT \qquad (2\text{-}2)$$

,

where $S_a(T)$ is the absolute Seebeck coefficient of sample *a*, and $S_b(T)$ is the absolute Seebeck coefficient of the known reference material, *b*. With the assumption that materials *a* and *b* are homogeneous and isotropic so that V_{ab} is only a function of T_a and T_b, (2-2) can be reduced to the following[43]

$$S_{ab} = S_b - S_a. \tag{2-3}$$

In other words, the Seebeck coefficient from the sample, S_a, can simply be determined from the measured relative Seebeck coefficient, S_{ab}, provided that the Seebeck coefficient of the material used for the lead wire, S_b, is known. From this basic starting point, there are several methods by which the Seebeck coefficient can be measured.

Martin[43] summarized the two main approaches for measurements of the Seebeck coefficient: the integral method and the differential method. In the integral method, an increasing temperature gradient is created between the two ends of the sample, which leads to an open circuit voltage, known as the thermopower voltage. One end of the sample is kept at a fixed temperature, T_c, while the temperature is increased at the other end as $T_h=T_c+\Delta T$[44], [45]. The real-time voltages and temperatures, $V_{ab}(T_c, T_h)$, are then recorded over a large ΔT, and a best-fit curve or analytic expression is then applied to the data. The analytic expression is then differentiated with respect to T_h, such that (2-2) becomes

$$S_{ab}(T_h) = S_b(T_h) - S_a(T_c) = \frac{dV_{ab}(T_{c,}T_h)}{dT_h} \tag{2-4}$$

Thus, the absolute Seebeck coefficient of the sample can be readily obtained from the slope of the curve at any temperature T_h. Since large temperature gradients are used, large voltages are generated making the integral technique relatively insensitive to small voltage offsets. However, in addition to the occasionally used complicated methods for data fitting, in practice it is often difficult to maintain a constant temperature at the cold end, in particular for short samples at high temperature, thus limiting the accuracy and feasibility of this technique.

In contrast to the large temperature gradient used in the integral method, the differential method applies a comparatively small thermal gradient ($\Delta T < 0.1T$) across the sample. Here, with a small ΔT, the average temperature, T_0, is defined as[38]

$$T_0 = \frac{T_h + T_c}{2} = T_h - \frac{\Delta T}{2} = T_c + \frac{\Delta T}{2} . \tag{2-5}$$

When ΔT is sufficiently small ($\Delta T/T_0 << 1$), and $\Delta S/S << 1$,

(2-2) can be simplified and rewritten[38] as

$$S_{ab}(T_0) = S_{ab}(\frac{T_h + T_c}{2}) = \frac{V_{ab}}{T_h - T_c} . \tag{2-6}$$

In practice, in order to improve accuracy, it is required to observe the linearity of $S_{ab}(T_0)$ by examining different ΔT values at each temperature point of interest.

For measurements of electrical resistivity, the four point probe method is widely used for thermoelectric materials, not only for evaluating new high ZT materials[46], but also for developing a Seebeck coefficient standard reference material[13]. Since the four-point probe method requires an axial current flow and precise dimensional measurements in order to apply

a proper geometric correction factors[47], bar shaped samples are the preferred geometrical shape for samples with this technique as evidenced by the fact that common commercial measurement systems require bar shaped samples. However, for determination of another critical factor in ZT, thermal conductivity k, measurements are often performed with the laser flash method, which generally requires a disk shaped sample. This difference in sample shape requirements for thermal and electrical characterization leads to difficulties in that samples either need to be cut or multiple samples must be prepared for the different measurements, thus introducing uncertainty due to variations from sample to sample. Additionally, the bar shaped samples are typically cut in the same direction as the disk shaped samples. However, the Seebeck measurement is applied along the bar direction and thermal measurement is applied across the thickness of the disk, which leads to the orientation difference in measurement. The measurements in perpendicular directions lead to another source of uncertainty for anisotropic materials.

Another solution for electrical resistivity measurements was firstly proposed by van der Pauw[48] in 1958. The major advantage of the van der Pauw method is that it can measure electrical resistivity on samples of arbitrary shape along any directions, thus saving a great amount of preparation work and covers the anisotropic issue. Unlike the four point probe method, which requires accurate measurements for all dimensions of samples in order to calculate the geometric correction factor, the van der Pauw method only requires one dimension (thickness) to be measured beforehand. In our experimental setup, in order to accommodate

different shapes and dimensions for samples and to improve accuracy, the van der Pauw method is selected for resistivity measurements.

In this work, we detail the design and validation of a home-built experimental system to measure the Seebeck coefficient and electrical resistivity for bulk thermoelectric materials. The description of the setup is presented first, then a standard sample (SRM 3451) and round robin tests of ZnO samples are used to validate the accuracy of Seebeck coefficient measurements. Next, the same SRM 3451 sample along with a nickel-based sample are used to assess the electrical resistivity measurements. Finally, we present a brief analysis of possible sources of error for the instrument.

2.2 Experimental System and Measurement Description

The overall experimental system is housed inside a vacuum sealed bell jar, and the system is divided into three parts: 1) Baseplate with supporting rods; 2) Measurement module with cartridge heaters and probes; 3) Data acquisition and control system. Most parts are custom designed and manufactured through the local department machine shop. Figure 2-1 shows the 3D design overview in SolidWorks, including the setup base, clamping plate and supporting rod.

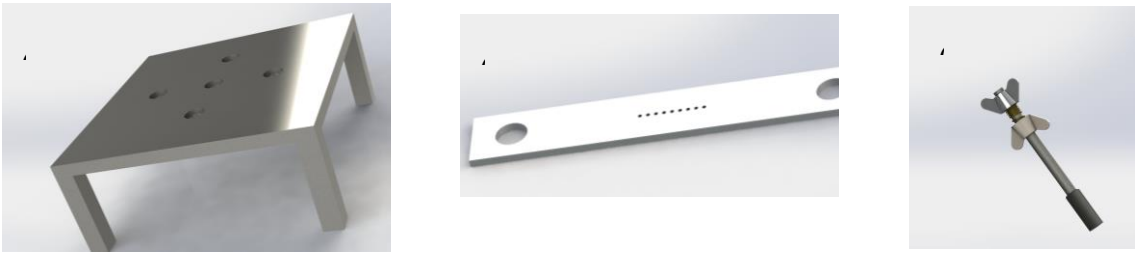

Figure 2-1 Customized parts for the measurement system. (a) setup for the supporting base; (b) clamping plates for the thermocouples and (c) for the supportive rods to hold the heaters.

The overview of the system design is presented in Figure 2-4. The overall system is basically composed of a bell jar that contains all measurement units inside, measurement units including supportive rods, thermocouples, heaters and holder plate, supportive base and the connection ports beneath it. For clarity, Figure 2-2 does not include all of the connections to the vacuum stage or the wires that transfer signals, which are important but complicate the overview of the system.

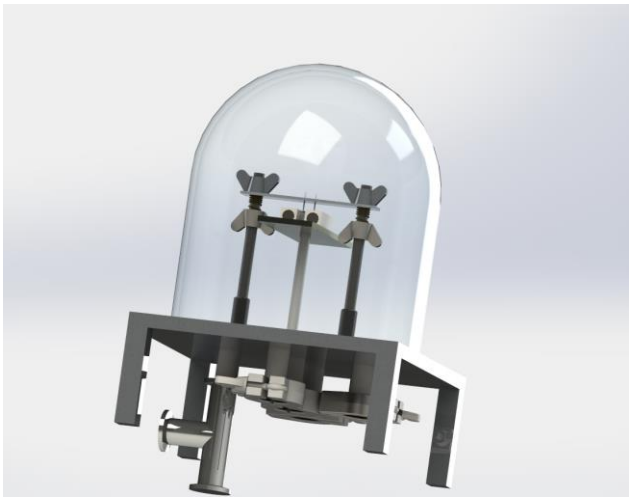

Figure 2-2 Three-dimensional overview of the overall measurement system.

By removing the bell jar, a more detailed understanding of the structure can be obtained through an explosion view (Figure 2-3) of the 3D view. The assembly relation is more clearly

illustrated in Figure 2-3. A zirconia rod attached to the base plate supports the heater plate, the cartridge heater, clamping plate, and the thermocouples. On both sides of the clamping plate, two threaded rods are used to hold the thermocouples at a perpendicular position relative to the sample. There are a total of five feed-throughs on the backside of the base, one for the wire connection terminal, one for the vacuum pump, and the other three can be inlets for multiple inert gases.

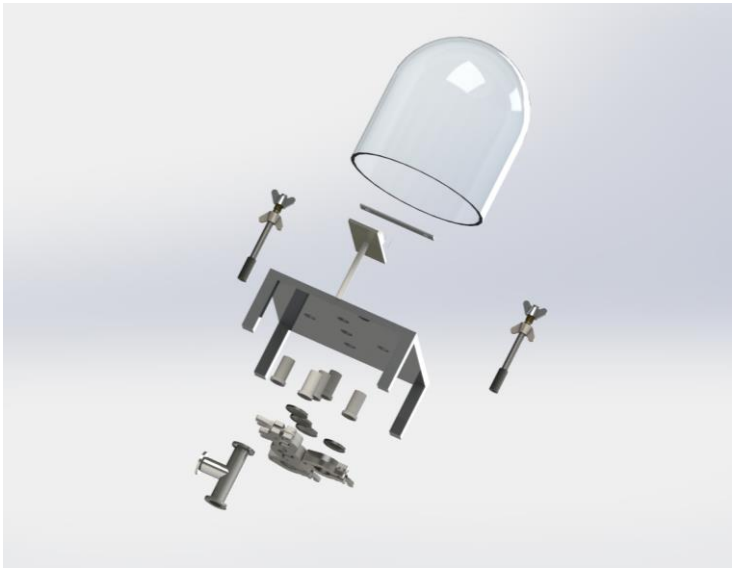

Figure 2-3 The explosion view of the measurement system.

The detailed core part of the measurement setup is shown in Figure 2-4. The square baseplate (not shown in Figure 2-4) is made from stainless steel with dimensions of 460 mm × 460 mm × 20 mm and is supported by four stainless steel rods of 25 mm × 25 mm × 225 mm. The supporting rods lift the baseplate, and the entire system, off a lab bench to allow for numerous electrical and vacuum feedthroughs to the system. An optical breadboard is attached to the top of the baseplate, and this breadboard is used as a fixing plate (*k* in Figure 2-4) for the

supporting rods used in the measurements. To accommodate a variety of samples, all of the supporting rods (*g* in Figure 2-4) attached to the fixing plate are adjustable by about 40 mm.

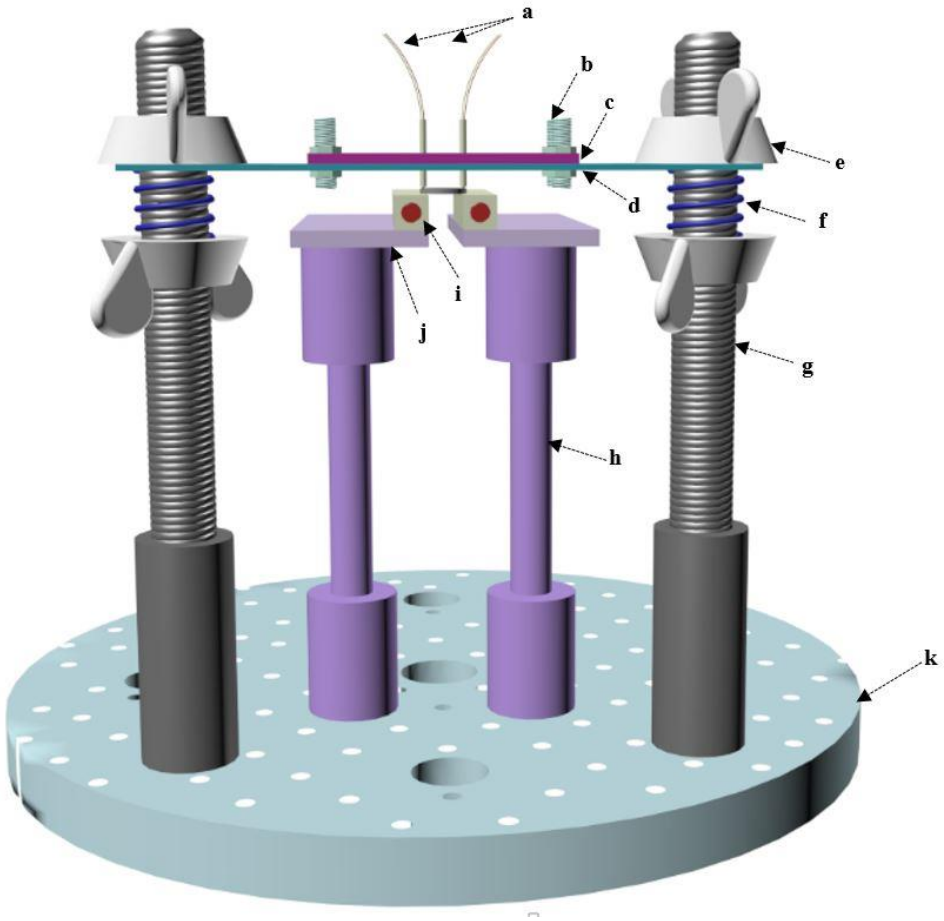

Figure 2-4: Schematic diagram of the home-built instrument setup. Supporting rods (g and h) provide thermal isolation from the fixing plate (k). Cartridge heaters (i) input heat to the attached sample, and temperatures and voltages are measured with probes (a) applied to the surface of the sample.

Two individually controlled cartridge heaters (i) are used to heat the two ends of a sample that is attached to the heaters with thermal paste. The cartridge heaters are fixed to the smooth surfaces of stainless steel platforms (*j*), which, in turn, are supported by two ceramic (zirconia)

rods (*h*). The low thermal conductivity zirconia rods limit the heat loss from the heaters to the surrounding environment, thus increasing the thermal stability of the system.

As mentioned previously[38], voltage and temperature must be measured at the same locations and at same time through excellent contacts on the sample. To fulfill these requirements, a pressed probe (*a*) arrangement with adjustable spring (*f*) forces is employed.

.

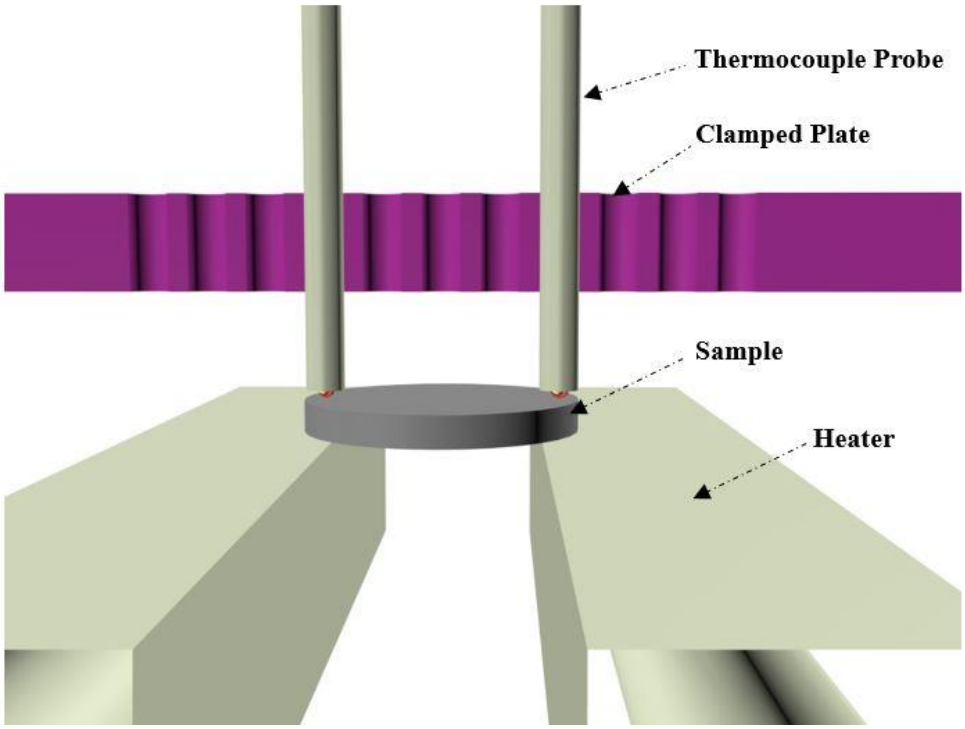

Figure 2-5: Close up view of the thermocouple probes on the sample. The thermocouple probes are housed in mullite tubes that are clamped tightly to a plate. The plate is then adjusted vertically in order to press the thermocouples onto the sample surface.

Figure 2-5 displays a close up view of the thermocouple probes on the sample. The thermocouple wires are fed through mullite tubes to form the probes. The probes are pressed

firmly onto the sample surface through the combination of two wing nuts (*e* in Figure 2-4) and two springs (*f* in Figure 2-4) to move a plate (*d* in Figure 2-4) that is clamped to the mullite tubes. The springs and wing nuts provide a vertical pressing force, and they ensure good contact, even for samples with non-uniform thickness. Secondly, with the help of the fitting through holes in the upper plate (*c*) and the tiny fastening threaded rods (*b*) located on corners, the whole structure is able to provide a straight linear support to confirm that the probes can be pressed perpendicularly. By using a vertical force from the springs to locate samples, it would greatly overcome the geometrical limitations of tested samples, which gives more freedom to choose variable candidates. The probes were used to measure voltage and temperature at the same spot. With the use of an Agilent 34970A switch unit, the time between voltage and temperature measurements was limited to 1.5 seconds, thus ensuring that measurements were nearly simultaneous and at the same location.

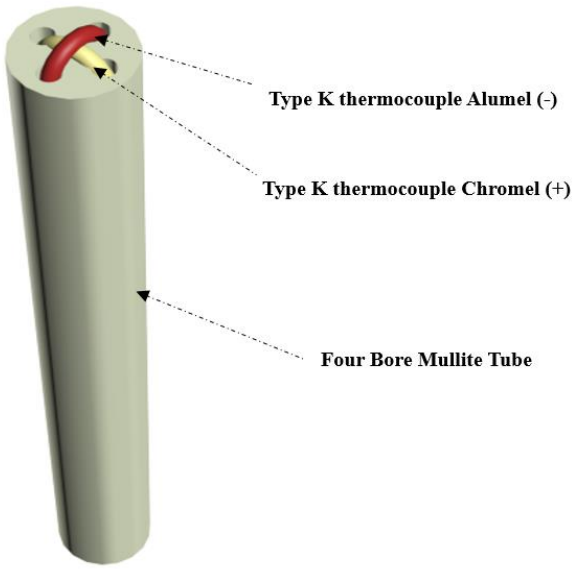

Figure 2-6: Details of the thermocouple probe design. The two thermocouples wires are fed through a mullite tube, and the wires cross at the end of the tube to form the thermocouple junction and probe tip.

The probes used in this system are a modification from Wood's[44] previous work. Similar to the previous work, we use a four-bore mullite tube in order to form a thermocouple junction at the tip of the probe. As shown in Figure 2-6, the two thermocouple wires with a diameter of 255 μm cross at the end of the tube in order to form a junction. To reduce heat losses through the probes from the sample, we choose a ceramic, mullite, with low thermal conductivity for the tube. A Type K thermocouple is selected due to its ability to cover a wide temperature range (-200 °C to 1350 °C,) which exceeds the temperatures as which the thermoelectric materials will be tested (room temperature to ~325 °C).

As mentioned previously, the van der Pauw method is used to measure electrical resistivity. With this method, the electrical resistivity of the sample is given by[49]

$$\exp\{\frac{-\pi R_{AB,CD}h}{\rho}\}+\exp\{\frac{-\pi R_{BC,DA}h}{\rho}\}=1 \quad (2\text{-}7)$$

where ρ is the resistivity of a sample of arbitrary shape,and h is the sample thickness. $R_{AB,CD}$ is the resistance determined from a measurement of the voltage between locations C and D when a current is passed from A to B as shown in Figure 2-8 (i.e. $R_{AB,CD} = V_{CD} / I_{AB}$), and $R_{BC,DA}$ is defined in a similar way.

Equation (2-7) can be solved by an iteration method automatically in a LabVIEW program with inputs of resolution, two surface resistances and sample thickness h. The iteration process leads to the resistivity of sample directly. Figure 2-7 shows the schematic view of the structure of this LabVIEW program.

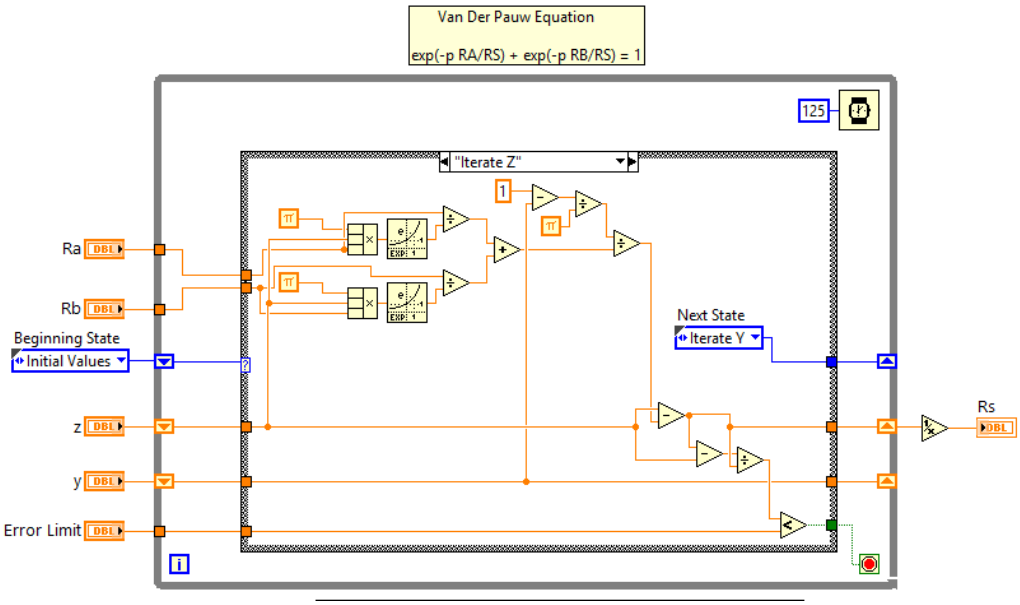

Figure 2-7 Iteration program that automatically translates the input resistance values into the desired resistivity ρ.

Koon[50], [51] examined errors in van der Pauw measurements resulting from the contact placement, tip contact size, and sample resistivity inhomogeneities. To improve the measurement accuracy, three primary requirements must be satisfied:[52]

1) The sample must be continuous with uniform thickness,

2) The four probes must be securely attached to the sample circumference, and

3) The contacts of all of the probes must be sufficiently small. While performing measurements, it is essential to fulfill the second and third requirements.

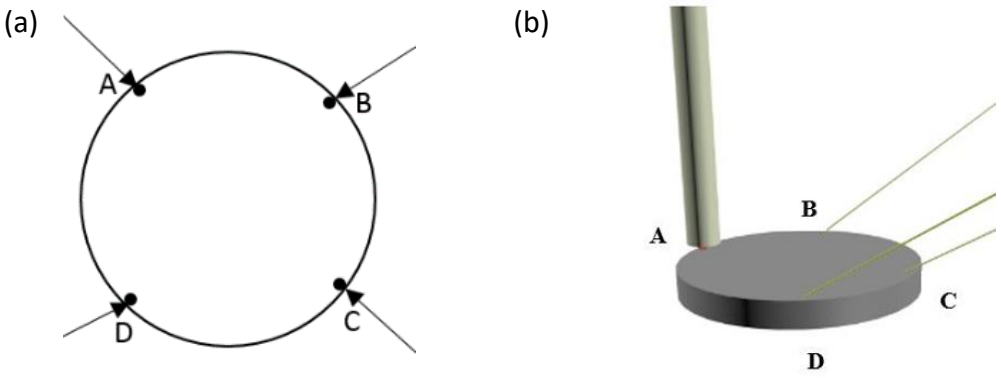

Figure 2-8: Schematic diagrams of the van der Pauw measurement method. (a) The ideal position for four probes in a disk-shaped sample; (b) actual experimental method where one of the probes is replaced by a thermocouple tip.

Figure 2-8 displays the ideal probe arrangement for resistivity measurements. As shown in Figure 2-8(b), in our measurements, one pin-shaped probe is replaced with a thermocouple probe in order to monitor the real-time temperature of sample through the use of the fast Agilent switch. All of the pin-shaped probes are controlled through independent micro-positioners,

which guarantee precise control of probe positions on each sample. To maintain a uniform and stable temperature around the sample, the sample is placed directly on one cartridge heater. The actual position of the probes is shown in Figure 2-9, where three probes are pin-like needle probes located on the edge of the sample while the last one is kept perpendicular by a clamping plate as thermocouple probe. By replacing one standard probe with a thermocouple, one can then monitor the actual temperature on the sample surface while not introducing an additional heat load to the sample.

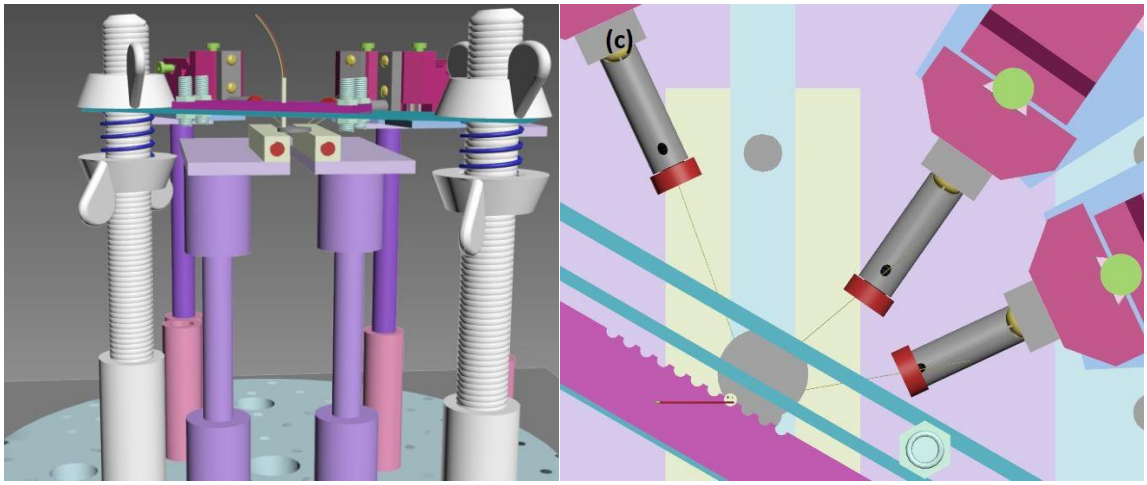

Figure 2-9 Actual setup for resistivity measurements. The left image shows the locations of the probe holder and the image on the right displays the probe placement onto the sample itself. A section view of the clamping plate is made to show the thermocouple position

In order to improve accuracy for the electrical resistivity measurements, a reversed polarity measurement is preferred to remove the impact of voltage offsets.[53] To perform these measurements, the sheet resistance is recorded eight times with current passed in different

directions using the Agilent 34970A switch. As shown in Figure 2-8 and (2-7), $R_{AB,CD}$ and $R_{BC,DA}$ can be redefined as $R_{Horizontal}$ and $R_{Vertical}$, which can be expressed as

$$\begin{aligned} R_{Horizontal} &= \frac{\frac{R_{AD,BC}+R_{DA,CB}}{2}+\frac{R_{BC,AD}+R_{CB,DA}}{2}}{2} \\ R_{Vertical} &= \frac{\frac{R_{AB,DC}+R_{BA,CD}}{2}+\frac{R_{DC,AB}+R_{CD,BA}}{2}}{2} \end{aligned} \tag{2-8}$$

In (2-8), we also can make a small modification from the original method in order to eliminate the effect of spurious voltage offsets with

$$\frac{R_{AD,BC}+R_{DA,CB}}{2}=\left|\frac{U_{AD,BC}-U_{DA,CB}}{2I}\right|. \tag{2-9}$$

By using the same magnitude of current I applied on different ends with the polarity change, we can use eight consecutive measurements to calculate electrical resistivity. In measurement practice, the switch card in the Agilent 34970A can fulfill the action of changing polarity and changing the input end. By connecting to multiple switches in the switch card, the logic function of switching between the current end and voltage reading end can be obtained. The example of dataflow is shown below in Figure 2-10:

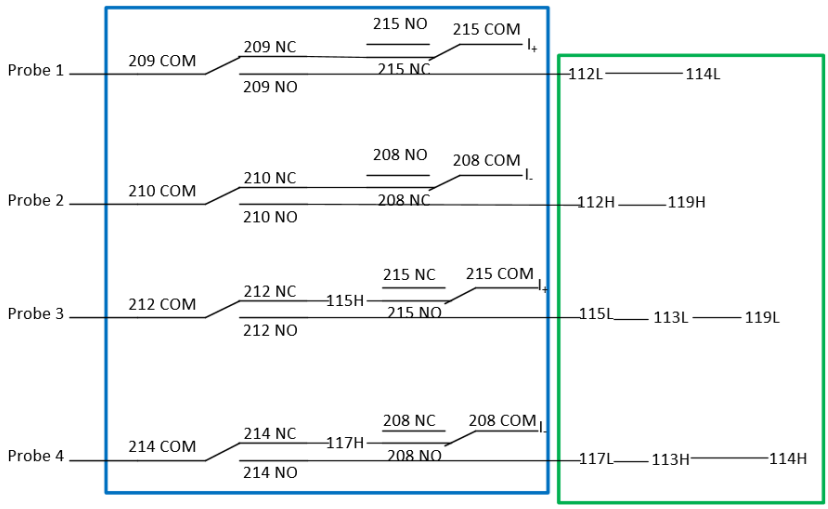

Figure 2-10 The dataflow chart of the probe connections in the switch card. The combinations of these gates enable each probe to function as a current source or voltage reading end.

Several examples can be used to illustrate how this switch function works. If Probe 1 and Probe 2 connect as shown in (2-9), they connect to the current ends acting as current inputs for the sample. At the same time, Probe 3 and Probe 4 need to be switched to the NO side, where they can connect to terminal 113. Then the voltage across the sample can be read through reading the voltage difference from terminal 113. In this way, by referring digits 1-4 to letters A-D, voltage $U_{AB,DC}$ can be known. Then applying a negative current flow using the same connection, $U_{BA,CD}$ is also available. So one part in (2-8) can be recorded according to (2-9), which is $\frac{R_{AB,DC}+R_{BA,CD}}{2}$. Similar processes can be done to record the remaining necessary parts in (2-8), by reading the voltage differences at terminals 112, 114 and 119, respectively.

The whole measurement should employ the following procedures: First of all, the vacuum chamber is pumped down to a pressure of approximately 8×10^{-6} Torr, and the pressure can be

obtained by the ion gauge. Once the chamber is evacuated, the Seebeck coefficient measurements are conducted first systematically:

1) Both of the cartridge heaters are set to their desired temperatures;

2) The system is allowed to stabilize until the temperatures are constant (3-5 minutes);

3) The temperature for one heater is increased gradually in order to create a small temperature gradient across the sample;

4) The voltages and temperatures are alternately recorded using a LabVIEW program for a period of five minutes;

5) Steps 1-4 are then repeated at different targeted temperatures. After completing these steps for the temperature range of interest, the collected data are used in a linear analysis to calculate the Seebeck coefficient.

Similarly, the electrical resistivity measurements use the following procedure:

1) Place the sample on one heater and arrange all of the probes on the sample as shown in Figure 2-8;

2) Evacuate the bell jar to a pressure of approximately 8×10^{-6} Torr;

3) Change the setpoint for the cartridge heater and allow the temperature to stabilize;

4) Run a LabVIEW program to apply current to the appropriate probes and to measure voltage from the other probes. The program will automatically switch polarity of both the

current source and voltage meter, and repeat the measurements. After Steps 3 and 4 are repeated for the temperature range of interest, the data are processed and calculated to determine the electrical resistivity of the sample.

2.3 Results and discussion

To validate the accuracy and precision of our experimental system, a standard Seebeck coefficient material (SRM 3451) from NIST with known properties was first examined from room temperature to 400 K. More information about the production, repeatability and properties of this reference material can be found in several reports from Lowhorn[13], [54], [55]. All the measurement process were finished using the protocol and procedures described above.

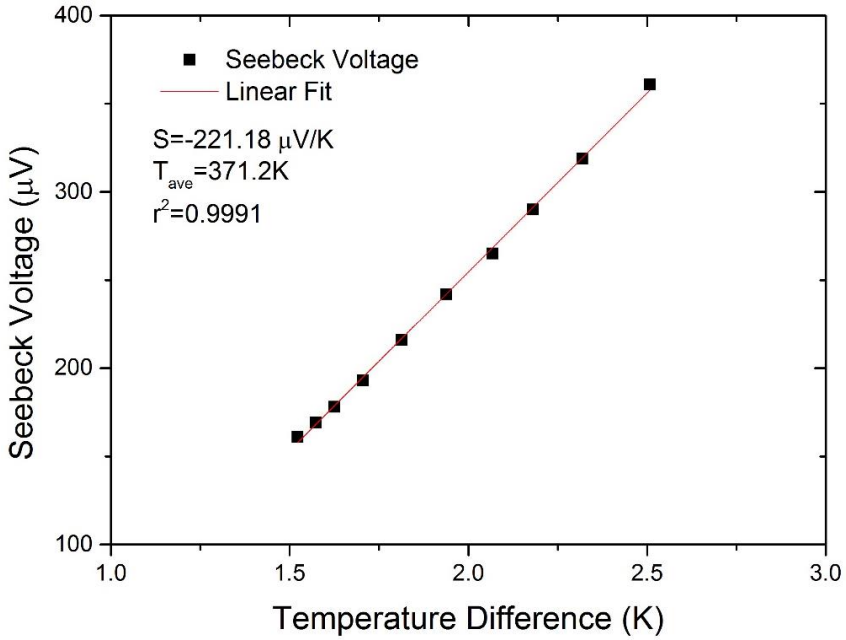

Figure 2-11: Typical Seebeck voltages measure by the experimental system for standard sample SRM 3451 at a temperature of 371.2 K. By measuring the Seebeck voltage over a range of temperature differences, the measurements are insensitive to small offset voltages that may be present in the system.

Figure 2-11 displays a typical data curve for measurements of the Seebeck coefficient at one specific temperature point. Here, the measured Seebeck voltage is plotted for various temperature differences at the same average temperature of 371.2 K, which is the interested temperature point. The linearity of the data indicates that there are Ohmic contacts between the probes and the sample with no Schottky barrier[56], and the slope gives the relative Seebeck coefficient between the sample and the probe end (Alumel in this case). From the definition of (2-3), with the known Seebeck coefficient of Alumel[57], the Seebeck coefficient can be determined at each targeted temperature point.

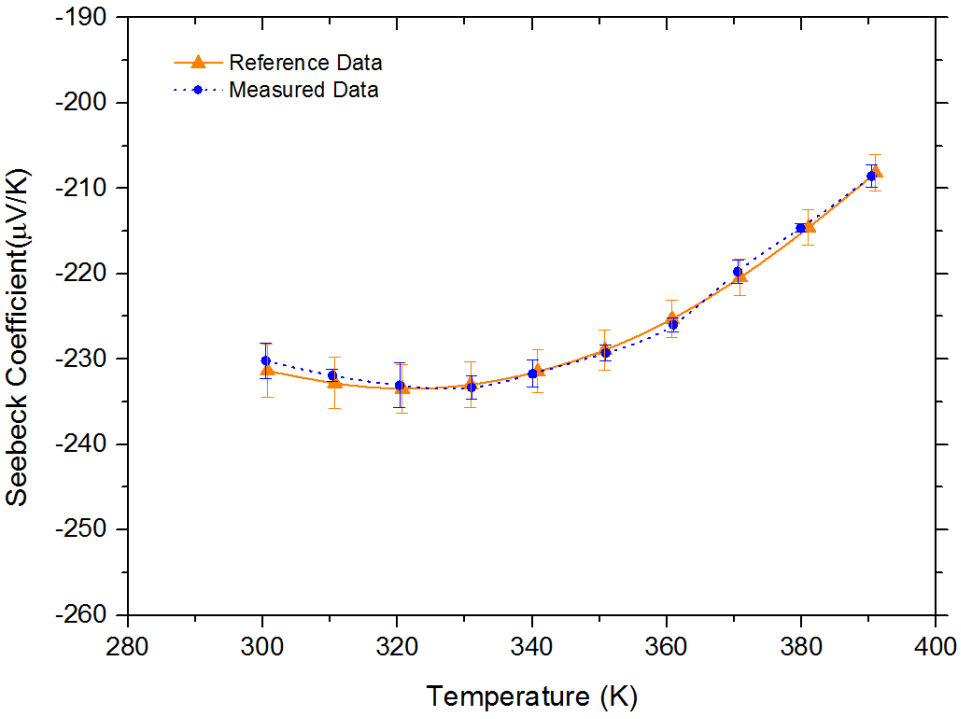

Figure 2-12: Measured Seebeck coefficient of NIST SRM 3451 standard Seebeck sample as a function of temperature. The reference data (orange triangles) is from Lowhorn[13] with uncertainties of ±2.7%. The close agreement between the current measurements and the reference data gives confidence in the design of the new measurement system.

Figure 2-12 displays a comparison between the measurements of the temperature dependent Seebeck coefficient from Lowhorn[11] on the a standard reference sample (NIST SRM 3451) and measurements conducted with our new system . At each targeted temperature, we performed measurements three times to reduce random experimental error, and our uncertainties are estimated to be 2.5%. The excellent agreement between these two measurements provide suitable validation for the new measurement system.

While the SRM 3451 sample was useful for validating the system at temperatures below 400 K, additional measurements on other materials are required for its validity check at higher temperatures. Thus, we examine a second material, ZnO doped with aluminum, through comparative measurements conducted with our system and a commercial system (TFTEP-800, from SeePel Co., Ltd.) at the Korea Institute of Science and Technology.

Table 2-1: Sintering atmosphere and temperature for 2% Al-doped ZnO samples.

	Sintered Atmosphere	Sintered Temperature
Sample #1	Nitrogen	1400 °C
Sample #2	Nitrogen	1300 °C
Sample #3	Nitrogen	1200 °C
Sample #4	Air	1400 °C

All samples examined in this round of measurements are ZnO doped with 2% of aluminum, but each sample was sintered under different conditions as shown in Table 2-1. Figure 2-13 displays the Seebeck coefficients for these samples as measured by the new measurement system as well as the aforementioned commercial system from 300 K to around 600 K. The results agreed well for all four samples with a maximum difference of ~10% over measured temperature range. All of the ZnO samples exhibited negative Seebeck coefficients (α)

indicating *n*-type thermoelectric material. For the samples sintered under nitrogen, the increase of the absolute value of the Seebeck coefficient can be explained to the decrease of carrier concentration for those sintered at higher temperatures[58]. For the two samples sintered at 1400 °C, the ZnO-2%Al sample sintered in air exhibits a significantly larger Seebeck coefficient than the sample sintered under nitrogen, as a result of a decrease in carrier concentration[4].

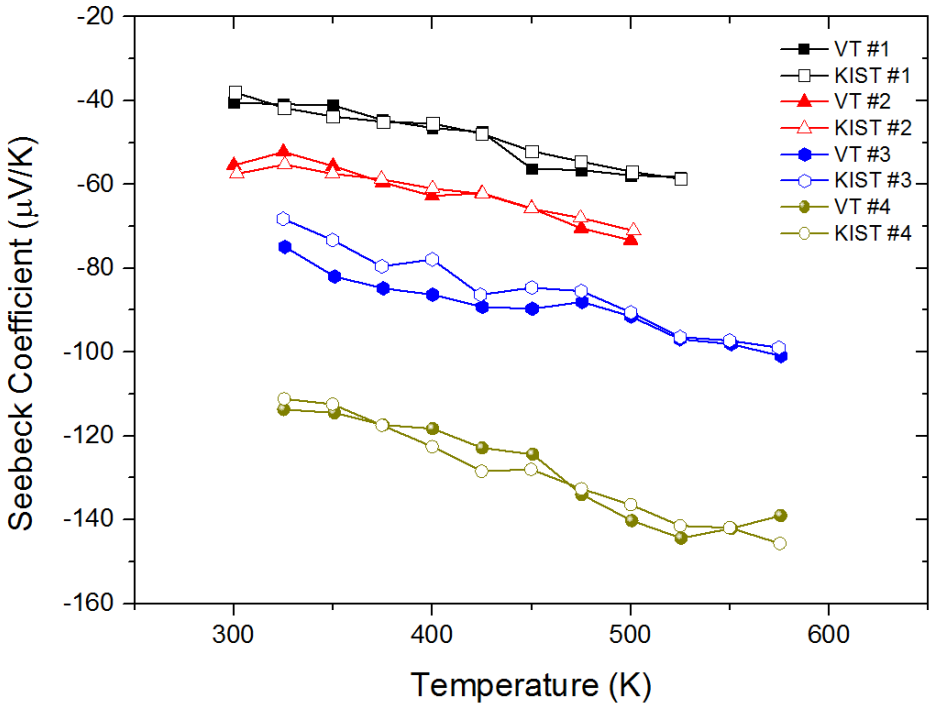

Figure 2-13: Four groups of samples were measured both with the new measurement system developed at Virginia Tech (filled symbols labeled "VT") and also with the commercial measurement system (TFTEP-800, from SeePel Co., Ltd.) at the Korea Institute of Science and Technology (open symbols labeled "KIST"). These results also demonstrate suitable accuracy of the new system.

The standard SRM 3451 reference sample made from Bi_2Te_3 was also used to validate the electrical resistivity measurements. After surface polishing, the dimensions of the rectangular bar-shaped SRM sample were 1.91 mm × 3.53 mm × 7.87 mm, respectively. However, a normal-used van der Pauw method requires that the sample thickness should be much smaller than the lateral dimension. Weiss *et al.*[59] provide an analytical formulation for a correction factor in van der Pauw measurements for samples with finite thickness using pin-point contacts for a rectangular parallelepiped sample. According to this work, this sample has a ratio of thickness to lateral dimension of 0.54, from the ratio of 1.91 divided by 3.53, which leads to a correction factor (CF) of 0.97 where CF is applied to:

$$\rho = \rho_{vdP} CF \,, \tag{2-10}$$

where ρ_{vdP} represents the calculated van der Pauw resistivity in (2-7) using the iteration method, and ρ is the corrected electrical resistivity.

With the correction factor applied, the sample resistivity was obtained as a function of temperature up to 400 K, and the results are shown in Figure 2-14.

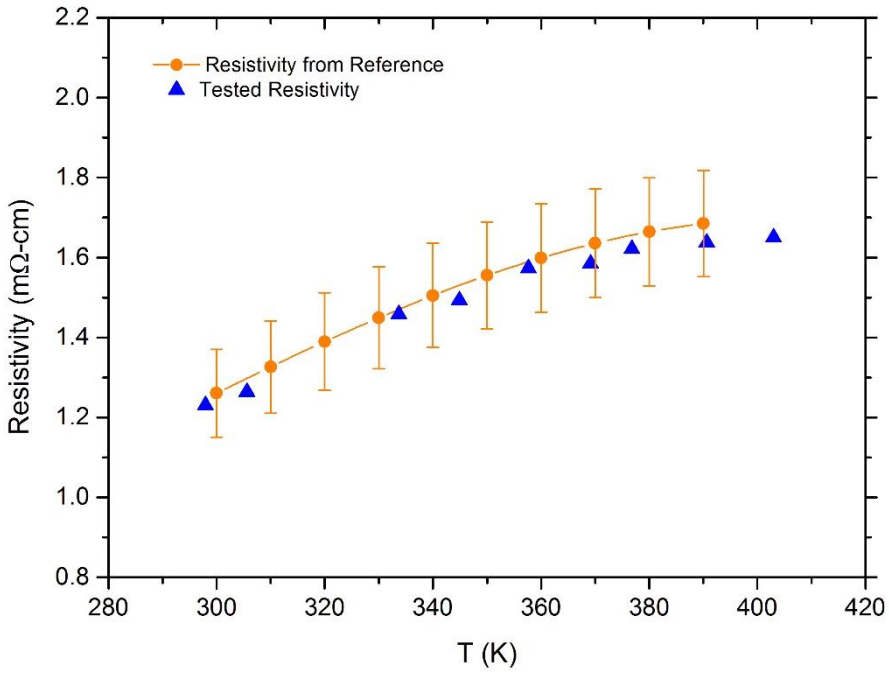

Figure 2-14: Measured electrical resistivity of the Bi_2Te_3 standard SRM 3451 sample from NIST. The reference data, including uncertainties of ± 8.8%, is from Lowhorn.[13]. The results from the van der Pauw measurements are shown to be in good agreement with data taken from measurements performed with a standard four-point probe method.

For validation of the electrical resistivity measurements at higher temperatures, we examine Monel, a nickel-based alloy (70% nickel, 28% copper, and 2% manganese) with typical semiconductor behavior. The measured sample, Monel 400, is from High Temp Metals, Inc. with known electrical resistivity[60]. Kasl and Hoch[61] experimentally studied the effect of thickness for disk shaped samples with the van der Pauw method. Based on this previous work, samples were fabricated with sufficiently small thickness to diameter ratio, with thicknesses ranging from 1.62 mm to 2.12 mm for a uniform diameter of 9.06 mm.

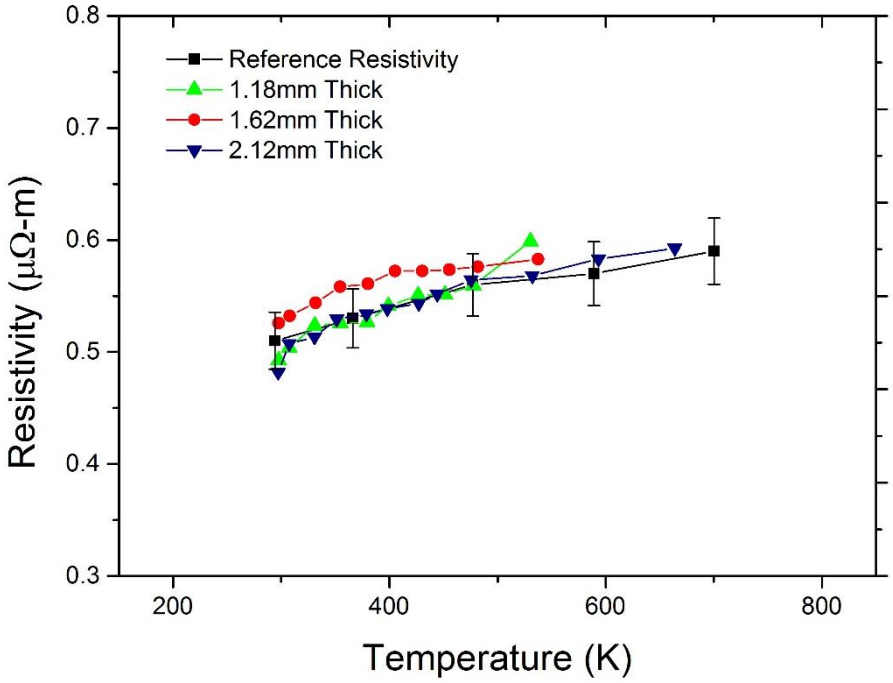

Figure 2-15 Comparison of electrical resistivity measurements of Monel 400 samples of various thickness with the reference data.[60] The current results are in reasonably good agreement (within 6% error) with the reference data.[60]

Figure 2-15 displays measurements of electrical resistivity for disk shaped Monel 400 samples of different thickness from 300 K to approximately 600 K. The results are all in a good agreement (within 6%) with reference data[60] across this temperature range.

2.4 Systematic thermal simulation analysis

According to the setup, there are thermocouples located on two ends of the sample to monitor the temperature profile. However, with only two inputs, it is difficult to determine the overall temperature field inside of the bell jar, especially at the sample surfaces. Considering that increasing the number of thermocouples is the bell jar is not practical due to space considerations, a simulation tool can be a helpful resource to investigate the overall temperature

profile. As there are many parts and components in the system, in the simulation, several simplifications are applied to the actual setup. Therefore, the physical model that was built in COMSOL for analysis, is shown in Figure 2-16.

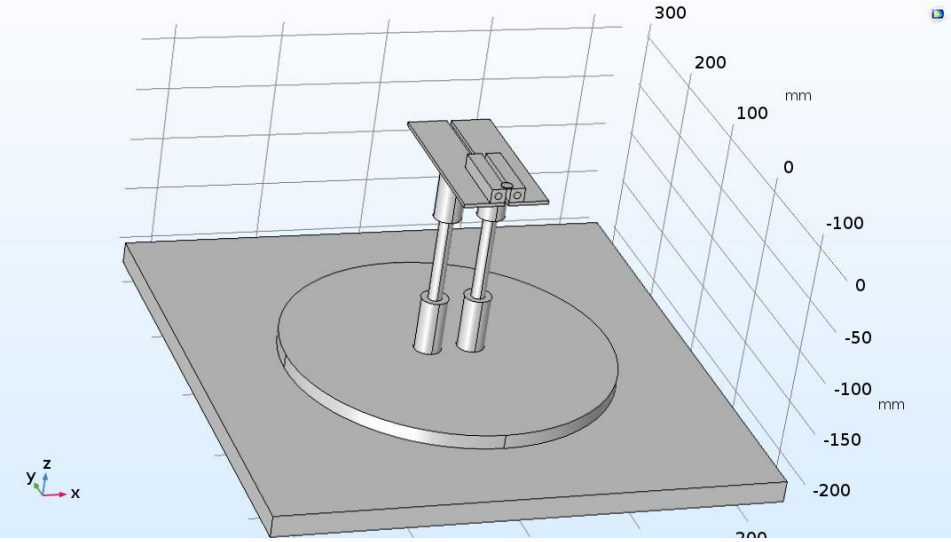

Figure 2-16 A simplified model is constructed in COMSOL for thermal analysis.

Since we are only interested in the temperature profile around the sample, the heat transfer can be limited to the objects around the sample. The boundary condition can be understood as having constant temperature at two cartridge heaters, where the core is made of a high thermal conductivity material Incoloy, ensuring a constant temperature for the whole body. Moreover, the heat loss in the system will be mainly through convection losses between the parts and atmosphere inside. Based on these boundary conditions and simplifications, a temperature profile inside the chamber can be examined.

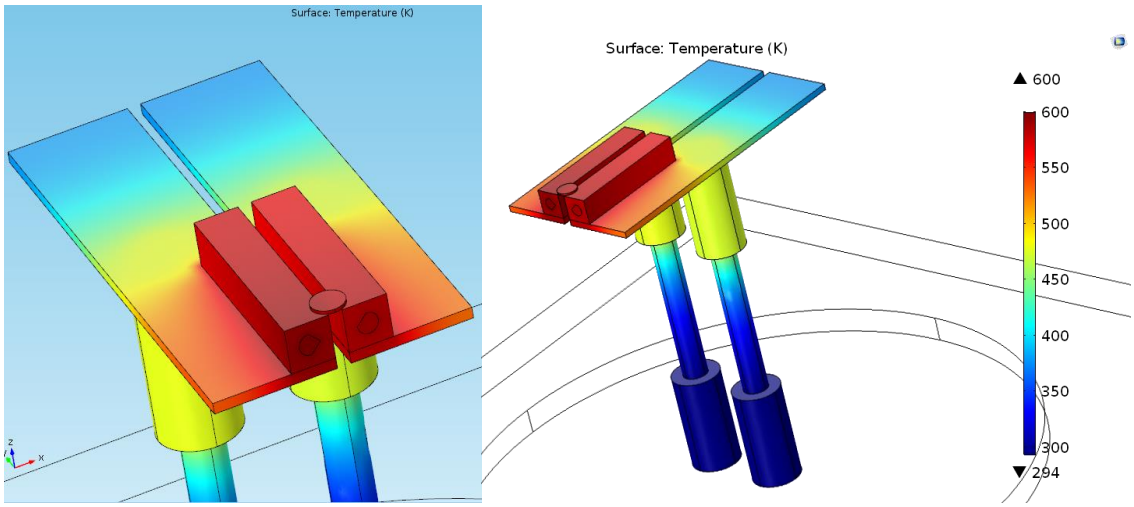

Figure 2-17 Temperature profile inside the bell jar. The left side shows an enlarged view of the sample and heater while the right side shows the overall temperature distribution from the base to the sample.

Figure 2-17 presents the simulation results of the targeted measurement unit inside the bell jar. Due to the resolution limitation, the temperature difference on the sample itself is not clearly presented. By switching the hot and cold side temperature between 600K and 590K, one gets a better description of the simulated temperature distribution on the sample itself.

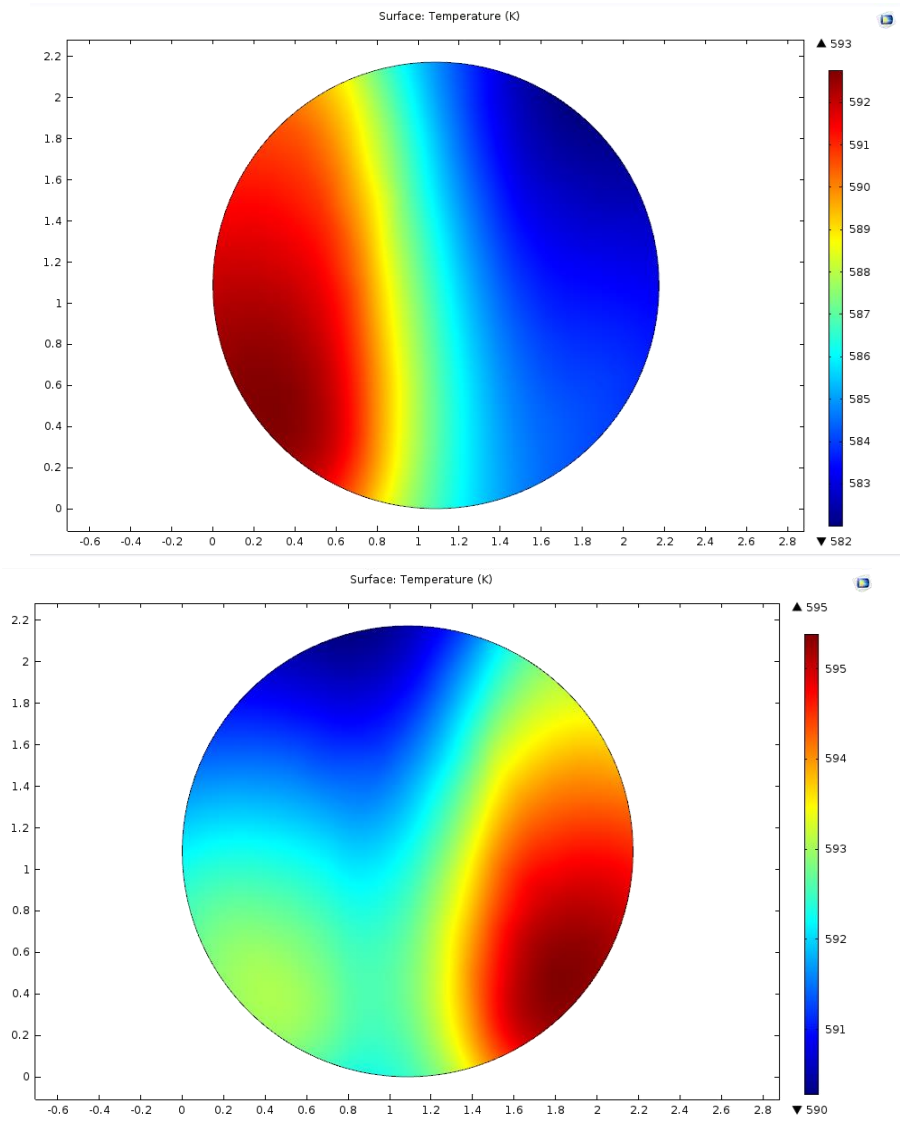

Figure 2-18 Temperature profile at the sample surfaces. The upper image shows when the hot side is located on the left and lower image shows the opposite case. The symmetric temperature profile illustrates the symmetric heat loss at both ends.

With the help of the simulated results, the thermal flow can be better monitored to reduce the heat loss from the core parts of the measurement units. By comparison of the simulation and experimental work, more information about the detailed temperatures can be obtained.

2.5 Error analysis and discussion

The measurement errors for this self-built instrument arise from both random and systematic errors. Random errors result, in part, from thermal instabilities, electrical noise, offset voltages, and other, fluctuating, stray voltages. In all of our measurements, the contacts are verified beforehand using V-I curves to verify Ohmic contacts between the probes and the samples, which can greatly reduce errors from offset voltages. During Seebeck coefficient measurements, temperature instabilities (up to 0.1 K) on the surface of sample cannot be eliminated. Thus, while temperature and voltage are measured within about 1.5 seconds of each other, they are not exactly simultaneous. A similar situation occurs when electrical resistivity is measured. Small thermal gradients could create thermoelectric voltages that affect the resistivity results. The use of a single heater helps maintain the sample surface at a constant and uniform temperature; however, thermal instabilities cannot be eliminated completely.

Systematic errors may result from instrumentation, data acquisition processes, and calibration. Mackey *et al.*[62] described a systematic method for analyzing the uncertainties in both Seebeck and electrical resistivity measurements. Here we describe the uncertainty analysis of electrical resistivity as an example. In this case, since the electrical resistivity is calculated from the measured sheet resistance and sample thickness, its total uncertainty results from the propagation of every error source. For a typical electrical resistivity measurement, the thickness error is simply the resolution of the calipers compared to the minimum thickness of the sample, which is 0.6% in our measurements. However, the error contribution to sheet resistance is comparatively more complex as R_s is calculated from the LabVIEW program using $R_{horizontal}$

and $R_{vertical}$, as measured from the aforementioned van der Pauw method. For a single resistance measurement, van der Pauw[48] estimated the uncertainty brought by the probe spacing and the length of the probes for a regular disk shape. Similarly, the uncertainty can be calculated for the geometry of our measurements, and this contributes around 2.5% relative error. Additional error comes from the data acquisition system, which in our case consists of the Keithley 2182A nanovoltmeter and the Keithley 6220 precision current source. The specification parameter determines this contribution of the relative error to be about 2.9%. By combining the systematic and random errors together, the total relative error for the electrical resistivity measurements is about 4.1%.

The uncertainty analysis for the Seebeck measurements can be conducted in a similar manner. Combining the systematic error and random error introduced by temperature variance, the maximum total error is approximately 8.3%. The details of these calculations can be found in Appendix A Uncertainty calculation of Seebeck coefficient and electrical conductivity.

2.6 Thermal conductivity characterization technique

2.6.1 Laser flash method expansion

With the accurate measurement of the Seebeck coefficient and electrical resistivity, we still need information about the thermal conductivity in order to calculate the figure of merit for thermoelectric materials. For the measurement of thermal conductivity, the laser flash method is selected due to its excellent accuracy and repeatability. The laser flash method is aimed to

measure thermal diffusivity α, as well as specific heat C_p of bulk samples. Once α and C_p are acquired, the thermal conductivity k can be calculated with the density, ρ, through

$$k = \alpha C_p \rho \quad . \tag{2-11}$$

The principle of the laser flash method comes from a heat transfer analysis on a semi-infinite surface. Parker *et al.*[63] originally described this laser heating procedure and described the intensity profile of a Gaussian beam that is incident on the sample surface. The temperature rise at the opposite face is monitored as the time is takes for the thermal wave to be transmitted through the sample is related to the thermal diffusivity of the material. The time that it takes for the temperature at the opposite surface to reach half is its maximum value, $t_{1/2}$, is used for evaluating the thermal diffusivity of the sample from

$$\alpha = 0.1398 \frac{d^2}{t_{1/2}} \quad . \tag{2-12}$$

According to the assumptions of semi-infinite heat conduction, the sample has some limitations on the range of thicknesses that can be measured. One important rule of thumb is to keep the thickness to diameter ratio small enough such that the heat transfer in-plane will not affect the out-of-plane temperature change, which is also the reason that disk-shaped samples are preferred. However, this ratio cannot be too small due to the resolution limitation of the detector, which makes the ratio of 0.1 a reasonable balance.

If this magnitude length ratio is taken as a rule, one more step can be forwarded to expand the application to square shape samples as long as the half-length can meet this rule. On the other hand, having the ability to measure square shape sample is of great importance in sample

fabrication. Due to the extraordinary hardness of most thermoelectric materials, it is difficult to fabricate the raw material to any desired shape, especially for perfect disk shaped samples. Thus, it is common to replace the disk shaped sample with a polygon shaped sample. However, cutting the material into a square shaped sample is relatively easy. With the use of an additive manufacturing technique, a prototype square sample holder was designed and fabricated.

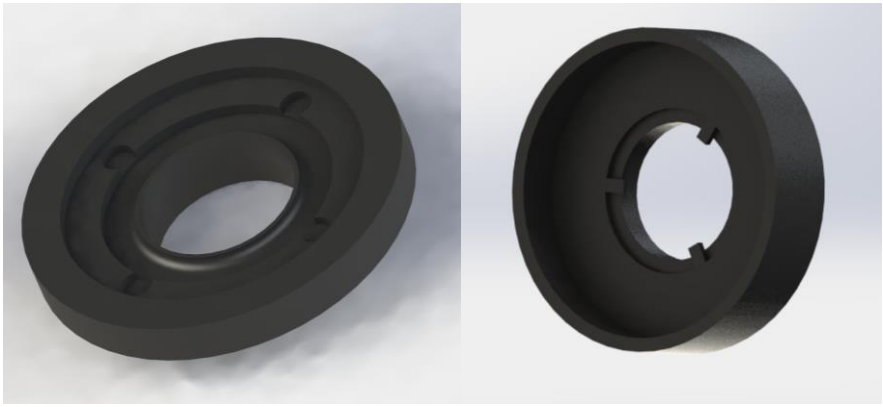

Figure 2-19 Computer model of a 3D printable square shaped sample holder

Figure 2-19 shows the 3D view of the square shape sample holder. As a fast-fabricated prototype holder, it skipped the long process of mechanical cutting, providing more dimensional details in a short period of time. Though the plastic holder cannot sustain high temperature heating, the final version of the sample holder was produced based on this prototype.

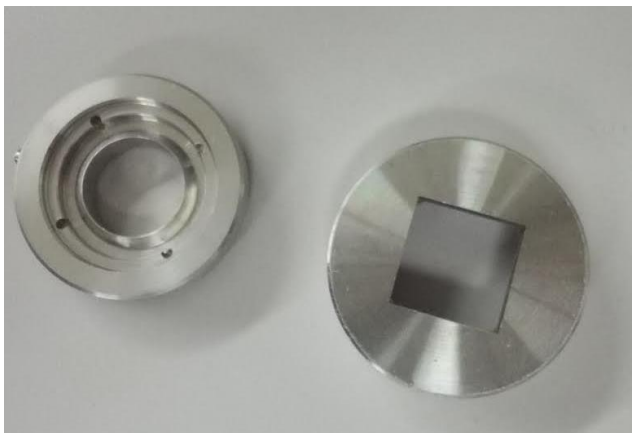

Figure 2-20 Final version of a stainless steel sample holder for laser flash measurements.

Figure 2-20 shows the final version of the stainless steel sample holder. The calibration results are shown below, compared to the reference value[64].

Table 2-2 Calibration of Stainless steel sample holder using Tantalum

Temperature in C°	Diffusivity in mm^2/s	Reference Value
100	24.18	24.08
200	23.83	23.97
300	23.56	23.87
400	23.38	24.15

2.6.2 Effects of porosity on thermal conductivity of copper

With the laser flash method, I also completed some research about the effects of porosity on thermal conductivity of copper. The copper itself is intended as a raw material for metallic 3D printing. Due to the inevitable porosity in the manufacturing process, the thermal

conductivity of the fabricated product is unknown. By studying a variety of porous copper samples, a modified Wiedemann-Franz equation was proposed to explain the relationship between the thermal conductivity and electrical conductivity of porous copper.

Warnes [65] suggested that for some metals, the normal Lorentz number needs to be modified to better describe the electronic contribution to the total thermal conductivity. According to this method and the Wiedemann-Franz law shown below, the relation between the density, electrical conductivity and thermal conductivity can be written as

$$k = LT\sigma + k_{lattice};\ \ k = k_e + k_{lattice}, \tag{2-13}$$

where L stands for the Lorentz number, T is the absolute temperature, σ is the electrical conductivity and k_l is the lattice component of thermal conductivity. The total thermal conductivity is the summation of the electronic contribution and lattice contribution. We investigated the relation between density and electrical conductivity first.

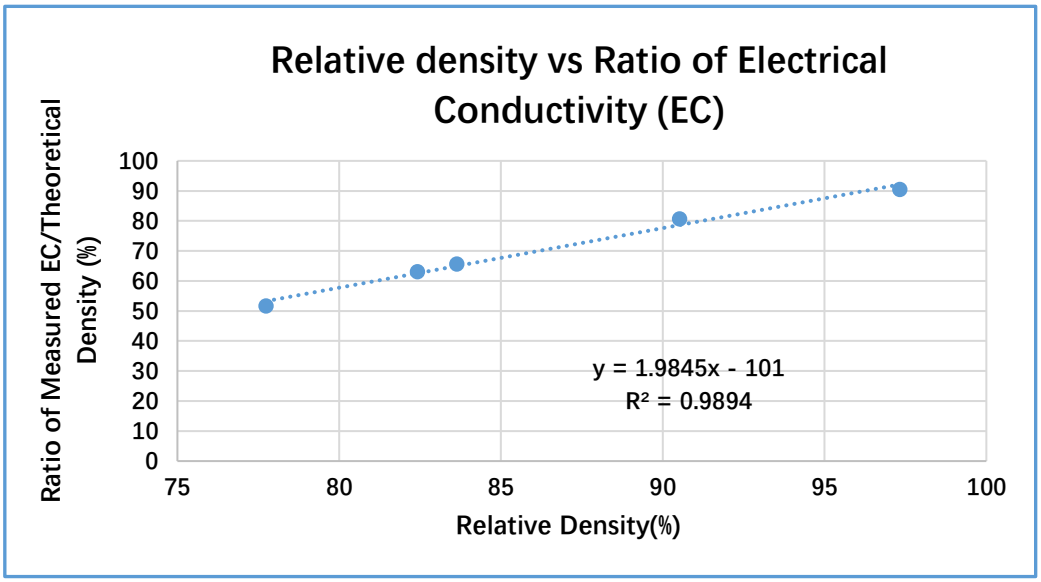

Figure 2-21 The linear relation between the density and electrical conductivity for porous copper.

The linear relation shows that porosity is important as holes in the composition of porous copper effectively reduce the density and impact the electrical conductivity in the same way. However, the porosity will affect the total thermal conductivity in a different way.

Table 2-3 Thermal conductivity of copper for different porosity values

Sample	Porosity	k_e from WF law	Total k	k_l
#1	0.1637	263.69	262.28	-1.41
#2	0.2227	207.80	245.72	37.92
#3	0.0948	324.21	293.52	-30.69
#5	0.1759	253.41	256.47	3.06
#6	0.0268	363.63	312.90	-50.73

It can be directly seen from the Table 2-3 that k_l is found as the difference between the measured total thermal conductivity and the calculated electronic part of thermal conductivity where this electronic component is determined from the measured electrical conductivity and the Wiedemann-Franz law. Obviously, a negative lattice thermal conductivity is impossible. One possible physical reason for the discrepancy is that the porosity could have an effect on the Lorentz number of the electronic contribution to the thermal conductivity. Another possibility is simply uncertainty in the measurements. However, when the lattice component is plotted as a function of porosity, the relationship is somewhat more clear.

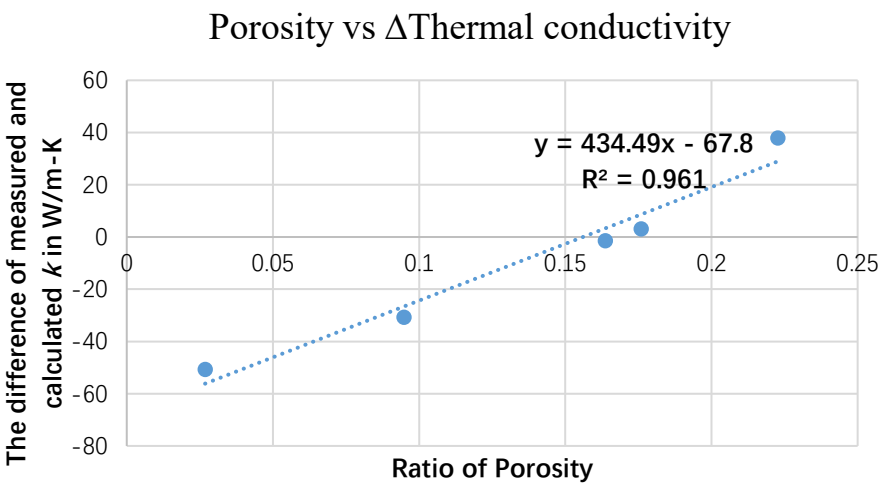

Figure 2-22 The k_l term in the W-F law is affected by the porosity level of the sample.

From this plot, the negative lattice components do not appear to be random errors in the measurement, as they appear to have a clear relationship with the porosity. Further measurements and analysis are required to fully explain these results.

2.7 Conclusion

In this chapter, I described the design and validation of a self-built Seebeck coefficient and electrical resistivity measurement system that operates in the temperature range from 300 K to 600 K and allows for measurements on samples of various shapes and sizes. The system measures the Seebeck coefficient with a quasi-steady state differential technique and electrical conductivity is determined with the van der Pauw method. Both measurements use a fast switch to measure temperature and voltage nearly simultaneously from adjustable probes. Validation measurements in the temperature range of 300 K to 400 K were made on a standard Bi_2Te_3 (SRM 3451) sample from NIST. In this temperature range, the Seebeck coefficient was within 3% and the electrical conductivity within 9% of values in the literature. At higher temperatures, up to 600 K, Seebeck measurements on four ZnO samples were within 10% of results obtained with a commercial system, and electrical conductivity was also within 6% of literature values for a Monel 400 sample. These results demonstrate the accuracy of the new measurement system. In addition, a brief discussion about the thermal conductivity measurement technique was also presented, showing the expansion of the laser flash method to accommodate square shaped samples and its application in the evaluation of porous copper materials.

Chapter 3 Characterization and development of thermoelectric material

3.1 Investigation high figure of merit skutterudites

In collaboration[66] with several others, I examined the development of $CoSb_3$ skutterudites as promising thermoelectric materials. By adding various guest atoms as fillers in nanocages[21], [67], [68], filled skutterudites are excellent candidates as high performance thermoelectric materials. They maintain high electrical conductivity like as a crystal, yet the filled nanocages are effective in reducing thermal conductivity. Among the various candidates, Yb doped skutterudites show great properties due to its ability to moderate carrier concentrations. However, the path to find a suitable electron accepter for doping is not easy. For Yb-filled skutterudites, there are limitations for its filling fraction which are not well understood. Along with collaborators, we completed the fabrication and characterization of a series of iron doped Yb-filling skutterudites in the formula of $Yb_xCo_{4-y}Fe_ySb_{12}$ (x ranging from 0.25 to 0.5, while y ranging from 0.1 to 0.5).

For the composition of the series of samples, we set the value of x equal to 0.25/0.3/0.4/0.5 and the value of y was equal 0.1 to 0.5 with a midpoint of 0.25. So the total number of samples in series was be 24. For several typical samples, we present the results here in Figure 3-1.

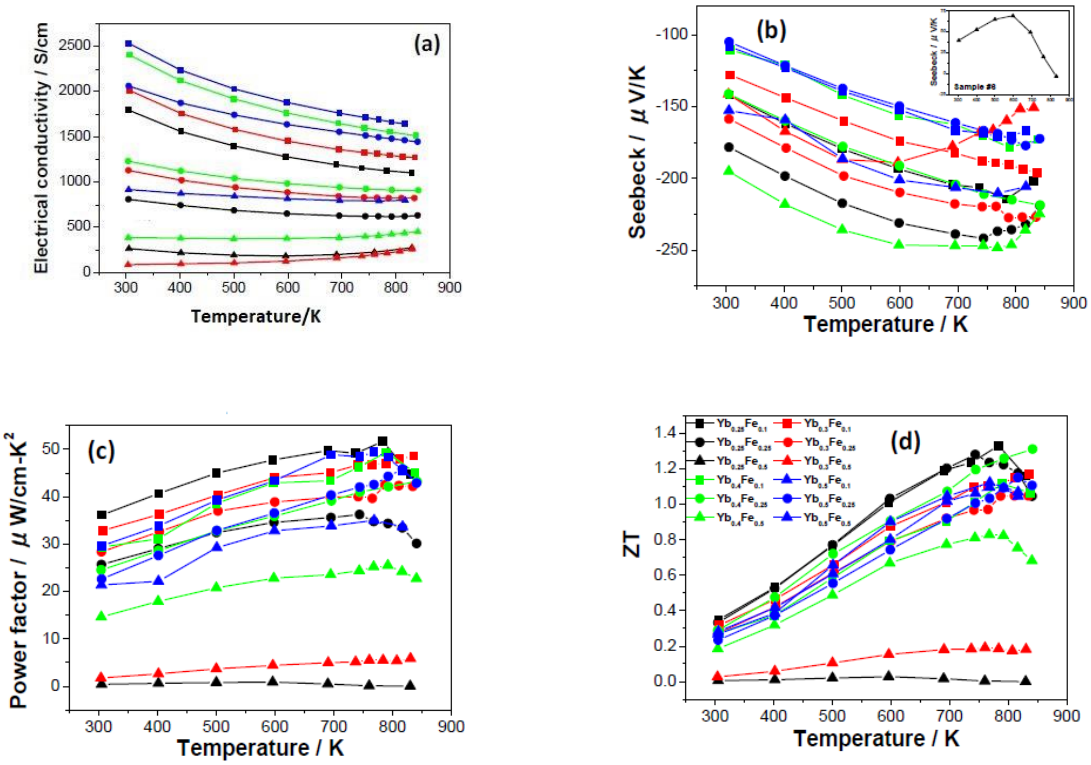

Figure 3-1 Characterized properties of selected samples from group. (a) electrical conductivity; (b) Seebeck coefficient, which has an distinct curve for Sample #6; (c) calculated power factor; (d) overall figure of merit *ZT* value and nominal composition.

Most samples follow the trend that electrical conductivity increases with the increasing temperature, proving their semiconductor behavior. For the role of Yb and Fe doping, since Yb acts as an electron donor while Fe is an acceptor, they have different influences in the change of electrical conductivity. For a fixed level of iron doping, the electrical conductivity increases with an increase in the doping level of Yb due to the donor enhancing the carrier concentration. Meanwhile, the trend is opposite for the role of Fe, which acts as an acceptor. For the performance of the Seebeck coefficient, the key phenomenon is the bipolar effect that decreases the high temperature Seebeck coefficient, especially above 600 K. Combining all of these

effects, the total value of the power factor remained at almost the same level for most high-performance materials, showing that the slight increase in the Seebeck coefficient was balanced by the decreasing trend of electrical conductivity with increasing temperature.

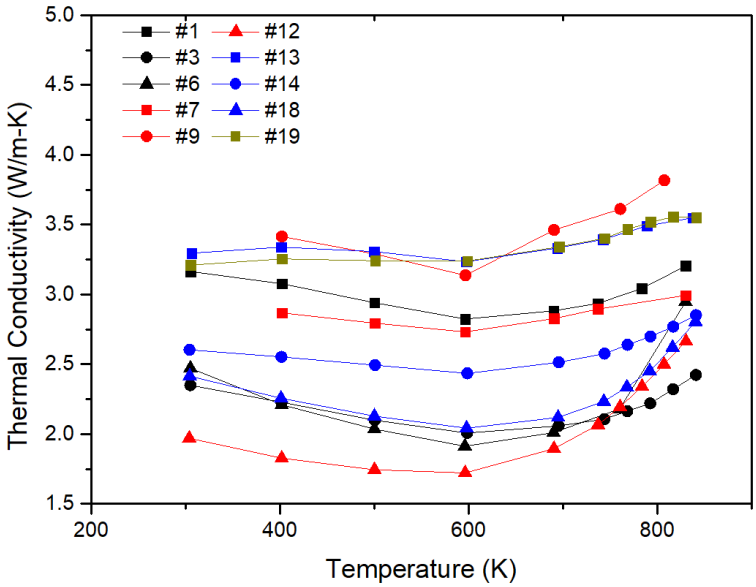

Figure 3-2 Temperature dependent thermal conductivity measurement results for skutterudite samples.

One outstanding performance of this series of samples are the ultra-low thermal conductivity values. Figure 3-2 presents several selected values of thermal conductivity in the temperature range from around 300 K to 800 K. These low thermal conductivity values contribute greatly to the final enhancement in the thermoelectric figure of merit, which is shown in Figure 3-1(d). The observed low thermal conductivity may result from the microstructure that the doping brings to the local atoms, where $CoSb_3$ has nano-size grains formed by the high-energy ball milling in the fabrication process. Both the Yb filler and Fe

substitution act as low-frequency scattering sites with their grain size, effectively reducing the phonon transport at these frequencies so that the total thermal conductivity is reduced while keeping a decent electrical conductivity value[6].

Some attention was also given to the development and characterization of novel *p*-type skutterudite materials. Similar to the case for *n*-type thermoelectric materials, the reduction of thermal conductivity by phonon scattering is an effective route to creating a high figure of merit. Nolas *et al.*[69] proposed that the random distribution of fillers will generate point-defects on microstructure, thus scattering a larger spectrum of phonons than for a fully-filled scenario. Furthermore, by introducing multiple kinds of fillers into the cage-like structure of skutterudites, there is a higher chance that the different sizes of point defects will scatter a relatively broad range of phonons. Based on that theory, we used a La filled skutterudite system in the form of Fe_3CoSb_{12} as the fundamental formula. Then multiple kinds of fillers such as lanthanum (La), titanium (Ti), gallium (Ga) and other elements were added into the formula to explore better thermoelectric material.

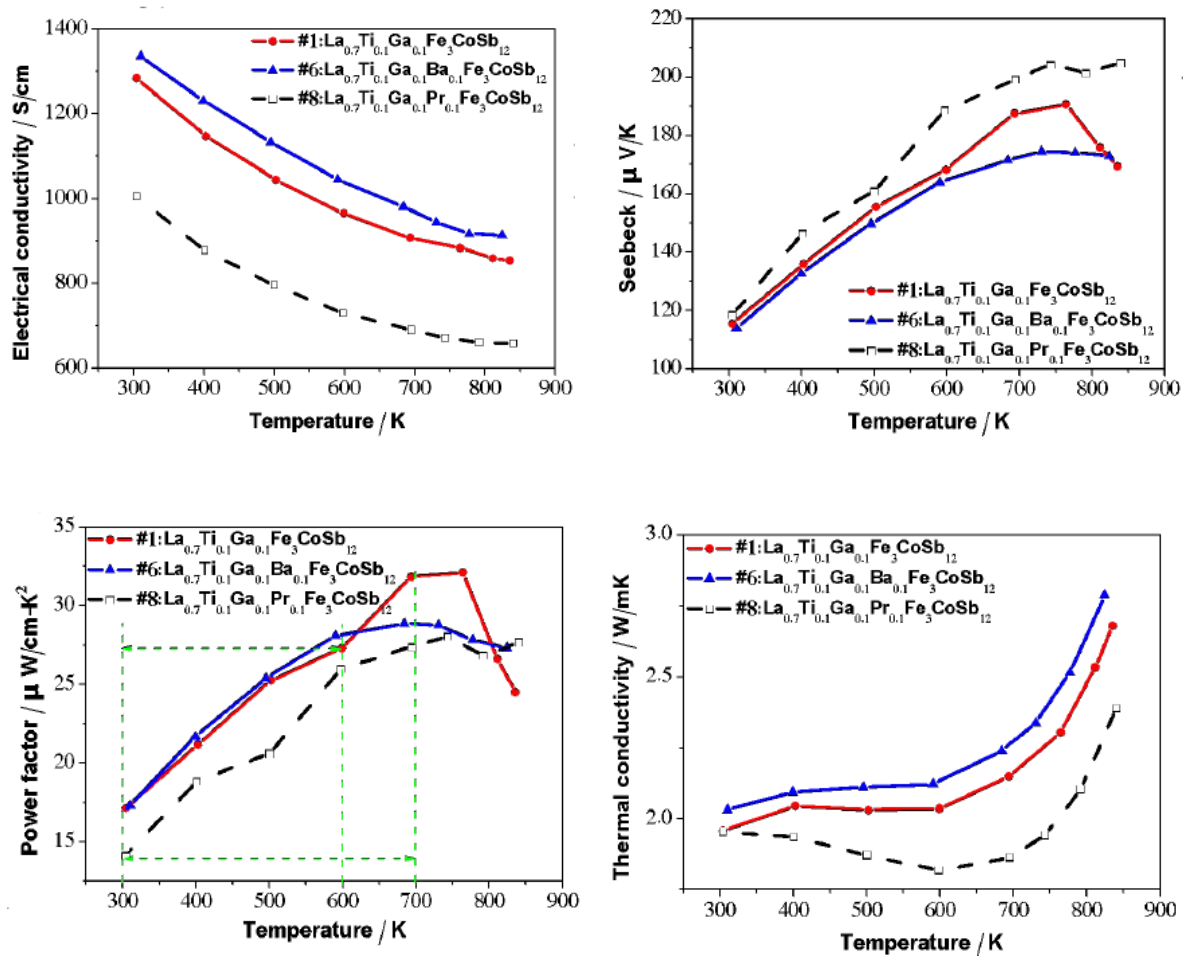

Figure 3-3 The electrical conductivity, Seebeck coefficient, power factor, and thermal conductivity of selected multi-filled *p*-type skutterudites. The addition of praseodymium (Pr) as heavy donors is effective in improving the performance of the material.

Figure 3-3 presents the measured thermoelectric properties of multi-filled *p*-type skutterudite materials. The composition of sample #1 can be taken as the base formula, which already shows decent electrical conductivity and Seebeck coefficient. Furthermore, with the addition of heavier atoms such as Ba and Pr, different effects are shown. For carrier donors as Ba, the increased carrier concentration is beneficial to the electrical conductivity while lowering the Seebeck coefficient slightly. The carrier acceptor Pr will has the inverse effect on

the performance. The reduction of carrier concentration harms the value of electrical conductivity, but greatly reduces the thermal conductivity, which is more useful in the point view of the overall *ZT*.

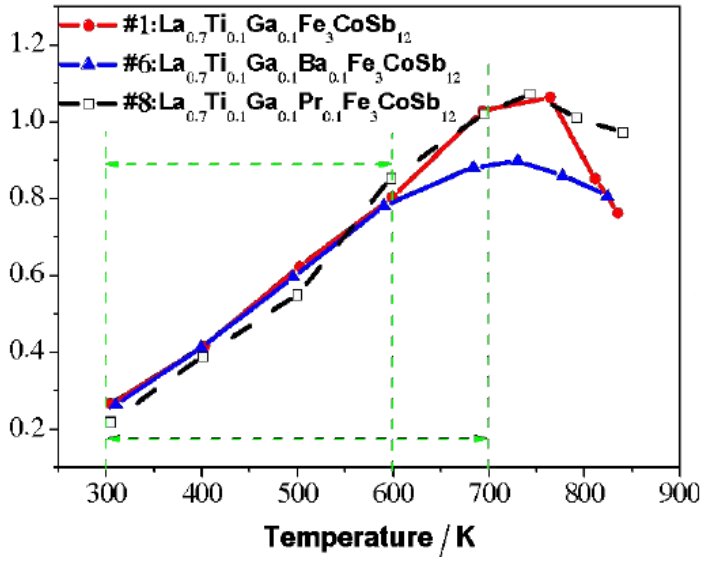

Figure 3-4 Overall *ZT* performance of *p*-type multi-filled skutterudites. The maximum *ZT* reaches about 1.1 at around 740 K.

Figure 3-4 illustrates the temperature dependent properties of the aforementioned compositions. All samples experienced a bipolar stage after 700 K around its maximum *ZT* point. This value is close to the best-published ZT value[70] (1.13) for similar material.

In conclusion, different methods were taken to improve the figure of merit in both *n*-type and *p*-type skutterudite materials, respectively. For *n*-type materials, the filling fraction limit is used as a reference to locate the optimum doping ratio of Yb and Fe, successfully decreasing the total thermal conductivity and reaching a maximum figure of merit of around 1.27. For *p*-

type material, multiple kinds of donors having different grain sizes are introduced to scatter a broader range of phonons. The effective reduction of thermal conductivity also leads to an excellent figure of merit of approximately 1.1 at around 740 K.

3.2 Characterization of excess Te doping Bi-Sb-Te material

Bismuth telluride, as one of the most widely used thermoelectric materials in commercial thermoelectric modules at low temperatures, has been well developed through decades of research. For p-type bismuth telluride, excess Te doping of $Bi_{0.5}Sb_{1.5}Te_3$ is one of the potential candidates for *ZT* improvement. Te doping percentages ranging from 2% up to 15% were prepared by hand-milling and spark plasma sintering (SPS). After cutting and polishing the materials into about 2.6 × 2.6 × 8 mm bars and 10.0 mm in diameter and 1 mm thick disks, the thermoelectric properties were measured to characterize the role of excess Te in the microstructure. Figure 3-5 shows the Seebeck coefficient and electrical conductivity for $Bi_{0.5}Sb_{1.5}Te_3$ samples with excess Te doping up to 15%. Generally, the excess Te doping into the composition has a positive effect on the Seebeck coefficient while reducing the electrical conductivity, which keeps the total power factor almost identical for different doping levels. However, the increase in excess Te doping acted as scattering centers for phonons, which make the total thermal conductivity decrease with increasing doping levels of Te.

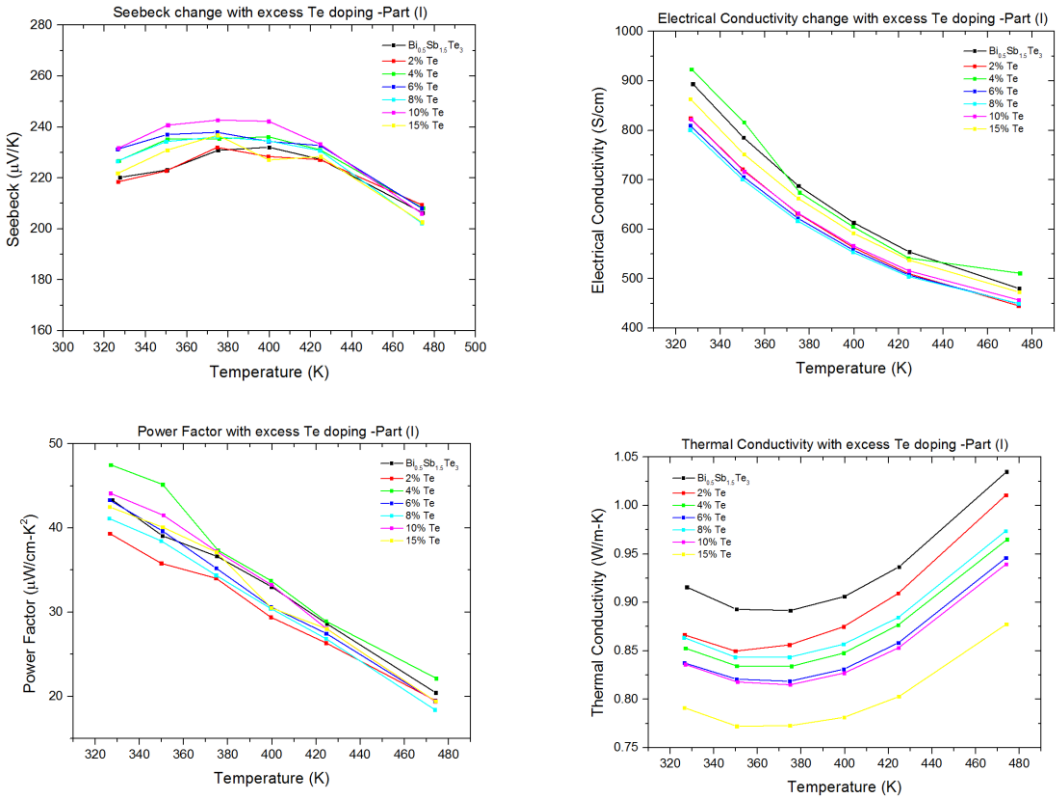

Figure 3-5 Thermoelectric properties of excess Te doped $Bi_{0.5}Sb_{1.5}Te_3$. The excellent electrical conductivity and relatively low thermal conductivity values makes a high overall *ZT* value.

As the result of the relatively high power factor with low thermal conductivity, the overall figure of merit, *ZT*, is shown in Figure 3-6 with a maximum value around 1.9 at around 350 K.

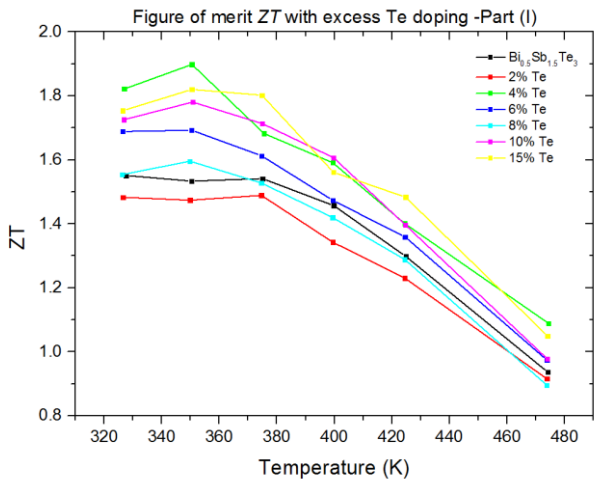

Figure 3-6 The figure of merit, *ZT*, for excess Te doped $Bi_{0.5}Sb_{1.5}Te_3$ up to 15% doping.

Increasing doping concentration was applied to pure Bi_2Te_3 compositions up to 70% using a similar method to investigate the limitation of excess Te. The initial idea of doping greater excess Te is to test the limitation of Te impacts on its thermoelectric properties. Thermoelectric properties were characterized and presented in Figure 3-7.

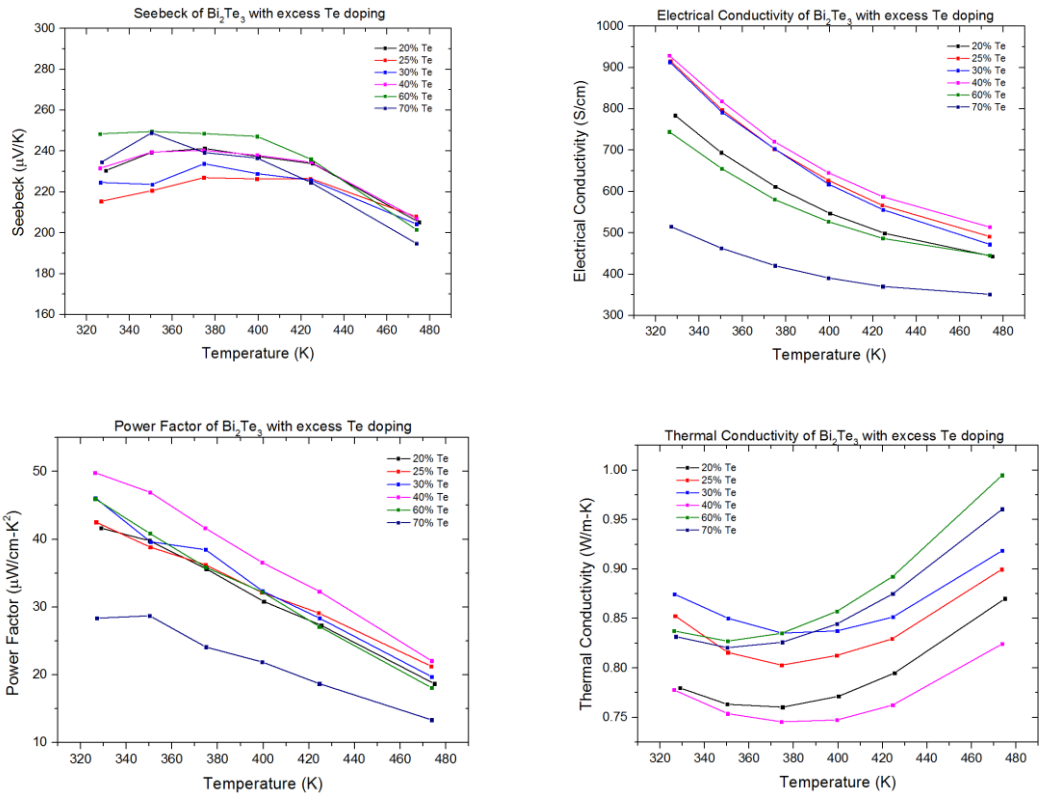

Figure 3-7 Thermoelectric Properties of excess Te doped Bi_2Te_3 from 20% up to 70%.

Different from the previous effects, excess Te doping acts differently with the increasing of doping level. High excess Te doping decreases the electrical conductivity due to the decrease of carrier concentration and too much Te doping will inversely enhance the thermal transport due to the concentration of excess Te. All of these effects made the sample with excess 30% Te doping have the best performances, as shown in Figure 3-8.

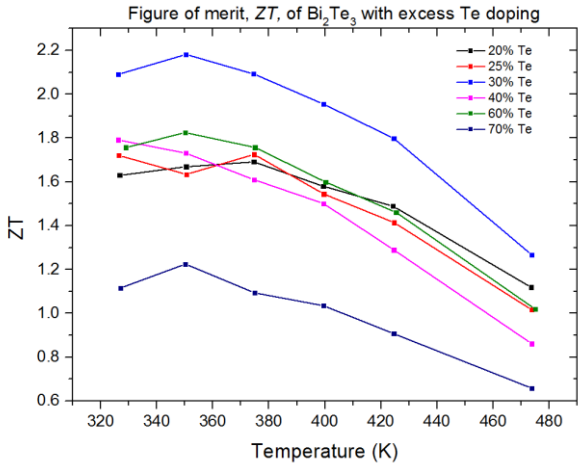

Figure 3-8 The figure of merit, *ZT*, for excess Te doped Bi_2Te_3 up to 70% doping.

For *n*-type bismuth telluride, $Bi_2Se_{0.7}Te_{2.3}$ with excess of Te and Se were fabricated using SPS as well. The replacement of Se in the Te position changes the carrier concentration of electrons, turning the overall composition into *n*-type.

Figure 3-9 presents the characterization properties. A general trend is the addition of Te enhances its Seebeck coefficient and electrical conductivity while Se functions in the opposite way. But the addition of Se will greatly help to decrease the thermal conductivity in the composition, which indicates a balanced concentration level combination is desired. Figure 3-10 shows the maximum *ZT* around 1.5.

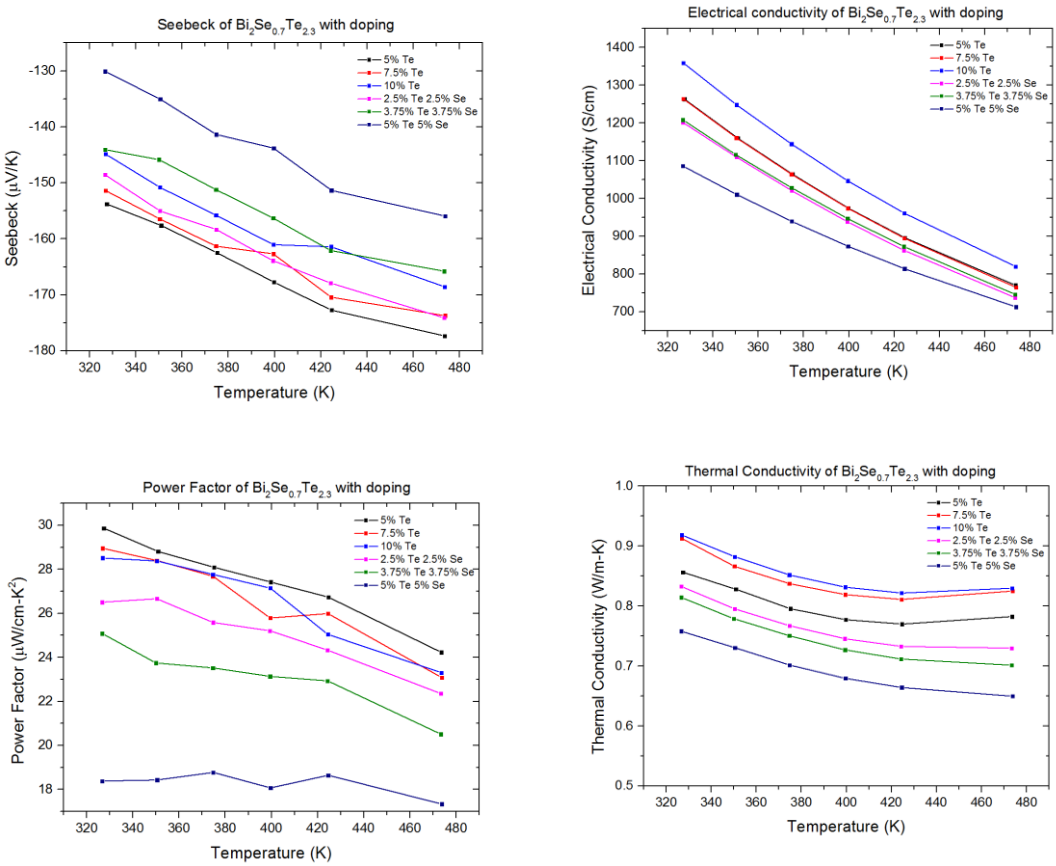

Figure 3-9 Thermoelectric properties of excess Te doped Bi_2Te_3.

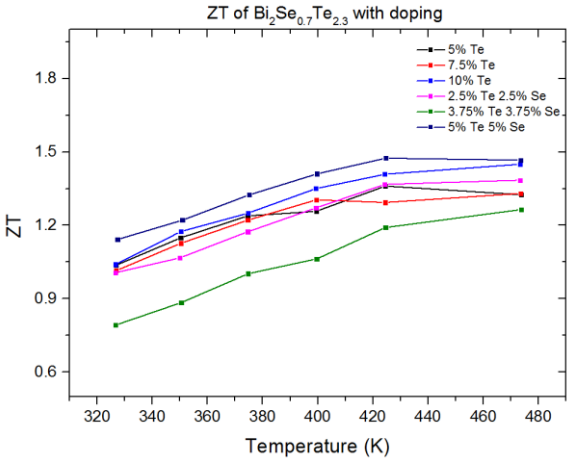

Figure 3-10 The figure of merit, *ZT*, for $Bi_2Se_{0.7}Te_{2.3}$ with excess Te and Se doping.

To determine the optimized composition for *n*-type bismuth telluride alloys, various compositions of $Bi_2Se_xTe_{3-x}$ with the same excess 0.2% Te were also fabricated by SPS. These samples were characterized and results are displayed in Figure 3-11 and Figure 3-12, showing transport properties and *ZT,* respectively.

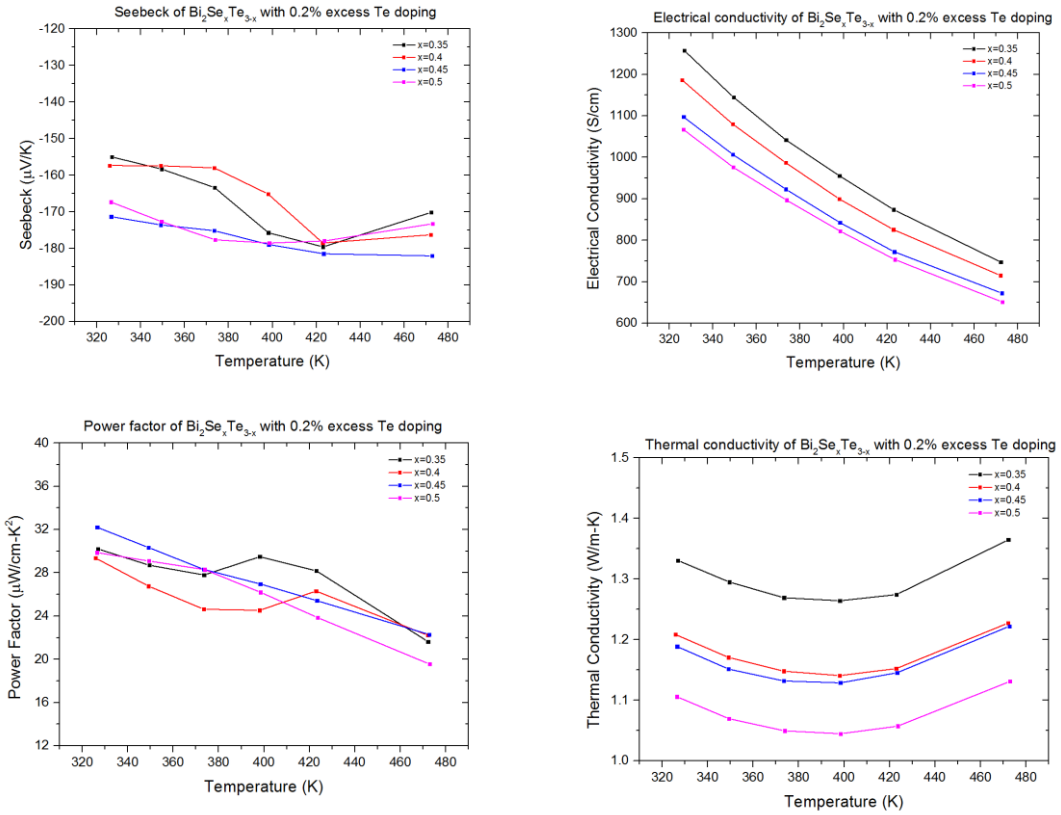

Figure 3-11 Thermoelectric properties of 0.2% excess Te doped $Bi_2Se_xTe_{3-x}$.

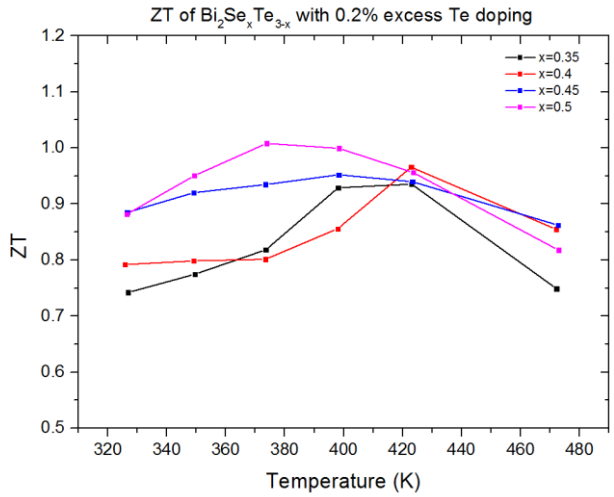

Figure 3-12 The figure of merit, *ZT*, for $Bi_2Se_xTe_{3-x}$ with 0.2% excess Te doping.

The role of excess Te is the key to the improvement of the figure of merit, as it increases the Seebeck coefficient while not significantly suppressing the electrical conductivity. Also, the excess doping functions as scattering centers[18] in both *p*- and *n*-type samples, successfully reducing the overall thermal conductivity, which leads to the increase in the figure of merit.

3.3 Exploration for high *ZT* half-Heusler alloys

Half-Heusler compounds also attract considerable attention as the potential candidates for high figure of merit thermoelectric materials, especially for high temperature applications around 800 K. By eliminating toxic materials such as lead and with great mechanical strength, multiple kinds of half-Heusler alloys are fabricated based on its ternary structure [71]. For this work, we focus on the development of *n*-type half-Heusler alloys with the composition of $(Hf_{0.6}Zr_{0.4})NiSn_{0.99}Sb_{0.01}$+*x* wt% Fe_2TiSn, which the has the general composition of XYZ where X and Y are selected from transition metals and Z functions as a group element. Different

from the regular formula, the addition of metallic phase nanoinclusions as dopants will greatly benefit the electrical conductivity. Furthermore, the nano-sized grains can act as scattering centers to reduce thermal conductivity[72]. The effectiveness of nanoinclusions and their optimal level is investigated by different doping levels and shown in Figure 3-13.

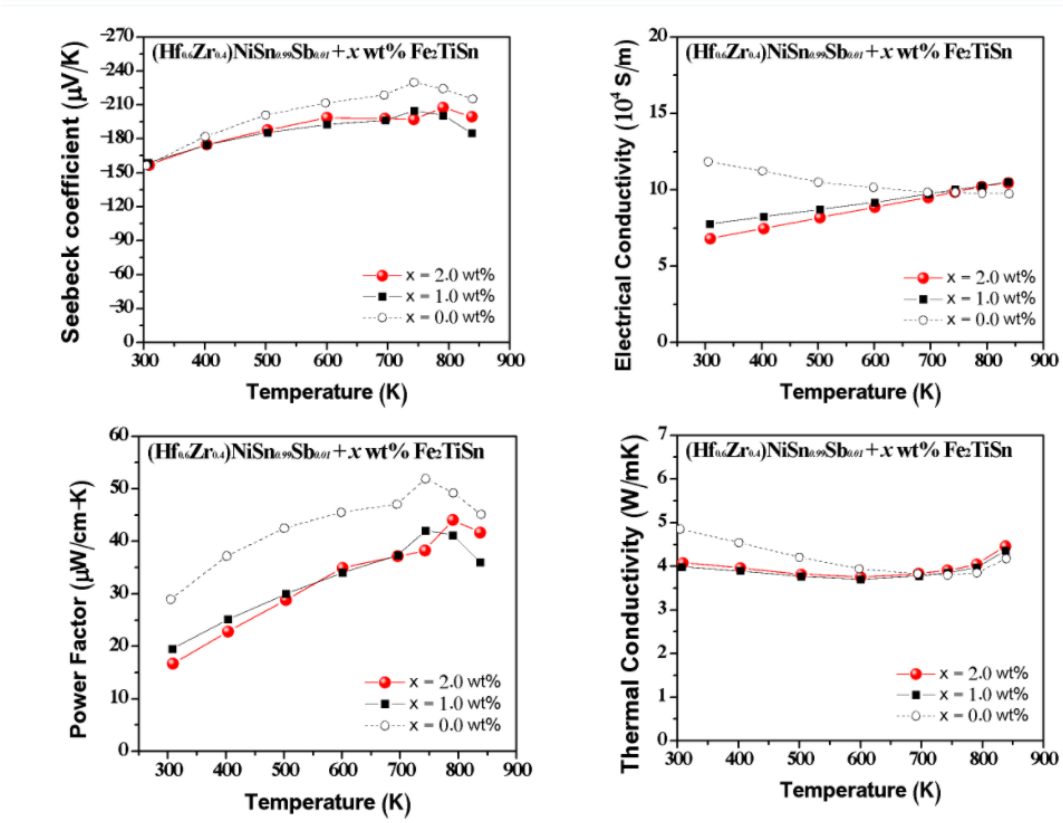

Figure 3-13 Characterized thermoelectric properties for *n*-type half-Heusler alloys.

The role of nanoinclusions can be determined by the comparison of the measured properties. Fe_2TiSn alloys can be considered as heavy-fermion Heusler type alloy doped into the half-Heusler structure[73]. By adding into the system, the controllable grain size can be chosen effectively to scatter phonons while not lowering the Seebeck coefficient significantly,

which can be confirmed with the measured result. The thermal conductivity of 1-2% level of Fe_2TiSn sample is lower than the one without the nanoinclusions.

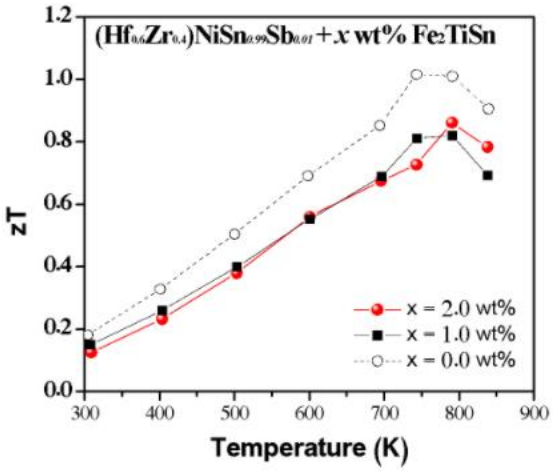

Figure 3-14 *ZT* improvement up to around 1.0 for *n*-type half-Heusler alloys.

However, the improvement in the thermal conductivity cannot compensate for the reduction in the Seebeck coefficient. Figure 3-14 shows the final calculated figure of merit for the nanoinclusion doped half-Heusler alloys. Unfortunately, the difference in Seebeck coefficient is the key factor, which decides the overall decrease in the figure of merit. Further enhancement towards the optimization of grain size is needed to recover the Seebeck coefficient decrease while keeping the thermal conductivity at a relatively low level.

3.4 Doping effects on $Ca_3Co_4O_9$ thermoelectric material

Compared to compound alloys, metallic oxide thermoelectric material distinguishes itself among other kinds of thermoelectric materials in high temperature applications with its excellent high thermal and chemical stability[74]. Since Terasaki *et al.* [75] reported single

crystal $NaCo_2O_4$ as a pioneer, a great variety of metal oxides have been developed for thermoelectric applications. Among them, layered cobalt oxides, such as Na_xCoO_2 and $Ca_3Co_4O_9$ can be regarded as complex crystals that are composed of more than two microstructures[76], which can moderate electron and phonon transport in a more balanced way.

Along with my collaborators, we developed several modified models based on $Ca_3Co_4O_9$. The first part of the work is to develop textured $Ca_3Co_4O_9$ with ion doping, in which the heavy atom Lu/Ga doping aiming for improved Seebeck coefficient from preferred orientation while reducing thermal conductivity as an extra scattering center.

For the second part of the work, we made some modifications with the type of ion doping. Instead of using Lu/Ga, we took advantage of the huge mass fluctuation by introducing Cd and Ca doping with Ag inclusion, trying to apply a dual-mode transport control mechanism for electrons and phonons, respectively. The role of the Ag additive is aiming for adding electrical connections for improving electrical conductivity and the large atom mass difference between Cd and Ca can consequently lead to chemical defects that affect low-frequency lattice vibrations, which can lead to a lower thermal conductivity.

Figure 3-15 presents the characterized properties of Lu and Ga doped $Ca_3Co_4O_9$. We also compared the effects of the sintering process between cold isostatic pressing (CIP) and spark plasma sintering (SPS). The results proved that SPS possesses more advantages than conventional sintering processes as it can bring more kinetics in the sintering process,

shortening the time of densification and also effectively limiting the grain size[77]. On the other hand, the doping effects of Ga and Lu are validated by the increase of Seebeck coefficients and the decrease of thermal conductivity simultaneously, which correspond well to our theoretical expectations.

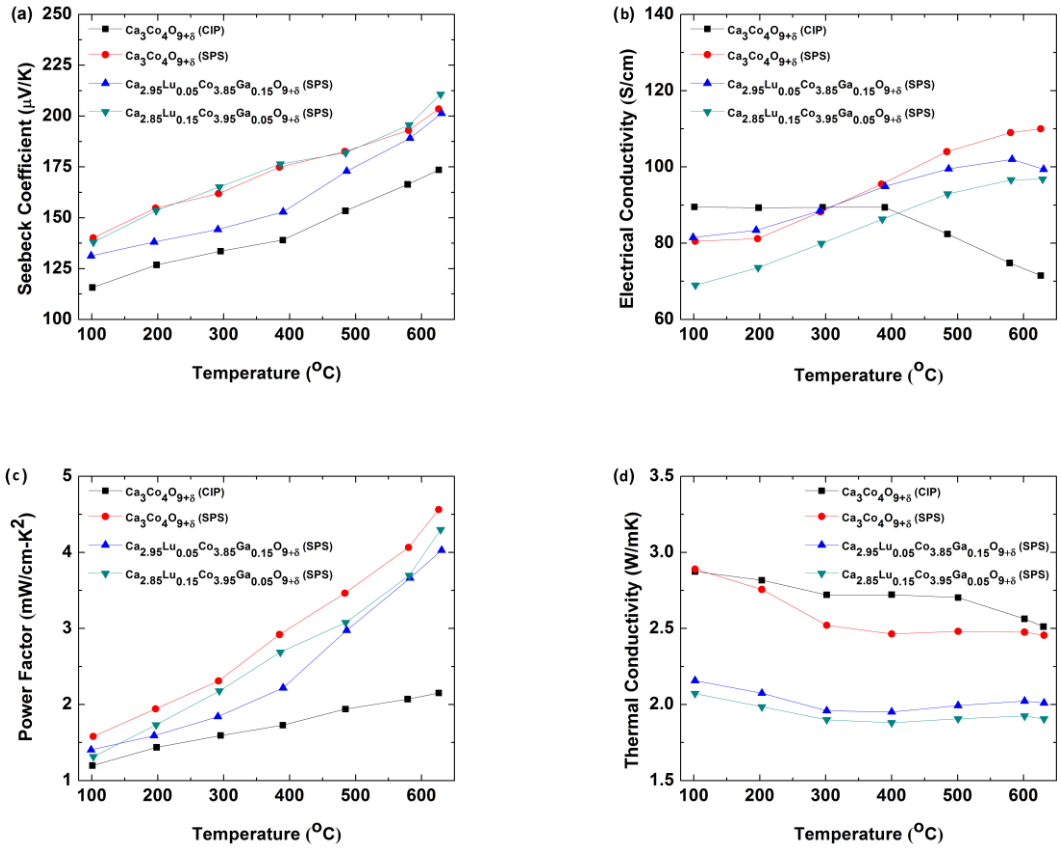

Figure 3-15 TE properties for Ca-Co-O based thermoelectric materials, fabricated by cold isostatic pressing and spark plasma sintering separately.

The improvement in Seebeck coefficient and thermal conductivity also reflect on the result of final figure of merit shown in Figure 3-16. Compared to the unimpressive *ZT* around 0.08 for cold isostatic pressed $Ca_3Co_4O_9$, the SPS fabricated sample and heavily doped sample

presented a much higher figure of merit of around 0.20. Though it cannot be compared to some extraordinary data collected from semiconductor alloys, it shows its ability to improve performance with the effective heavy atom doping.

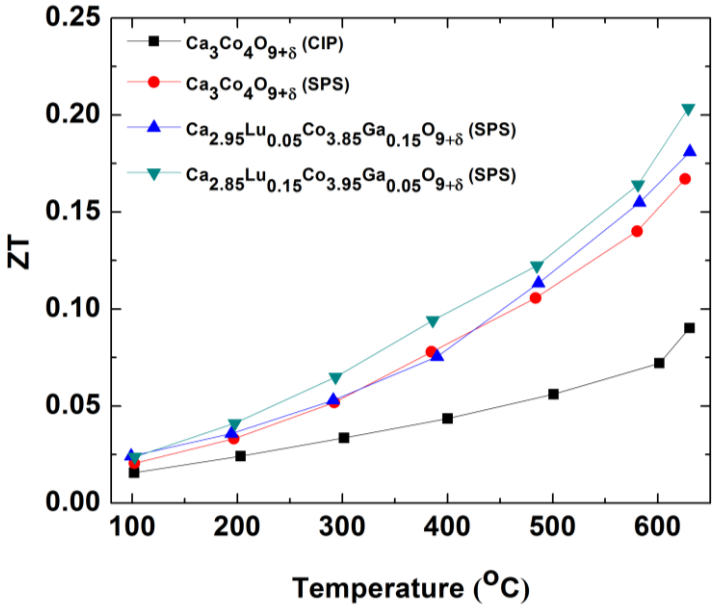

Figure 3-16 *ZT* greatly improved by applying spark plasma sintering method

Based on the experience of Lu and Ga doping effects, we applied a heavier atom, Cd, and separate metallic Ag inclusions to solve the relatively low electrical conductivity issue shown in Figure 3-15(b). The measured results are shown in Figure 3-17. By comparison with regular $Ca_{3-x}Cd_xCo_4O_{9+\delta}$ (x = 0 and 0.1), the Cd and Ag doped samples presented a higher Seebeck coefficient by increasing the overall carrier mobility. However, the significant drop of Seebeck coefficient for sample with 10% Ag addition may come from the large decrease in the effective mass, implying that the extra addition of Ag affects the Seebeck properties in an opposite way. Another point is that the addition of Ag inclusions increases the electrical conductivity and

thermal conductivity simultaneously, revealing the micro agglomerate metallic phase helps the transport of electrons and phonons. However, by finer control and optimization of the agglomerate size, the phonon increase can be suppressed, which would improve the figure of merit, *ZT*.

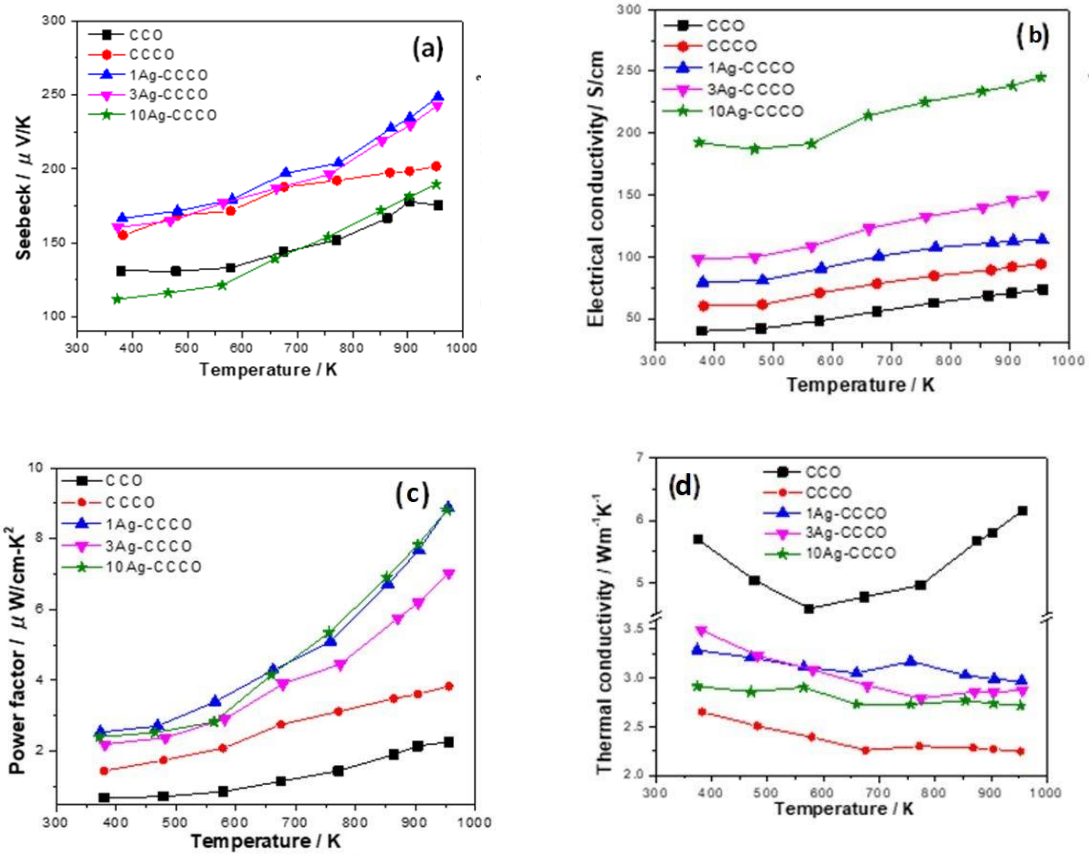

Figure 3-17 Thermoelectric properties of Ag inclusion doped CCCO and its comparison to the original composition. The role of Ag inclusions and the heavier atom Cd is an attempt to manipulate three properties in separate ways.

The improvement of Seebeck and electrical conductivity is also clearly shown in the increase of *ZT*, which is displayed in Figure 3-18. Except for the increase of thermal conductivity, the Ag doping proves its ability to increase Seebeck coefficient and electrical conductivity towards a better figure of merit. A finer control is desired for the distribution and size to further increase the benefits while sustaining the thermal conductivity increase at the same time.

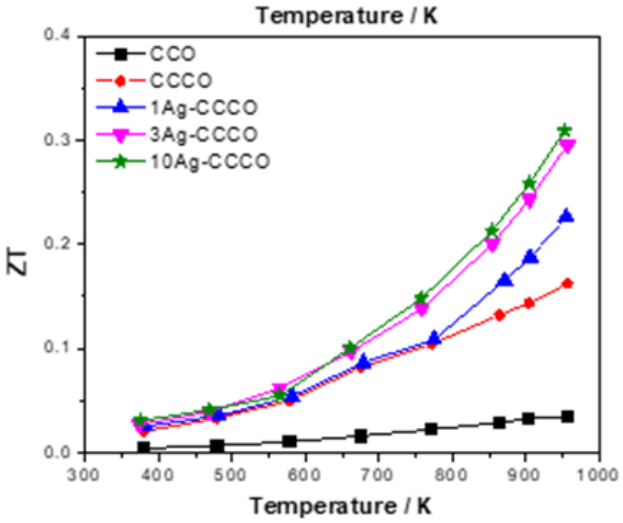

Figure 3-18 Overall *ZT* improvement by Ag and Cd doping.

In this part of the work, along with my collaborators, we finished the development of several novel thermoelectric materials based on the $Ca_3Co_4O_9$ structure by either adding Lu or Ga as heavy atoms, or introducing a non-balance replacement atom in Cd with the addition of Ag to improve the overall figure of merit. A significant increase of *ZT* can be observed after

doping, up to around 0.3 as a maximum for *ZT*. Further work will focus on finer optimization on the doped element microstructure to achieve better figure of merit.

3.5 ZnO electrical conductivity study and its functional graded structure

Compared to complicated lamellar structure of $Ca_3Co_4O_9$ and its related compositions, ZnO, as one traditional high temperature thermoelectric material candidate, has attracted continuous attention dating back to 1996[78]. Through around twenty years of development, this natural *n*-type wide-band semiconductor still suffers from low carrier concentration to achieve higher figure of merit[79]–[82]. One method to modify the electrical behavior for ZnO is the widely used doping method, especially for the doping of aluminum[80], [83], [84]. Meanwhile, the phase diagram of Al_2O_3 system shows that the function of Al doping is strongly correlated to the sintering temperature. At the same time, the sintering atmosphere will also affect the carrier density in the way of forming oxygen vacancies. In order to investigate the role of sintering parameters (temperature, initial condition and atmosphere), a set of ZnO samples doped with 2% Al powder[4] were fabricated with my collaborators and characterized in the self-built thermoelectric measurement setup.

The first set of comparisons was made between the same synthesized samples sintered in different atmospheres, air and nitrogen, respectively. Both samples are made using nano-size powders of ZnO and Al_2O_3 and went through ball milling for 48 hours. The only controlled parameter is the sintering atmosphere, which is set to air and nitrogen separately.

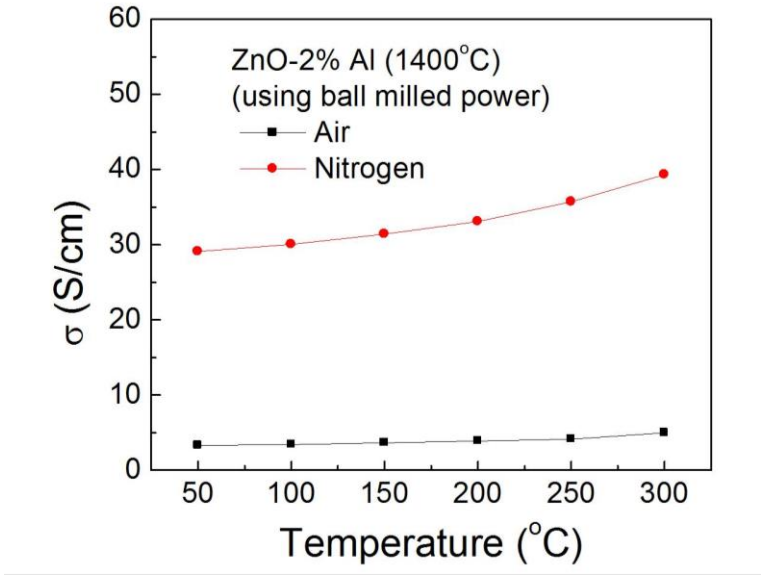

Figure 3-19 Electrical conductivity of ball-milled ZnO doped with 2% Al sintered at 1400 Celsius under air and nitrogen, respectively.

The electrical conductivity of ZnO sintered in nitrogen atmosphere presented superior properties than ZnO sintered in air with almost one order of magnitude improvement, shown in Figure 3-19. However, the absolute value of the electrical conductivity is considerably low.

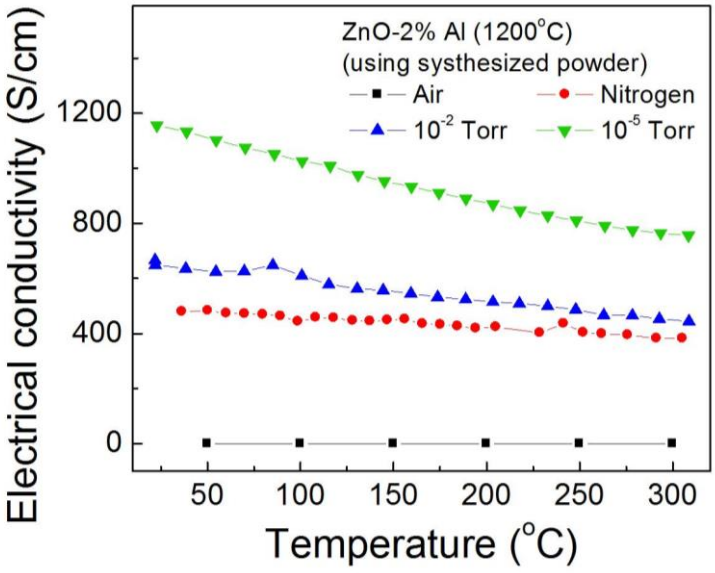

Figure 3-20 Electrical conductivity results of a group of chemically synthesized samples in the same 1200 Celsius under different atmospheres.

For both ball-milled ZnO samples, they are required to be sintered at a temperature of 1400 Celsius, which is relatively high. To overcome these challenges, an alternative sintering method using chemical synthesis is applied. Though the electrical performances of air sintered synthesized samples are relatively poor, the change in sintering atmosphere made the overall performances move towards a better direction. The samples fabricated in nitrogen atmosphere presented a reasonable electrical conductivity value, higher than both the air sintered samples and the ones that were made from a ball milling method. On the other hand, under certain vacuum condition, such as for 10^{-2} Torr or 10^{-5} Torr, the performance of the electrical conductivity is further improved as shown in Figure 3-20. The reason for the improvement is attributed to a higher carrier concentration in vacuum sintered samples, which helps to further increase the electrical conductivity.

The doping level will also influence the electrical conductivity in its own pattern. This set of samples was all fabricated from a chemical synthesis method, at 1200 Celsius and under 10^{-2} Torr. The only difference is that doping level is manipulated to 1-3 mol% of Al specifically.

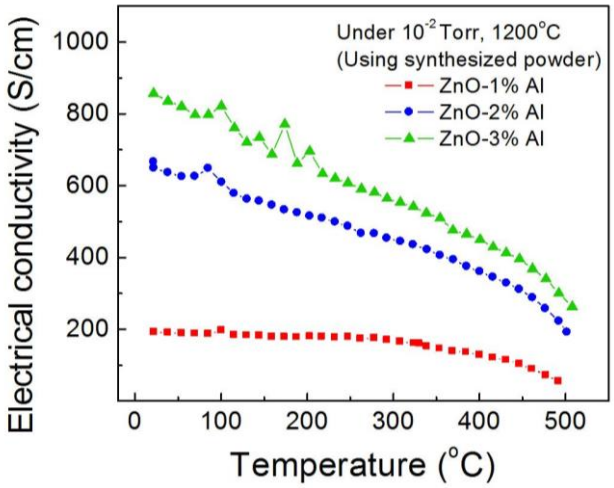

Figure 3-21 Electrical conductivity of chemically synthesized ZnO doped with 1-3% Al sintered under 1200 Celsius and 10^{-2} Torr, presenting an improvement of properties with increasing doping level.

Stronger carrier scattering at higher temperatures when the concentration is increased with more Al doping can explain the increasing trend shown in Figure 3-21. However, this trend has its own limitations due to the solubility of Al in ZnO. Meanwhile, some sintering parameters, such as sintering under vacuum conditions, can elevate the solubility to a higher level so that further increases in carrier concentration can be achieved. The optimization of this combination of parameters will be a topic for further research.

Another interesting topic related to ZnO is to build a functionally graded structure. Thermal shocks and stress, as well as rapid thermal fatigue contribute to a reduction in lifespan of oxide-based thermoelectric generators[85]–[87]. One method to mitigate thermal stress by composition is to apply grain size gradation. Large grains can spread heat more effectively than small grains with better stability, but small grains, even microstructures, can lead to a higher figure of merit and better efficiency[88]. To build a functionally graded material, a flexible

combination of various grain sizes is needed. Along with my collaborators, a 5-layer functionally graded structure was fabricated using grain sizes ranging from 180 nm to 1400 nm. Here the smallest grain layer and the largest grain layer were characterized.

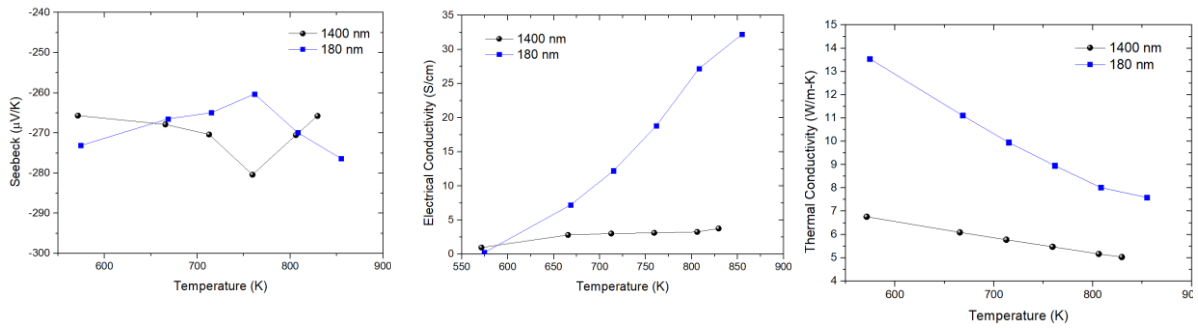

Figure 3-22 Seebeck coefficient, electrical conductivity and thermal conductivity properties of 180 nm layers and 1400 nm layers, respectively

A significant difference in properties is observed in these different grain size samples. Though the Seebeck value is similar and quite constant along the temperature, the electrical conductivity and thermal conductivity proved that small grains help the electron and phonon transport simultaneously. However, as the increase in electrical conductivity is greater, the overall performances in small grain material is expected to be better.

3.6 Conclusion

In this chapter, the development and characterization of multiple thermoelectric materials are presented and clarified. Based on the work from our custom built thermoelectric measurement system along with the optimization of commercial ZEM-3 and TC-1200

measurement units, thermoelectric materials including skutterudites, bismuth telluride based materials, half-Heusler alloys, $Ca_3Co_4O_9$ based compositions and Al doped or functional graded ZnO were fabricated, characterized, and analyzed. Methods for improving the thermoelectric properties such as heavy atom doping, metallic phase introduction and nanoinclusion addition were discussed and compared. In addition, a significant figure of merit increase was achieved for several samples and some of these materials have already been applied in thermoelectric generators. The developments and improvements of these thermoelectric materials provide several avenues to achieve a higher figure of merit, efficiency and thermal stability.

Chapter 4 Experimental evaluation of mechanical and thermal stability of GaSn interface layers

4.1 Introduction

Thermoelectric generators (TEGs) directly convert heat into electricity through the Seebeck effect. With increased interest in efficiency and the reduction of energy lost as waste heat, TEGs are desirable devices with significant attractive features such as having no moving parts, no emissions, and reasonable scalability. However, TEGs suffer from the fact that they possess relatively low efficiency. To improve the efficiency of an actual TEG device, the dimensionless figure of merit (ZT) of the thermoelectric material should be increased[4], [89], [90], and the overall system design can also be improved[5].

While considerable efforts have rightfully focused on the development of new materials, the importance of designing a robust system that can withstand operation at high temperatures through numerous thermal cycles cannot be overlooked. One critical and challenging aspect of fabricating TEGs with long lifetimes deals with creating reliable thermal contact between the TEG and the heat source as well between the TEG and the heat sink. Although improved fabrication techniques provide better mechanical contact at these interfaces, there will inevitably be some air gaps at the interfaces due to microscale surface roughness and non-planar surfaces and warping due to thermal expansion. Thus, a variety of thermal interface materials (TIMs) are used to fill these air gaps in order to increase thermal conductance through the interfaces. Compared to other types of thermal interface materials such as thermal

grease[29], or filled polymers[31], low melting point alloys provide a metallic path for heat transfer, easy pre-curing treatments, as well as potentially better performance at high temperature ranges. However, liquid metal alloys also may suffer from dry-out issues, as well as oxidation and corrosion problems, especially at high temperature cycles. Several studies[32], [91], [92] have already examined the use of low melting point alloys in low temperature ranges for applications such as in packaging of electronic devices. However, the performance and reliability of low melting point alloys for high temperature applications has not been investigated as broadly.

Galinstan is a commercial liquid metal alloy mainly consisting of gallium, indium, and tin. Low melting temperatures ensure that such eutectic alloys may function well as both hot- and cold-side thermal interface materials in order to enhance thermal contact conductance at interfaces. Compared to the relatively stable, and low, temperatures at the cold-side interface, the hot-side interface experiences larger thermal gradients, which leads to larger mechanical stresses resulting from thermal expansion as well as greater oxidation issues. In this work, we experimentally evaluate the mechanical and thermal stability of a commercial composition of galinstan consisting of 92% gallium and 8% tin. The liquid interface layer, applied between solid layers of AlN and Inconel, are tested for mechanical strength under static pressure. Also the thermal performance stability is tested on this interface layer. Finally, I discuss some changes that were observed regarding the morphology of the interfaces, and I briefly examine the application of GaSn layers onto real thermoelectric devices.

4.2 Procedure and Experimental Design

As shown in Figure 4-1, low melting point liquid metals are possible candidates as thermal interface materials to enhance heat transfer between a thermoelectric device and the hot-side heat exchanger (HEX). In addition to wetting surfaces with some degree of surface roughness, the idea is that the liquid metal will also maintain thermal contact between the TEG and HEX if there is some non-equal deformation of the materials due to mismatch in thermal expansion coefficients. To examine the behavior of the liquid metal when confined between solid layers, two sandwich structures were created that consisted of 4 mm x 4 mm solid layers of either aluminum nitride (AlN) or Inconel. The AlN is used as the electrical isolation layer in the TEG, and the HEX is made from Inconel. The first sandwich structure consisted of alternating layers of AlN (three layers) and GaSn (two layers), while in the second sandwich structure Inconel replaced AlN as the solid layer.

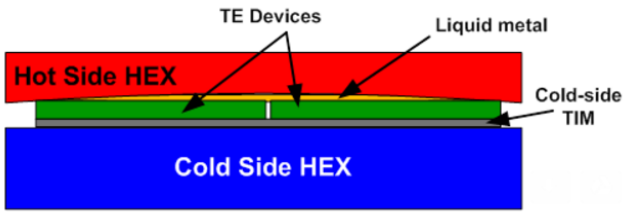

Figure 4-1 Schematic diagram of a thermoelectric generator system. Our interest in this work lies at the interface between the TEG and the hot-side HEX. Here a liquid metal is used as the interface material on the hot side of the device. The hot-side HEX is shown as being slightly bowed due to thermal expansion.

Galinstan is chosen as the liquid metal alloy for its stability and commercial availability. Our specific gallium tin alloy consists of 92% gallium and 8% tin and was obtained from *Alfa Aesar*. The sandwich structure was built in the following sequence, and then it was pressed with either (a) uniaxial pressing, or (b) cold isostatic pressing (CIP). First, the galinstan was completely melted into liquid form by heating to around 50 °C, and it was then applied uniformly on the surface of the solid layers in order to wet the surfaces. Finally, the sandwich structures were pressed together using either uniaxial pressing or cold isostatic pressing.

To evaluate the mechanical stability of the structure under static forces, the sandwich was compressed using a four-spring balanced pressure setup, as shown in Figure 4-2. The applied force was measured by the electrical resistance change of a thin film Flexi Force sensor. While the pressure was applied, the GaSn layer thickness was observed with a high speed camera (MEMRECAM HX-3) with 1.5 μm resolution. In addition to the application of compression forces, tensile forces could also be applied to the surface with an extension spring fixed to one of the solid layers. By examining the mechanical response of the structure under compression and tension, the stability of system when subjected to thermal expansion, which is the combination of compression and tension forces, could be better understood.

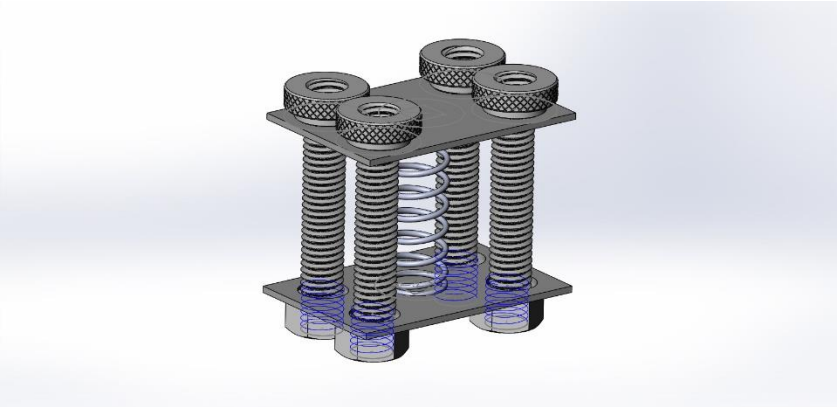

Figure 4-2 Three-dimensional diagram of the system used to apply compression to the sandwich structures.

For thermal treatments, the sandwich structures, built with solid layers of AlN or Inconel, were placed onto the same cartridge heater to test the galinstan performance on both materials. A controlled environment was provided in a bell-jar based setup shown in Figure 4-3(a). Figure 4-3(b) displays schematic diagrams of the measurement prototype for AlN and Inconel pieces. With simultaneous measurement of the surface temperature at multiple points, the quality of thermal contacts could be evaluated by the stability of temperatures during the heating period. The following microstructure analysis was made using scanning electron microscopy and energy dispersive x-ray spectroscopy (FEI Quanta 600 FEG environmental SEM with Bruker EDX).

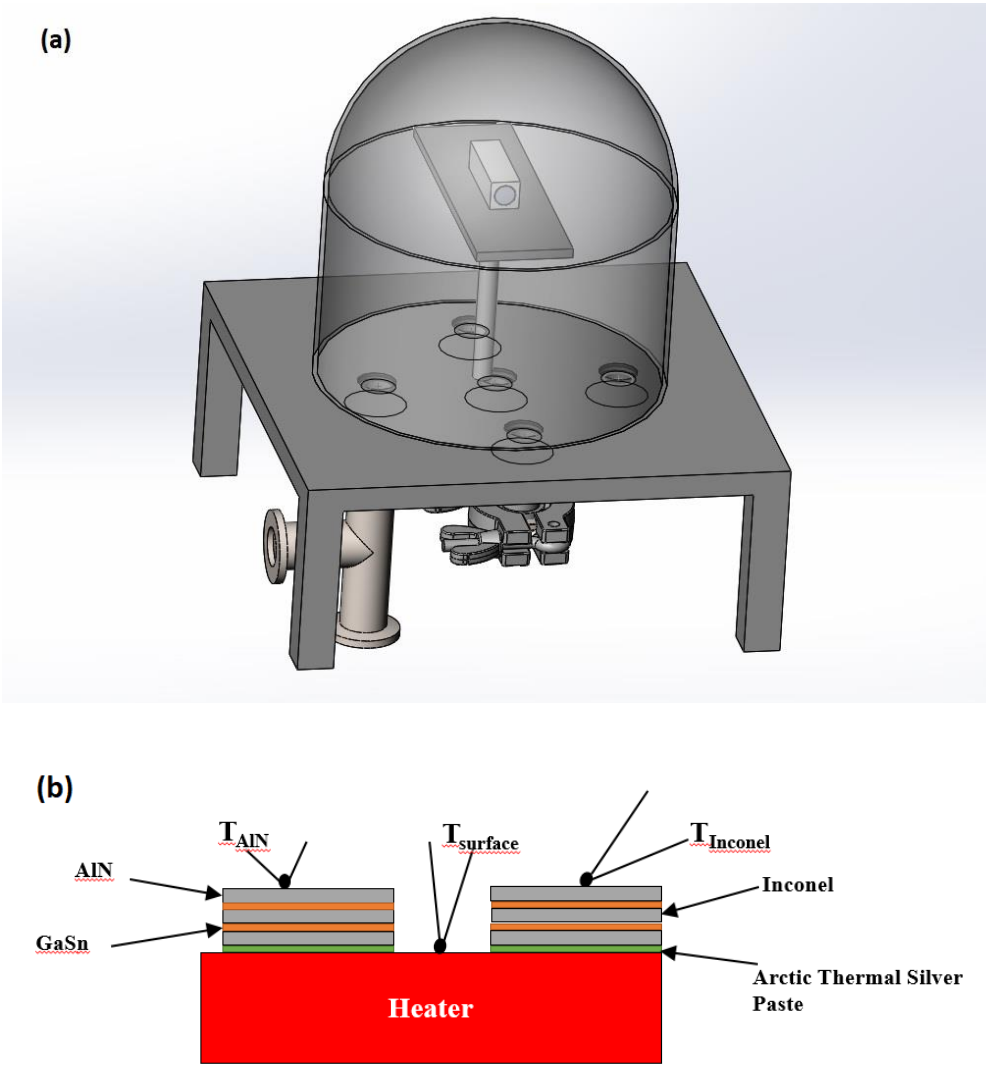

Figure 4-3 (a) Schematic diagram of the controlled bell jar system; (b) Test prototypes for AlN and Inconel sandwich structures. The sandwiches for each material consist of alternating solid (AlN or Inconel) and liquid (GaSn) layers. The thermocouples are attached for temperature measurements.

4.3 Results and Discussion

The sandwich structures are first tested to check the galinstan thickness change under uniform heating in a furnace. Figure 4-4 and Figure 4-5 display measurements of the GaSn layer thicknesses before and after thermal treatment at 700 °C in a furnace for 1 hour for

sandwiches made of AlN and GaSn. The upper subplots (Figure 4-4) show the thickness change for uniaxial pressed samples, and the lower subplots (Figure 4-5) present the isostatic pressed samples. By comparing the thickness change due to the thermal expansion during the uniform furnace heating treatment, the isostatic pressed samples showed improved stability compared to the uniaxial pressed samples. However, it is important to note that the pressures used for the isostatic pressed samples were much higher than for the uniaxial pressed samples, making layer thicknesses considerably smaller. Thus, it is not clear if the increased stability was simply due to the reduced layer thickness or if the high isostatic pressure helped the GaSn completely fill all of the voids between the layers by expansion force.

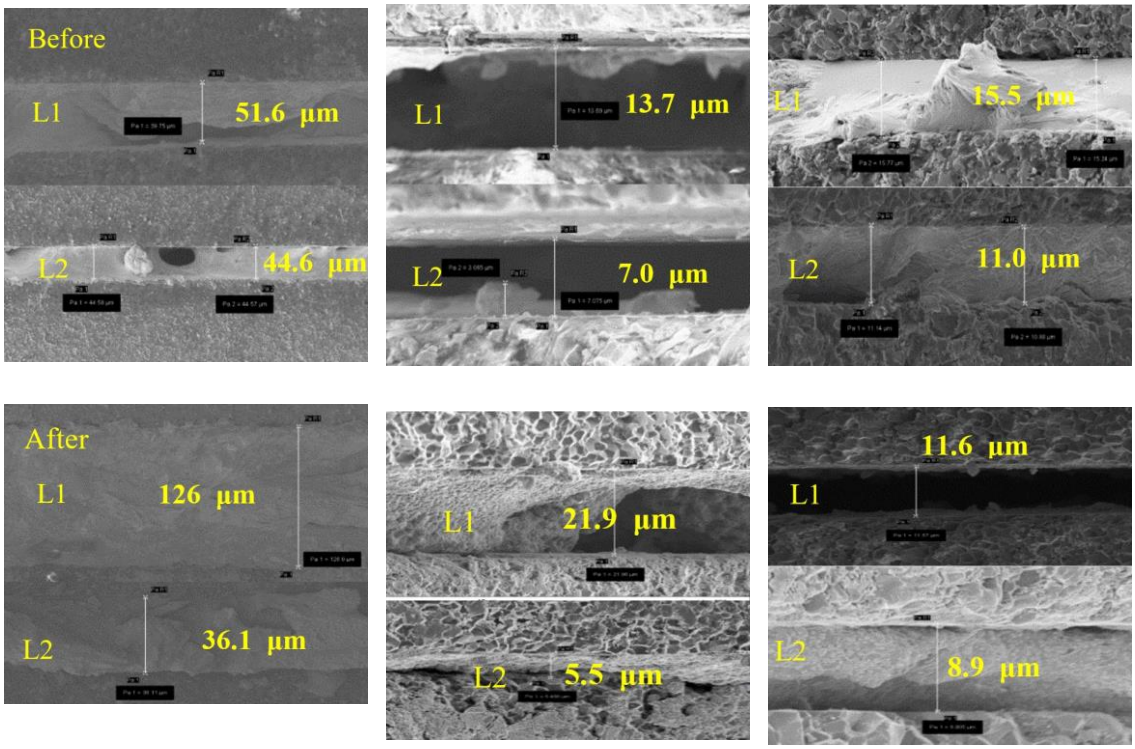

Figure 4-4 Scanning electron microscope measurements of the GaSn layer thicknesses in the uniaxial pressed sample before and after thermal treatment at 700 °C for one hour. The left column was pressed by hand, while the middle pressed with 0.5 lbf (~20 psi), and the right with 1 lbf (~40 psi) using an AlN piece.

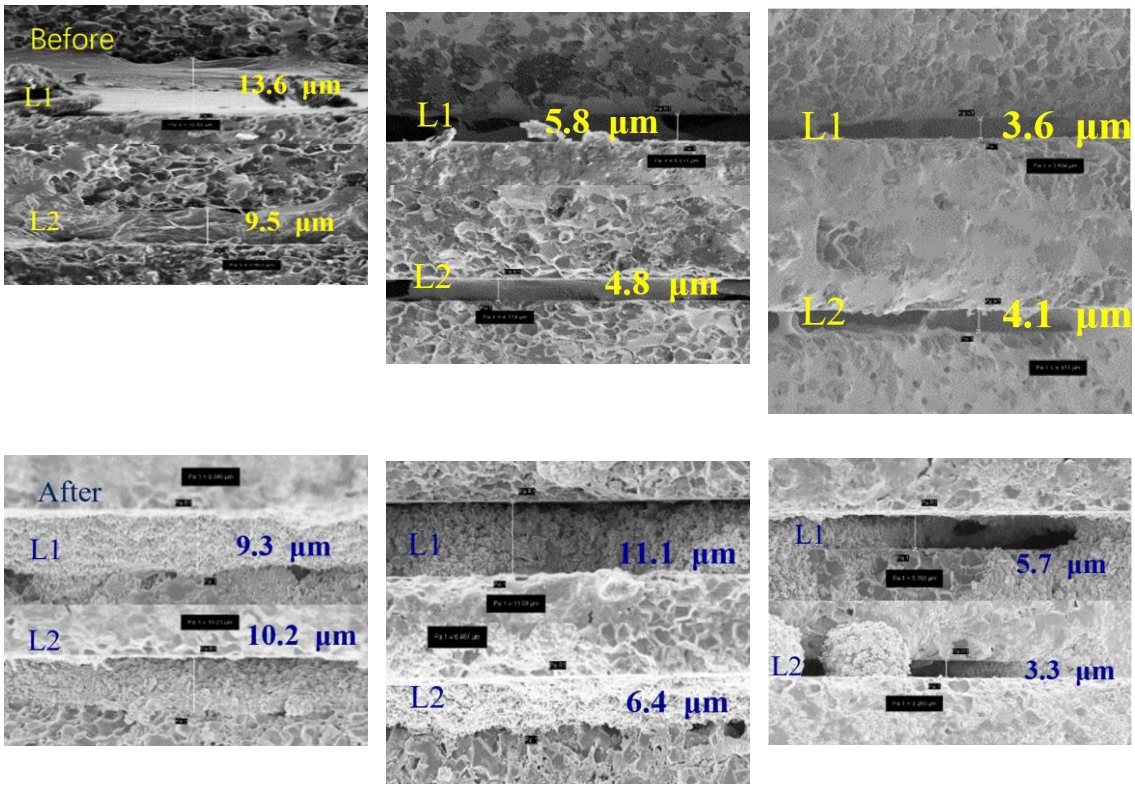

Figure 4-5 GaSn layer thickness change after thermal treatment at 700 °C for one hour for samples formed by isostatic pressing. From left to right, the three columns were pressed at 5 kpsi, 15 kpsi, and 30 kpsi, respectively, also using an AlN piece as the solid layer.

The GaSn intermediate layer shows similar behavior when acting under a perpendicular compression force using the pressure testing system noted above (see Figure 4-2) and shown in Figure 4-6. To verify that the applied force is correct, the electrical conductance response from the force sensor was calibrated first as shown in Figure 4-6. Also the deformation was recorded as well to confirm the value of the applied pressure. Figure 4-7 displays SEM images of the GaSn intermediate layer under static perpendicular pressures. A small notch in the AlN layer was used to mark the location to ensure that the observations occurred at the same location for each pressure. As shown in Figure 4-7 there was little noticeable or measureable change to

the interface layer for uniaxial pressures between 51 and 218 psi This pressure range was chosen as it represents a reasonable range of pressures we expect in a prototype TEG due to mismatch in coefficients of thermal expansion between the TEG and HEX. While the actual thickness of the GaSn layer is not measured directly in each panel, it is clear that the layer is stable and none of the GaSn is pumped out along the edge of the layers.

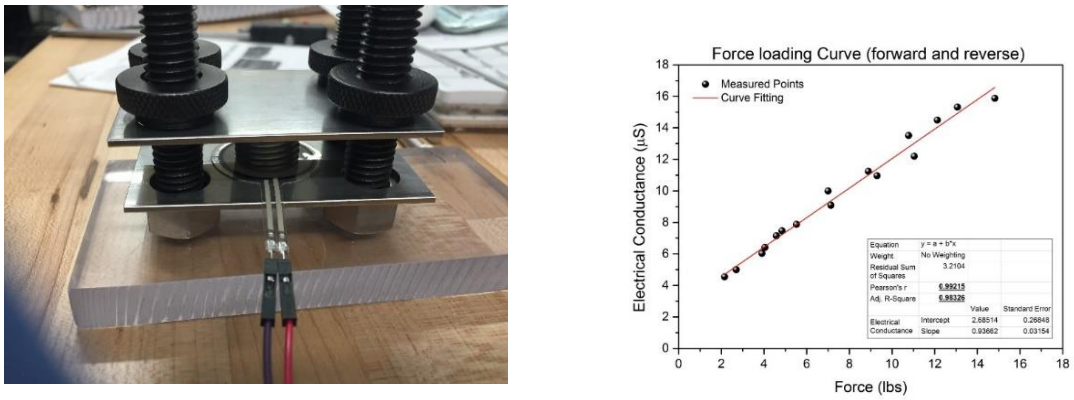

Figure 4-6 The left panel is a photograph of the tensile test setup, and the right panel shows the calibration of the linear relation between the output electrical conductance from the sensor and the applied force to the sensor.

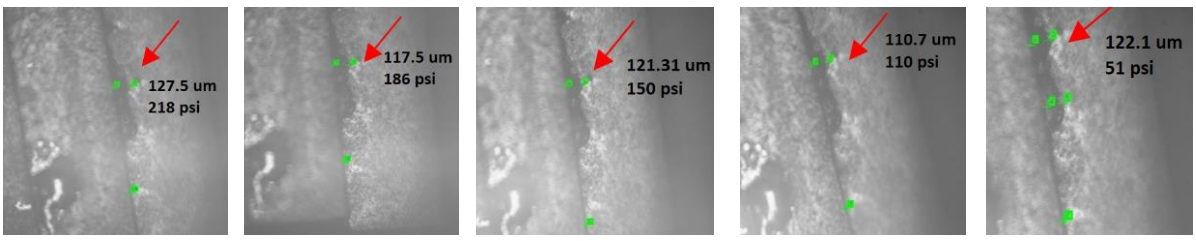

Figure 4-7 Examination of the GaSn middle layer thickness under various levels of uniaxial pressure. The red arrows point to a notch on the AlN to confirm all measurements are done at the same location. The images show that the GaSn layer is stable and that it is not pumped out along the edge of the solid layers.

The response of the sandwich structure to a tensile force was also examined. Again, four sandwich structures, identical to those examined previously, were formed. Two of the samples were formed with uniaxial pressing (UP) and two with cold isostatic pressing (CIP). For these measurements, an extension spring was attached to the upper AlN surface of each sample. A tensile force was then applied to each sample, and the force required to remove the top AlN layer was recorded. Each sample was tested with a spring of different thickness as shown in Table 4-1. These measurements showed that the samples formed with isostatic pressing required an order of magnitude greater force for the top AlN layer to be removed.

Test Number	Stiffness in N/mm	Deformation in mm	Force in N	Pressure in psi
UP #1	0.12	1.1	0.14	0.35
UP #2	0.43	1.4	0.18	0.46
CIP #1	0.06	62.1	3.79	5.50
CIP #2	0.94	3.4	3.42	4.96

Table 4-1 Tensile force required to remove the top layer of AlN from the sandwich structure. Two of the samples were formed with uniaxial pressing (UP), and the other two were formed with cold isostatic pressing (CIP).

To examine possible thermal degradation for these sandwich structures, several temperature stages ranging from 100 °C to 600 °C were tested. The first stage was tested at 100 °C using a two-layer AlN-GaSn sandwich and a three-layer AlN-GaSn sandwich, both

made by the CIP method. Figure 4-8 shows a schematic diagram and the thermal treatment test results for up to 30 hours.

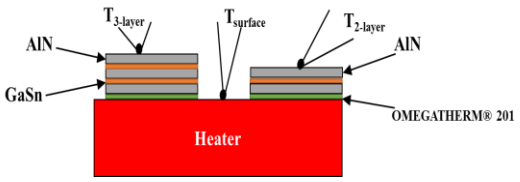

(a)

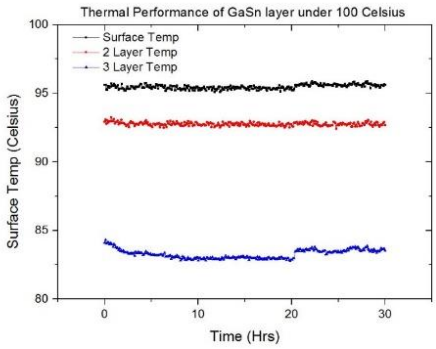

(b)

Figure 4-8 (a) Schematic diagram of the test structure to examine the thermal stability of the GaSn interface layer in a 100 °C environment. Temperatures are measured at the surface of the heaters as well as the surfaces of the two-layer and three-layer structures. (b) Surface temperature readings for the duration of the 30 hour test. The results indicate that the interfaces were stable throughout the test period.

The surface temperature measurements shown in Figure 4-8 for both the two-layer and three-layer structures remained constant for the 30-hour test. Thus, we conclude that the GaSn liquid metal layer remains stable for the duration of the test.

In addition to the measurements at 100 °C, performance at higher temperatures was examined using the setup shown in Figure 4-3(b) for both an AlN-GaSn-AlN structure and an AlN-GaSn-Inconel structure. Figure 4-9 shows the surface temperature of both structures for an environmental temperature of 500 °C for durations of up to 12 hours in air. Considering that

AlN has larger thermal conductivity than Inconel, the temperature at the surface of the AlN structures is expected to be greater than the temperature at the Inconel surface.

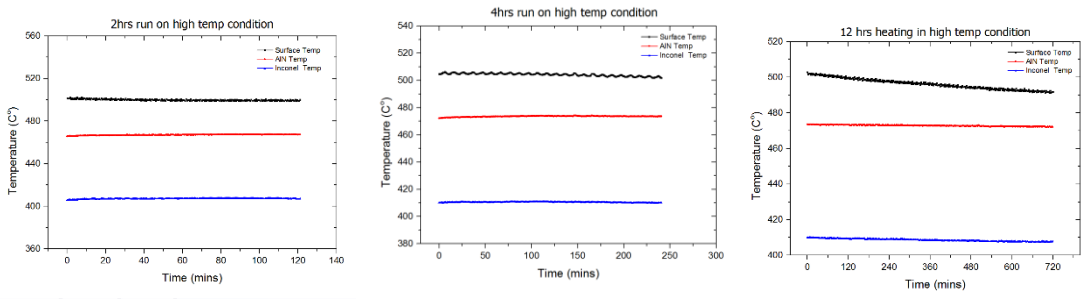

(a) **(b)** **(c)**

Figure 4-9 Surface temperature profile of AlN and Inconel structures for heater temperatures of 500 °C in air. Again, the temperatures are roughly constant throughout each test indicating that the interfaces are stable.

One final thermal test was performed at 600 °C in the bell jar with the pressure reduced to about 0.3 atmospheres. Figure 4-10 displays the surface temperatures on the AlN and Inconel structures when the environment temperature was maintained at 600 °C for 48 hours. Once again, both surface temperatures were constant throughout the test, indicating reliable thermal performance of the GaSn liquid metal interface.

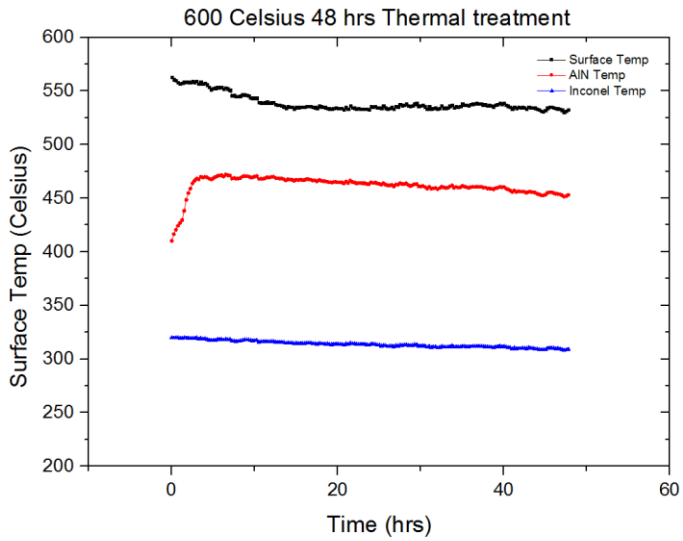

Figure 4-10 Surface temperatures of the AlN and Inconel structures in a low-pressure (0.3atm) environment kept at 600 °C for 48 hours.

Although the surface temperatures of both structures remained constant, the morphology of the liquid metal on the surface was also examined to determine if the high temperature test had any further effect on the GaSn layer. Figure 4-11 displays the morphology of the GaSn on an AlN sample before any thermal treatments.

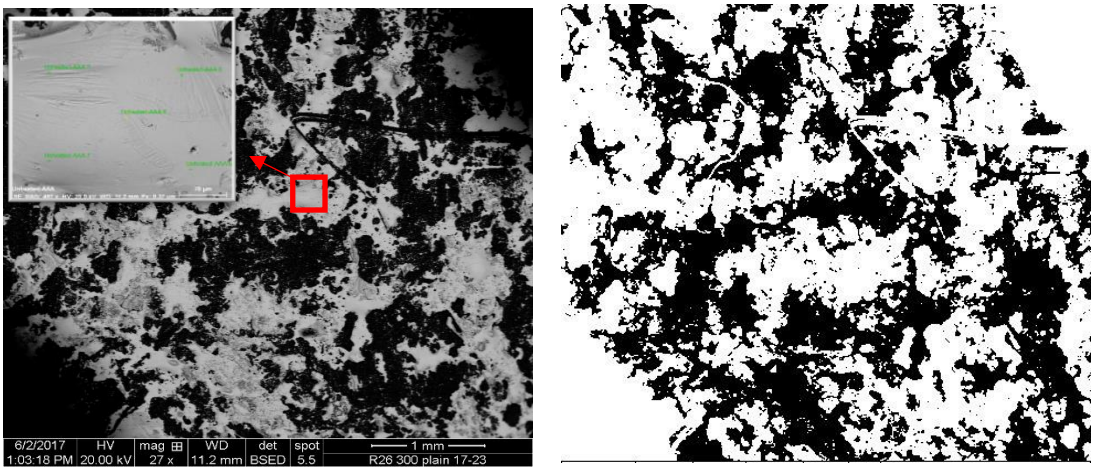

(a) **(b)**

Figure 4-11 (a) SEM image of a GaSn layer on an unheated AlN sample. The inset shows the region chosen for EDS analysis. (b) The area coverage calculation was done by transferring the original SEM image to this black and white image.

Two factors could influence the thermal performance of the GaSn interface layer in this application: 1) the effective coverage of area of liquid metal on the AlN piece; or 2) the composition of the layer could change with time and heating. The composition of the liquid GaSn layer was examined with EDS and the results are shown in Table 4-2.

Sampled Points	Gallium at%	Sn at%
1	93.68	6.32
2	93.98	6.02
3	92.39	7.61
4	94.46	5.54
5	94.46	5.73
Mean Value	**94.27**	**5.73**
Average Coverage of Area	41.1%	

Table 4-2 EDS analysis of a sampled area of GaSn on an unheated AlN sample along with the calculated area coverage of the liquid metal layer.

In comparison of the composition from the expected values given by the manufacturer (92% gallium and 8% tin), the analyzed composition is 94.27% gallium and 5.73% tin, which is reasonably close. With the use of image processing software, the effective coverage of the liquid layer was calculated as 41.1% for the region shown in Figure 4-11. It should be noted that this percentage was calculated after the removal of the first layer of AlN, thus the actual coverage area might be somewhat larger than the calculated results.

Figure 4-12 contains SEM images of the GaSn layer on AlN sample after thermal treatment at 600 °C for 48 hours. The effective area coverage slightly increased to 53.7%. This increase

could be due to thermal expansion during heating, or it could just be a random fluctuation introduced by the removal of the top AlN layer. The EDS analysis in Table 4-3 showed a different picture than the measurements done prior to heating. Silver from the silver paste used to attach the structures to the heater became a large source of contamination for some of the points measured. Additionally, the EDX analysis also documented the presence of oxygen at one location resulting from oxidation. Despite these changes, the thermal performance remained constant throughout the heating process.

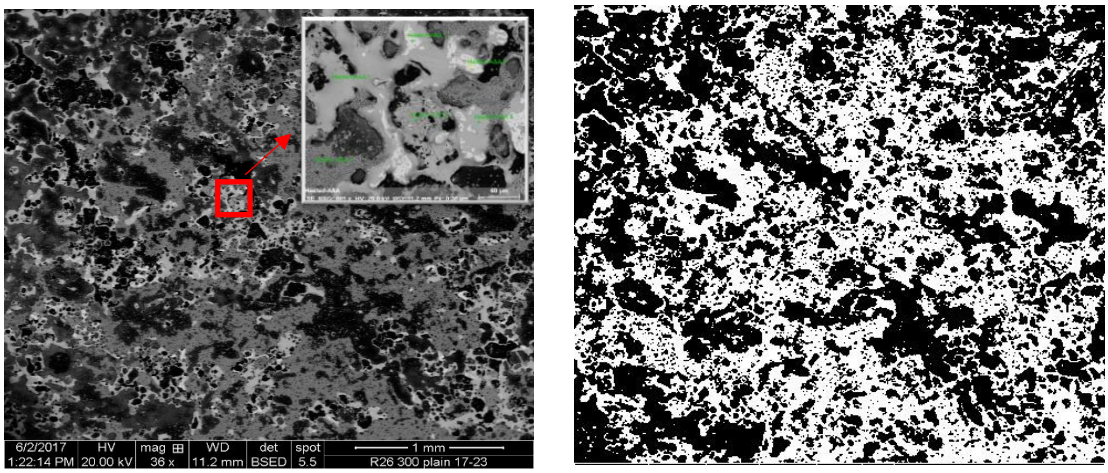

(a) **(b)**

Figure 4-12 (a) SEM image of a GaSn layer on AlN sample after heating. The inset shows the region examined with EDS. (b) The area coverage calculation was done by transferring the original SEM image to this black and white image.

Sampled Points	Ga at%	Sn at%	O at%	Ag at%
1	93.09	6.91	*NA*	*NA*
5	93.75	6.25	*NA*	*NA*
3	29.13	0.90	*NA*	69.97
6	30.61	1.01	*NA*	68.39
2	47.72	1.14	51.14	*NA*
4	52.52	3.04	*NA*	44.44
Area Coverage	**53.7%**			

Table 4-3 EDS analysis of a sampled area of GaSn on a heated AlN sample along with the calculated area coverage of the liquid metal layer.

A similar analysis process was applied to a GaSn layer on an Inconel sample before and after heating at 600 °C for 48 hours. Figure 4-13 describes the morphology of the liquid metal layer before and after thermal treatment and the related black and white images used for the area coverage calculations. A relatively constant coverage area before and after the thermal treatment (75.2% vs 69.4%) was observed on the Inconel sample. The EDS analysis showed a homogeneous GaSn layer before heating on the Inconel as well (93.85% gallium and 6.15% tin). However, the composition changed greatly after heating as shown in Table 4-4. Severe oxidation contamination was observed throughout the sampled area as well as silver contamination from the silver paste.

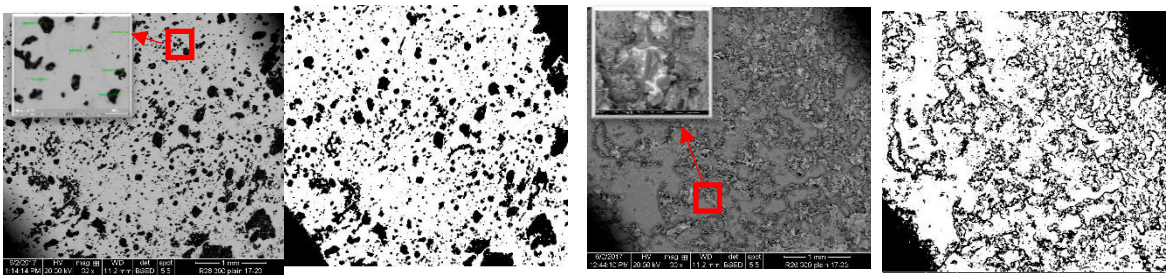

(a) **(b)** **(c)** **(d)**

Figure 4-13 (a) SEM image of the morphology of GaSn on unheated Inconel sample, (b) black and white contrast image of the covered area of the unheated Inconel sample, (c) SEM image of the morphology of GaSn on Inconel after heating, and (d) the related coverage image of the heated Inconel sample.

Sampled Points	O	Cr	Fe	Ni	Ga	Ag	Sn
7	52.12	0.81	*NA*	0.87	11.02	4.78	30.40
8	61.03	4.99	*NA*	2.56	40.88	7.20	13.34
9	43.73	2.03	0.88	2.40	34.91	*NA*	16.05
10	40.65	1.13	*NA*	0.98	24.80	26.30	6.14
11	28.33	4.14	4.00	21.06	42.05	*NA*	0.42
12	24.07	14.62	4.77	25.38	30.12	*NA*	1.03
Coverage	**69.40%**						

Table 4-4 EDS analysis of the Inconel sample after heating at 600 °C for 48 hours. Significant oxidation as well as silver contamination was observed. The total area coverage decreased slightly from 75% to 69.4%.

From the microanalysis above, the survivability of the GaSn liquid metal layer was confirmed before and after the thermal treatment. Though contamination from oxidation and silver diffusion from the silver paste was discovered, the overall thermal performance were not dramatically altered during heating over 48 hours at 600 °C.

In order to understand the role of the GaSn layer and its effective thermal resistance as an interface layer, a physical model was built and analyzed numerically using COMSOL software. According to the setup design shown above, two three-layer structures made of AlN pieces or AlN-Inconel combinations are modeled. In addition, the cartridge heater was included in the modeling as the heating source for the setup.

The model is built on the same scale as in the actual experiments. The AlN and Inconel pieces have dimensions of 10 mm x 10 mm x 0.635 mm. The thickness of the GaSn layer was simplified to be 0.05 mm (50 μm) as a conservative approximation, according to the SEM measurement results. The hot side boundary condition was fixed as a constant temperature of 500 Celsius at the heater surface, which is also accomplished in the experiments. For the heat transfer mechanism, the main heat loss is via convection from the top surface of the structure. All radiative and conduction losses are considered negligible. All of the material properties are from the manufacturer's datasheet and its thermal properties are from related work[93], [94].

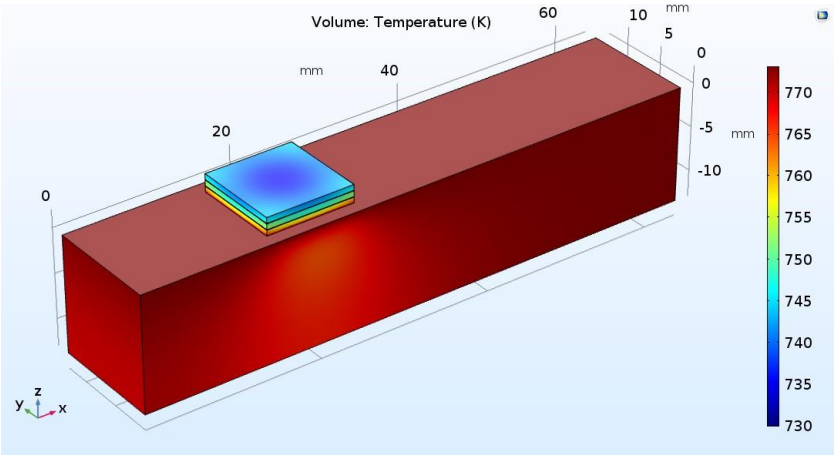

Figure 4-14 Temperature profile of an AlN piece under constant surface temperature 500 Celsius (~773 K) with GaSn as an interface layer.

Figure 4-14 presents the temperature profile of an AlN piece with GaSn as an interface layer. The top surface temperature can be averaged as an indicator to compare with the experimental results. For this model, the top surface average temperature is 740 K, which is essentially identical to the temperature we obtained during the experimental tests.

Location	Top surface	1st AlN top	2nd AlN bottom	2nd AlN top	3rd AlN bottom
Temperature (K)	739.81	748.76	746.75	744.28	742.27
Heat flux (W/m^2)	9.826E5	9.829E5	9.825E5	9.825E5	9.826E5

Table 4-5 Temperature profile at every interface and its heat flux according to simulation results.

With the help of the simulation and its verification with real experimental results, an effective thermal resistance can be obtained using the temperature difference and its flowing heat flux. According to the definition of thermal resistance, $R = \Delta T/q$', the effective thermal

resistance of GaSn interface layer is 2.05×10^{-6} K-m^2/W, which is about 0.49 MW/m^2-K in thermal conductance.

One would expect some difference at the GaSn-Inconel interface when compared with the GaSn-AlN interface, since the wettability and coverage of the GaSn layer is different from AlN to Inconel. An additional thermal contact resistance is required to add into the thermal transport model to consider this change. Similar to the case with three AlN pieces, the AlN-Inconel-AlN structure is also already fulfilled in real experiments, which can be used to modify thermal contact resistance. The simulation results of Figure 4-15 show an average top surface temperature of around 687K, which agrees well with the experimental results of around 683 K.

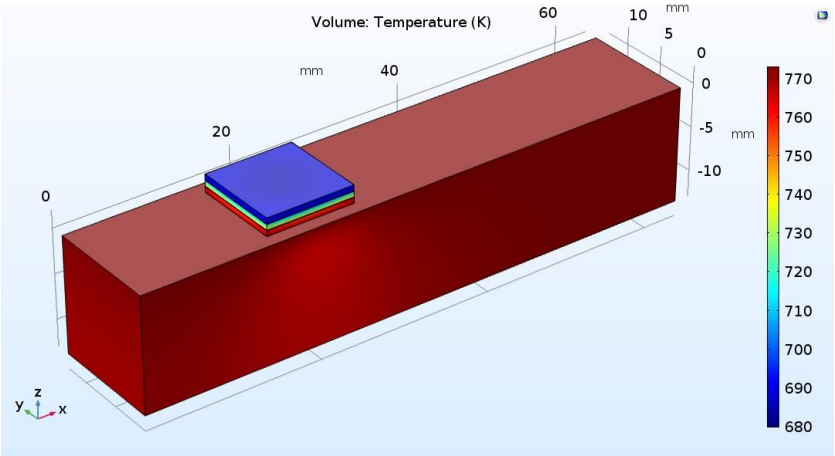

Figure 4-15 Temperature profile of AlN-Inconel structure under 500 Celsius surface temperature

The overall performance improvements can also be verified by comparing the results for the case where the GaSn interface layer is replaced with another kind of thermal paste. OMEGATHERM 201 is a common kind of thermal paste with high thermal conductivity to

connect heat sinks or other solid surfaces. By replacing the GaSn layer with this thermal paste of the same thickness, a lower top surface temperature of 705 K is observed, along with an effective thermal conductance of about 0.05 MW/m^2-K. This great difference proves that the GaSn layer can function as a better thermal interface material to improve the effective thermal conductance. Table 4-6 offers further details regarding the temperature and heat flux when thermal paste is applied as the interface layer.

Location	Top surface	1st AlN top	2nd Inc bottom	2nd Inc top	3rd AlN bottom
Temperature (K)	704.98	748.75	729.14	726.87	707.25
Heat flux (W/m^2)	9.06E5	9.064E5	9.061E5	9.06E5	9.06E5

Table 4-6 Detailed temperature profile at every interface if thermal paste is applied as the interface layer instead of GaSn.

4.4 Conclusion

In this chapter, I examined the performance of liquid GaSn layers for possible use as thermal interface materials in thermoelectric power generation applications up to 600 °C. Compression and tension measurements indicated that structures formed through cold isostatic pressing were more robust and reliable as compared with structures formed with uniaxial pressing. Thermal performance of the GaSn layers was assessed through evaluation of sandwich structures made from AlN and Inconel. These results indicated that the GaSn layers remained stable at temperatures up to 600 °C for up to 48 hours. Further measurements of the

morphology and elemental composition of the GaSn layers suggest that while the coverage of the liquid metal over the solid surface remained relatively constant, oxidation could be an issue, especially for Inconel samples. Thus, while further research is required, in particular for long-term reliability, GaSn appears to be a promising candidate as a high temperature thermal interface material.

Chapter 5 Summary and Future Work

5.1 Summary and conclusions

Thermoelectric devices, which can directly convert thermal energy into electricity without moving mechanical parts, enables a possible solution for waste heat recovery. Thus, thermoelectric devices and their related thermoelectric materials are receiving increasing interest today due, in large part, to the urgent need for clean, renewable energy resources. To model, build and fabricate a successful thermoelectric generator, the first requirement is a high-performance thermoelectric material. Additionally, in order to optimize the thermoelectric device, the module must be well designed which included minimizing the thermal resistance of its packaging and connections to the heat exchangers.

The significant contributions of this dissertation include addressing several key steps towards the design, evaluation, and fabrication of thermoelectric generators. The design, manufacturing, assembly and calibration of the measurement system for Seebeck coefficient and electrical conductivity enables measurements on a wide range of samples of various shapes and sizes. The design of the thermocouple probes and pin-probe distribution in the van der Pauw method limit the cold-finger effects in the measurements by reducing the heat loss through the measurement probes. By combining the functions of different units, including the use of inert gases for varying environmental conditions, the overall system has great flexibility to perform measurements of both electrical conductivity and Seebeck coefficient on samples of non-standard size and shape. Calibration measurements up to 600 K demonstrated the

accuracy and reliability of the system. While this system is not suitable for measurements above about 600 K, it is useful for rapid evaluation of thermoelectric properties of materials to quickly screen potential candidates for further study.

Full thermoelectric characterization was accomplished with a refinement of the laser flash method and its application into practice for determining thermal conductivity, the final property of interest for. Besides traditional solid thermoelectric materials, I also expanded this method for measurements on porous Cu as well as several wooden materials (white pine and medium density fiberboard).

With the acquisition of two additional thermoelectric characterization systems, ZEM-3 and TC-1200 units from ULVAC, the full capability of characterization of thermoelectric materials was extended to a higher temperature range with great accuracy. With these systems, my collaborators and I developed and characterized multiple kinds of thermoelectric materials including skutterudites for low or moderate temperature ranges, Bi_2Te_3 based materials for low temperatures and cooling applications, half-Heusler alloys for high temperature ranges and Ca-Co-O/ZnO oxides materials for oxidizing environments. A significant increase in the electrical conductivity was observed for most of the new materials, and the final characterization of the thermoelectric figure of merit, *ZT*, demonstrated their potential for becoming good candidates in new thermoelectric devices.

In addition to the design and characterization of thermoelectric materials, the optimization of the actual thermoelectric devices is also critical in order to improve overall device efficiency.

One significant challenge is the unnecessary thermal loss from a heat source to the thermoelectric device in power generation applications. The issue of making reliable and durable thermal contacts at the hot side heat exchanger is especially important and difficult at high temperatures, where thermal expansion and oxidation increase. This work demonstrated that GaSn, a eutectic metal with a low melting temperature is capable to function as interface layer to reduce thermal resistance between the thermoelectric module and the high temperature heat exchanger. The mechanical and thermal behavior of GaSn interface layer were examined under static pressure or high temperature conditions, proving its survivability under high temperature to enhance thermal performance.

5.2 Future work

Based on my current research, there are still some related areas of work that can be further studied. Several suggestions for further exploration are given below.

While the self built system for measurements of Seebeck coefficient and electrical conductivity was shown to be accurate, there are several improvements that could be made. The first improvement is related to the accuracy and sensitivity of the measurement setup. At this moment, the accuracy is largely dependent on the thermal stability and control of the heater and its surrounding setup, which is dependent on the feedback of a PID loop. A further fast-reaction feedback system such as automatic temperature rebalancing will improve the thermal stability of the system for better accuracy. Also, due to the limitation of resources, the atmospheric effects on the measurement procedure are not clearly known yet. Only low vacuum

and air conditions were tested so more options as nitrogen and helium were left open to further study.

For the development of novel thermoelectric materials, one suggestion is to incorporate more theoretical modeling into the fabrication of raw materials. Finding suitable combinations of materials from periodic tables is a time-consuming and arduous task for material development. With the fast development of artificial intelligence, more screening tools are available today for material researchers to rapidly investigate more candidate materials. Gaultois[95] proposed web-based machine learning models for screening of thermoelectric materials. To expand this thought, more complex theoretical calculation models can be included into the knowledgebase of AI and, with sufficient time, a more optimized experimental route to sintering processes can be proposed and supported by numerous calculations, which will greatly reduce the time and design cycle for developing new thermoelectric materials.

As for the building of thermoelectric generators with GaSn interface layers, a more practical model is needed to test the role of GaSn in actual applications, especially over the long term to the effects of extreme environments. The lab environmental conditions are close to ideal, and they are far from the environments encountered in practical use of thermoelectric devices, especially for those in unmaintained conditions. A further study regarding the evaluation of GaSn in actual thermoelectric devices will be vital for the further development of GaSn interface layers towards their ultimate use in applications.

Appendix A Uncertainty calculation of Seebeck coefficient and electrical conductivity

The uncertainty calculation can be divided into two parts: The uncertainty analysis for the van der Pauw method and the uncertainty calculation in the Seebeck coefficient measurement. The following sections briefly illustrate the calculation process that derives the final uncertainty in both resistivity and Seebeck coefficient measurements.

A.1 Resistivity uncertainty calculation

For the van der Pauw method, the electrical resistivity is determined by $\rho = R_s \cdot d$, where R_s is the surface resistance, and d is the thickness. According to the propagation of uncertainty, for independent measurement of R_s and d , the uncertainty is expressed as the following:

$$\frac{\sigma_\rho}{\rho} \approx \sqrt{(\frac{\sigma_{R_s}}{R_s})^2 + (\frac{\sigma_d}{d})^2} \quad \text{(A-1)}$$

Then the uncertainty analysis for the disk shape of Monel samples will be used as an example for uncertainty calculation.

For the measurement of thickness d, the uncertainty mainly comes from the resolution of the calipers used in the measurement, which, in this case, is 0.01 mm. For a typical sample used in the experimental setup, the minimum thickness is 1.62 mm. So for this part of the uncertainty, $\frac{\sigma_d}{d} = \frac{0.01}{1.62} \approx 0.62\%$.

For the measurement of surface resistance, R_s, there is more complexity in the analysis. First of all, R_s is calculated by the LabVIEW program using the inputs of $R_{horizontal}$ and $R_{vertical}$, which is necessary for the van der Pauw method. For the numerical iteration itself, the error of limit can be set and decided as $\varepsilon = 0.05\%$. That will be the first source of error to add into the total $\frac{\sigma_{R_s}}{R_s}$. Van der Pauw[48] estimated the uncertainty brought by the probe spacing and length of probes for disk shape. In our practice, the electrical probe contacts are also placed mutually close to 90° apart as needed. As mentioned previously, three pin probes and one thermocouple wire probe are applied in the measurement. Since the pin probes are small enough in diameter and also flexible to place on the edge, the introduction of error will primarily come from the thermocouple wire probe. The diameter of thermocouple wire is 255 μm, equipped with a mullite tube having an outer diameter of around 1.6 mm, the maximum contact length will be the outer diameter (OD) of the tube, which is φ = *1.6 mm*. For the probe spacing, the thermocouple wire probe will be placed as close as to the edge. However, a distance of *l* = *OD* cannot be avoided in real cases. By applying the probe diameter and distance into the error estimation formula that Van der Pauw[48] gave, along with the consideration of largest error, which leads to the minimum diameter that being used in calibration of 9.06 mm.

For one of the contacts that has a length φ along the periphery, the relative error is calculated as:

$$\frac{\Delta\rho}{\rho} \approx -\frac{\varphi^2}{16D^2 \ln 2} \tag{A-2}$$

If the contacts had a length φ perpendicular to the periphery:

$$\frac{\Delta\rho}{\rho} \approx -\frac{\varphi^2}{4D^2 \ln 2} \tag{A-3}$$

Also with one of the contacts, assuming a point, is situated at a distance l from the periphery:

$$\frac{\Delta\rho}{\rho} \approx -\frac{l^2}{2D^2 \ln 2} \tag{A-4}$$

Then insert the values into the error calculation using φ, l and D as noted before. The relative error is then calculated as 0.25%, 1.12%, and 2.25%, respectively. So the total relative error that results from the probe size and placement will be the combination of these three values, i.e. 2.5%.

The other error source comes from the DAQ system, both from the voltage measurements and the current supply. For the Keithley 2182A nanovoltmeter, it specifies a two year accuracy of 40 ppm (reading) + 0.5 μV. To further apply this error range to the normal reading of voltage output, the relative error is about 2.5% (for a minimum reading around 20 μV). Also for the Keithley 6220 precision current source, it specifies one year of accuracy of 1.5% in our setup application range. So the total relative error contribution from DAQ system is about 2.9%.

The third source is from the effect of the thickness of the samples. For the disk shaped samples we used, the largest thickness is 2.12 mm with a uniform diameter of 9.06 mm. Kasl and Hoch[61] gave a correction factor for finite sample thickness samples. In this case, we have

the largest ratio of thickness to diameter of 0.24, which leads to 1.3% as the relative error in this source.

To combine all of these error sources for the R_s measurement, also adding the error introduced by $\frac{\sigma_d}{d}$, the total relative error for the disk shaped Monel sample series are calculated as:

$$\frac{\sigma_\rho}{\rho} \approx \sqrt{(\frac{\sigma_{R_s}}{R_s})^2 + (\frac{\sigma_d}{d})^2} = \sqrt{(\frac{\sigma_{numerical}}{R_s})^2 + (\frac{\sigma_d}{d})^2 + (\frac{\sigma_{spacing}}{R_s})^2 + (\frac{\sigma_{DAQ}}{R_s})^2 + (\frac{\sigma_{thickness}}{R_s})^2} = 4.12\%$$

A.2 Seebeck uncertainty calculation

A similar derivation process can be applied for the determination of the uncertainty in the Seebeck coefficient. The first large contribution will be from the wire Seebeck variation. In the setup, we use a Type-K thermocouple, consisting of Chromel and Alumel. For reading the Seebeck value from the Alumel side, the total Seebeck value is calculated by adding:

$$S_{total} = S_{measured} + S_a \tag{A-5}$$

For the Alumel Seebeck, the accuracy is around 5% of noted numbers, at around – 24 μV/K. So for a total contribution around 200 μV/K, this part of the uncertainty will be around $\left|\frac{5\% \times 24}{200}\right| \approx 0.6\%$.

The second large error source will be the reading of the combination of absolute temperature and its related voltage. According to the K-type thermocouple's characteristics for error limits, in the temperature range used in this work, the relative errors can be regarded as

standard limits of error of 0.75%. Then the DAQ voltage reading, similar to that in the uncertainty analysis for resistivity, will be around 2.5% as well for voltage reading separately. To apply this error in to the propagation of error, the total error resulting from this part will be:

$$\frac{\sigma_{total_{DAQ}}}{S_{measured}} = \sqrt{(2.5\%)^2 + (0.75\%)^2} = 2.61\%$$

The third error source is inevitably resulting from the cold-finger effect discussed previously. The probe-to-probe temperature difference can be obtained as a function of ambient temperature, so the maximum uncertainty will be at a higher temperature set point. Mackey[62] plotted this cold-finger effect uncertainty with the change of ambient temperature and at around 600 K, which is the maximum temperature point in our setup, the uncertainty contribution is around 5.25%.

The last error source will be the statistical variation error from the curve fitting data. This part a fixed 5% is used for general evaluation of the total error. Adding all these effects into the final evaluation of the uncertainty, the maximum total uncertainty will be:

$$\frac{\sigma_S}{S} = \sqrt{(\frac{\sigma_{DAQ}}{S_{measured}})^2 + (\frac{\sigma_{cold-finger}}{S_{measured}})^2 + (\frac{\sigma_{stat}}{S_{measured}})^2} + \frac{\sigma_{S_a}}{S_a} = 8.3\% .$$

Appendix B Round robin calibration with ORNL of bismuth telluride

This round robin test is a blind test with Oak Ridge National Lab, scheduled April 2017, in order to verify the system accuracy of Seebeck and electrical conductivity measurement. The test includes the measurement of Seebeck coefficient, electrical conductivity and thermal diffusivity of a widely distributed Bi_2Te_3 material.

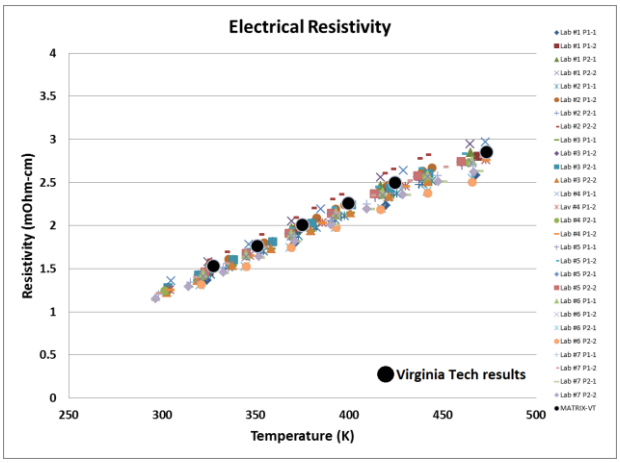

Figure B-1 Comparison of measured electrical conductivity values with other labs results. The large black dots are data from this work.

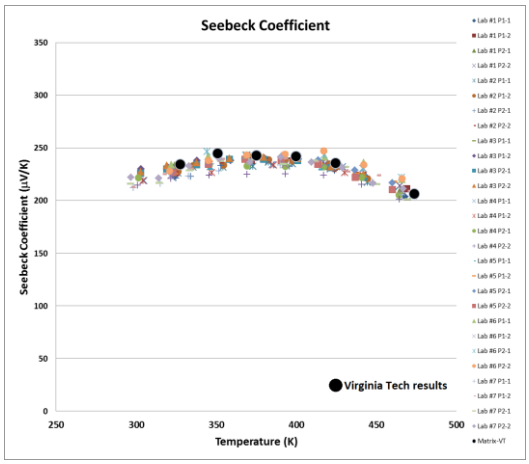

Figure B-2 Comparison of measured Seebeck coefficients with other labs results. The large black dots are data from this work.

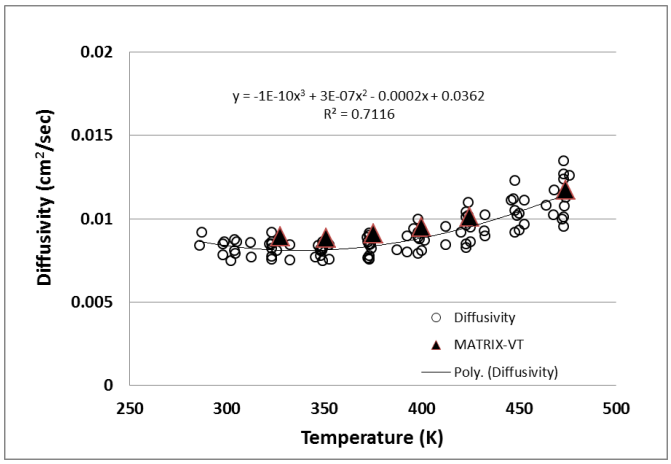

Figure B-3 Comparison of measured thermal diffusivity values. The large triangles are data from this work.

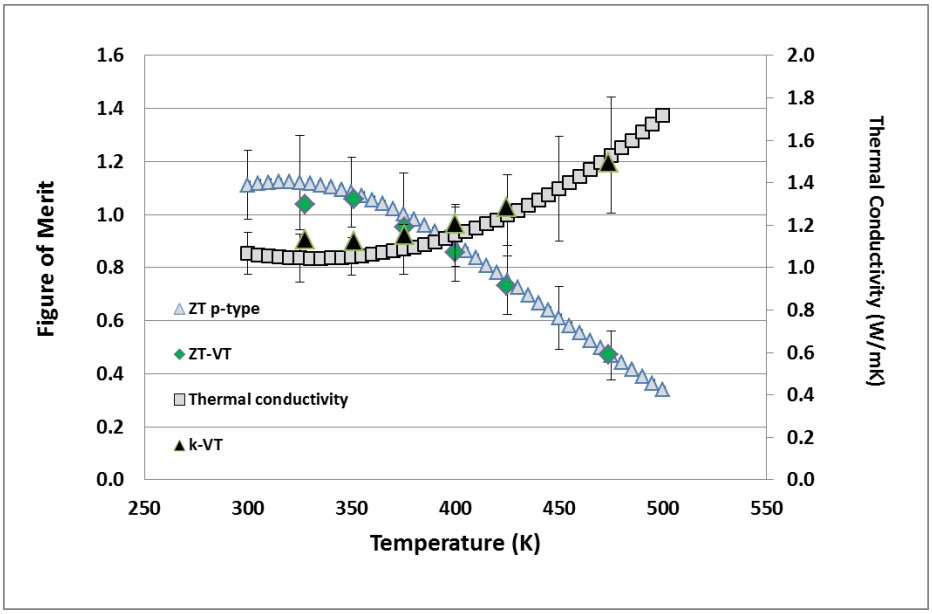

Figure B-4 Final calibration of thermal conductivity and *ZT*.

The overall calibration data is measured from one time test, which demonstrates the measurement accuracy for unknown properties sample in a single test.

Appendix C Sample preparation and testing procedure for ZEM-3 and TC-1200

Different from the self-designed thermoelectric properties characterization system, for the ZEM-3 and TC-1200 systems, the sample preparation work and routine systematic check of the measurements is necessary for maintaining high accuracy of these systems. This part will separately discuss the sample preparation, testing procedure and routine maintenance for both systems.

For ZEM-3 system, one preparation step before the measurement is to ensure the measurement atmosphere is suitable. The purity of the helium used in the tests will greatly affect the performance accuracy, especially in high temperature range when small temperature differences are used. The minimum requirement for helium purity is high purity grade, with the grade being 4.8, which means 99.998% purity and recommended purity is 5.0 UHP level. Then the sample dimension should be controlled to be around 2.0 × 2.0 × 16.0 mm. A larger cross section of the sample will provide more stable contacts between probes and sample surfaces. For the measurement of electrical conductivity, a 16.0 mm length should be necessary since around 3.0 mm current diffusion area should be kept at both ends of the material to allow fully and average distribution flow of current, plus the designated probe distances of 6.00/8.00 mm. A probe distance of 8.00 mm is recommended for samples that are sufficiently long since larger probe distances will naturally come up with larger temperature differences, providing a higher signal to noise ratio. The sample should be well polished with decently smooth surface, cleaned

with isopropyl alcohol (IPA) and acetone, then gently flushed using distilled water and dried for measurement. The electrodes are equipped with wire-wound heaters for the creation of local temperature differences so both thermal and electrical contacts for the electrodes are vital. A similar cleaning process is also necessary for both electrodes and the usage of a polishing pad to remove leftover residues are required. Gently polish the electrode surface using a green polishing pad or sandpaper (800 or 1200 grit) at a 45-degree angle to remove these. To ensure good condition for the probes, the probes should appear as shiny and metallic. Otherwise, use similar polishing methods to remove tip residues.

Also, when placing the probes on the sample, it is recommended to use a thin sheet of graphite foil as a diffusion barrier. Practical experience revealed some highly active sample surfaces. Some thermally unstable samples will promptly diffusive some elements into the probe tip, leading to irremovable connection between the probe tips and sample thus destroying the tip. For high temperature applications above 750 K, the graphite sheet (a Panasonic PGS 50 μm thickness version is currently in use) should be regarded as a requirement. During the measurement process, the *V-I* curve can be used to detect contact quality by its linearity. When a smooth and linear *V-I* curve is observed at the initial test, the sample is ready for heating.

For the TC-1200 thermal diffusivity measurement system, the sample has a quite strict dimension requirement of a diameter 10 mm with thickness around 1.0 mm. The better the roundness of disk shape sample, the better accuracy can be expected. The sample should have uniform thickness of around 1.0 mm in order to give the maximum resolution of the time

responses. Both sides of the sample need to be painted black using graphite spray and dried out before use. A uniform, flat graphite layer will ensure the laser energy is fully absorbed on the top surface and will also give a smooth time response curve reading from the backside. Two insulating glass caps are responsible for holding the atmosphere in the heating chamber in the TC-1200 so it is recommended to clean both of the caps every time before performing measurements. The thermocouples can be annealed to the back side of the samples and connected to the loose end separately to provide a measurement of the actual temperature rise at the backside. By reading the actual temperature rise at backside, the specific heat value can be obtained by knowing the mass, the laser pulse energy, and maximum temperature rise.

References

[1] D. Zhao and G. Tan, “A review of thermoelectric cooling: Materials, modeling and applications,” *Appl. Therm. Eng.*, vol. 66, no. 1–2, pp. 15–24, 2014.

[2] J. Yang and T. Caillat, “Thermoelectric Materials for Space and Automotive Power Generation,” *MRS Bull.*, vol. 31, no. 3, pp. 224–229, 2006.

[3] B. A. Cook, T. E. Chan, G. Dezsi, P. Thomas, C. C. Koch, J. Poon, T. Tritt, and R. Venkatasubramanian, “High-Performance Three-Stage Cascade Thermoelectric Devices with 20% Efficiency,” *J. Electron. Mater.*, vol. 44, no. 6, pp. 1936–1942, 2015.

[4] Y. Zhao, J. Wang, S. Huxtable, G. A. Khodaparast, and S. Priya, “Role of Sintering Atmosphere and Synthesis Parameters on Electrical Conductivity of ZnO,” *Energy Harvest. Syst.*, vol. 0, no. 0, 2015.

[5] X. Hu, P. Jood, M. Ohta, M. Kunii, K. Nagase, H. Nishiate, M. G. Kanatzidis, and A. Yamamoto, “Power generation from nanostructured PbTe-based thermoelectrics: comprehensive development from materials to modules,” *Energy Environ. Sci.*, vol. 9, pp. 517–529, 2015.

[6] S. Wang, J. R. Salvador, J. Yang, P. Wei, B. Duan, and J. Yang, “High-performance n-type YbxCo4Sb12: from partially filled skutterudites towards composite thermoelectrics,” *NPG Asia Mater.*, vol. 8, no. 7, p. e285, 2016.

[7] D. M. Rowe, *CRC Handbook of Thermoelectrics*. CRC Press, 2010.

[8] S. T. J., “Ueber die magnetische Polarisation der Metalle und Erze durch Temperaturdifferenz,” *Ann. Phys.*, vol. 82, no. 3, pp. 253–286, Mar. 2006.

[9] T. Cinquante-Sixsieme, *Annales de chimie et de physique, Volume 56 (Google eBook)*, no. v. 56. 1834.

[10] H. Wang, W. D. Porter, H. Böttner, J. König, L. Chen, S. Bai, T. M. Tritt, A. Mayolet, J. Senawiratne, C. Smith, F. Harris, P. Gilbert, J. W. Sharp, J. Lo, H. Kleinke, and L. Kiss, "Transport Properties of Bulk Thermoelectrics—An International Round-Robin Study, Part I: Seebeck Coefficient and Electrical Resistivity," *J. Electron. Mater.*, vol. 42, no. 4, pp. 654–664, 2013.

[11] X. Yan, B. Poudel, Y. Ma, W. S. Liu, G. Joshi, H. Wang, Y. Lan, D. Wang, G. Chen, and Z. F. Ren, "Experimental Studies on Anisotropic Thermoelectric Properties and Structures of n-Type Bi2Te2.7Se0.3," *Nano Lett.*, vol. 10, no. 9, pp. 3373–3378, Sep. 2010.

[12] G. D. Tang, H. H. Guo, T. Yang, D. W. Zhang, X. N. Xu, L. Y. Wang, Z. H. Wang, H. H. Wen, Z. D. Zhang, and Y. W. Du, "Anisotropic thermopower and magnetothermopower in a misfit-layered calcium cobaltite," *Appl. Phys. Lett.*, vol. 98, no. 20, p. 202109, May 2011.

[13] N. D. Lowhorn, W. Wong-Ng, Z.-Q. Lu, J. Martin, M. L. Green, J. E. Bonevich, E. L. Thomas, N. R. Dilley, and J. Sharp, "Development of a Seebeck coefficient Standard Reference Material™," *J. Mater. Res.*, vol. 26, no. 15, pp. 1983–1992, 2011.

[14] J. Martin, T. Tritt, and C. Uher, "High temperature Seebeck coefficient metrology," *J. Appl. Phys.*, vol. 108, no. 12, 2010.

[15] K. A. Borup, J. de Boor, H. Wang, F. Drymiotis, F. Gascoin, X. Shi, L. Chen, M. I. Fedorov, E. Müller, B. B. Iversen, and G. J. Snyder, "Measuring thermoelectric transport properties of materials," *Energy Environ. Sci.*, vol. 8, no. 2, pp. 423–435, 2015.

[16] J. H. Dennis, "Anisotropy of the seebeck coefficients of bismuth telluride," *Adv. Energy Convers.*, vol. 1, pp. 99–105, Jan. 1961.

[17] L. E. Shelimova, T. E. Svechnikova, P. P. Konstantinov, O. G. Karpinskii, E. S. Avilov, M. A. Kretova, and V. S. Zemskov, "Anisotropic thermoelectric properties of the layered

compounds PbSb2Te4 and PbBi4Te7 ," *Inorg. Mater.*, vol. 43, no. 2, pp. 125–131, 2007.

[18] B. Poudel, Q. Hao, Y. Ma, Y. Lan, A. Minnich, B. Yu, X. Yan, D. Wang, A. Muto, D. Vashaee, X. Chen, J. Liu, M. S. Dresselhaus, G. Chen, and Z. Ren, "High-Thermoelectric Performance of Nanostructured Bismuth Antimony Telluride Bulk Alloys," *Science (80-.).*, vol. 320, no. 5876, p. 634 LP-638, May 2008.

[19] Y. Q. Cao, X. B. Zhao, T. J. Zhu, X. B. Zhang, and J. P. Tu, "Syntheses and thermoelectric properties of Bi2Te3/Sb2Te3 bulk nanocomposites with laminated nanostructure," *Appl. Phys. Lett.*, vol. 92, no. 14, p. 143106, Apr. 2008.

[20] D. Wu, L.-D. Zhao, S. Hao, Q. Jiang, F. Zheng, J. W. Doak, H. Wu, H. Chi, Y. Gelbstein, C. Uher, C. Wolverton, M. Kanatzidis, and J. He, "Origin of the High Performance in GeTe-Based Thermoelectric Materials upon Bi2Te3 Doping," *J. Am. Chem. Soc.*, vol. 136, no. 32, pp. 11412–11419, Aug. 2014.

[21] X. Shi, J. Yang, J. R. Salvador, M. Chi, J. Y. Cho, H. Wang, S. Bai, J. Yang, W. Zhang, and L. Chen, "Multiple-filled skutterudites: High thermoelectric figure of merit through separately optimizing electrical and thermal transports," *J. Am. Chem. Soc.*, vol. 133, no. 20, pp. 7837–7846, 2011.

[22] G. Rogl, A. Grytsiv, P. Rogl, N. Peranio, E. Bauer, M. Zehetbauer, and O. Eibl, "N-Type skutterudites (R,Ba,Yb)yCo4Sb12 (R = Sr, La, Mm, DD, SrMm, SrDD) approaching ZT ??? 2.0," *Acta Mater.*, vol. 63, pp. 30–43, 2014.

[23] S. Chen and Z. Ren, "Recent progress of half-Heusler for moderate temperature thermoelectric applications," *Mater. Today*, vol. 16, no. 10, pp. 387–395, 2013.

[24] C. Yu, T. J. Zhu, R. Z. Shi, Y. Zhang, X. B. Zhao, and J. He, "High-performance half-Heusler thermoelectric materials Hf1-x ZrxNiSn1-ySby prepared by levitation melting and spark plasma sintering," *Acta Mater.*, vol. 57, no. 9, pp. 2757–2764, 2009.

[25] H. Xie, H. Wang, C. Fu, Y. Liu, G. J. Snyder, X. Zhao, and T. Zhu, "The intrinsic disorder related alloy scattering in ZrNiSn half-Heusler thermoelectric materials," *Sci Rep*, vol. 4, p. 6888, 2014.

[26] Y. Pei, X. Shi, A. LaLonde, H. Wang, L. Chen, and G. J. Snyder, "Convergence of electronic bands for high performance bulk thermoelectrics," *Nature*, vol. 473, no. 7345, pp. 66–69, 2011.

[27] X. Yan, W. Liu, H. H. Wang, S. Chen, J. Shiomi, K. Esfarjani, H. H. Wang, D. Wang, G. Chen, and Z. Ren, "Stronger phonon scattering by larger differences in atomic mass and size in p-type half-Heuslers Hf1−xTixCoSb0.8Sn0.2," *Energy Environ. Sci.*, vol. 5, no. 6, p. 7543, 2012.

[28] K. Koumoto, R. Funahashi, E. Guilmeau, Y. Miyazaki, A. Weidenkaff, Y. Wang, and C. Wan, "Thermoelectric ceramics for energy harvesting," *J. Am. Ceram. Soc.*, vol. 96, no. 1, pp. 1–23, 2013.

[29] F. Sarvar, D. Whalley, and P. Conway, "Thermal Interface Materials - A Review of the State of the Art," *2006 1st Electron. Syst. Technol. Conf.*, vol. 2, pp. 1292–1302, 2006.

[30] D. Dai, Y. Zhou, and J. Liu, "Liquid metal based thermoelectric generation system for waste heat recovery," *Renew. Energy*, vol. 36, no. 12, pp. 3530–3536, 2011.

[31] T. Sakamoto, T. Iida, T. Sekiguchi, Y. Taguchi, N. Hirayama, K. Nishio, and Y. Takanashi, "Selection and Evaluation of Thermal Interface Materials for Reduction of the Thermal Contact Resistance of Thermoelectric Generators," *J. Electron. Mater.*, vol. 43, no. 10, pp. 3792–3800, 2014.

[32] J. P. Gwinn and R. L. Webb, "Performance and testing of thermal interface materials," *Microelectronics J.*, vol. 34, no. 3, pp. 215–222, 2003.

[33] X.-H. Yang, S.-C. Tan, and J. Liu, "Thermal management of Li-ion battery with liquid metal," *Energy Convers. Manag.*, vol. 117, pp. 577–585, 2016.

[34] T. Liu, P. Sen, and C. J. Kim, “Characterization of nontoxic liquid-metal alloy galinstan for applications in microdevices,” *J. Microelectromechanical Syst.*, vol. 21, no. 2, pp. 443–450, 2012.

[35] Y. G. Deng and J. Liu, “Corrosion development between liquid gallium and four typical metal substrates used in chip cooling device,” *Appl. Phys. A Mater. Sci. Process.*, vol. 95, no. 3, pp. 907–915, 2009.

[36] M. M. Sarafraz, A. Arya, F. Hormozi, and V. Nikkhah, “On the convective thermal performance of a CPU cooler working with liquid gallium and CuO/water nanofluid: A comparative study,” *Appl. Therm. Eng.*, vol. 112, pp. 1373–1381, 2017.

[37] C. K. Roy, S. Bhavnani, M. C. Hamilton, R. W. Johnson, J. L. Nguyen, R. W. Knight, and D. K. Harris, “Investigation into the application of low melting temperature alloys as wet thermal interface materials,” *Int. J. Heat Mass Transf.*, vol. 85, pp. 996–1002, 2015.

[38] J. Martin, T. Tritt, and C. Uher, “High temperature Seebeck coefficient metrology,” *J. Appl. Phys.*, vol. 108, no. 12, p. 121101, 2010.

[39] J. Martin, “Apparatus for the high temperature measurement of the Seebeck coefficient in thermoelectric materials,” *Rev Sci Instrum*, vol. 83, no. 6, p. 65101, 2012.

[40] S. Iwanaga, E. S. Toberer, A. LaLonde, and G. J. Snyder, “A high temperature apparatus for measurement of the Seebeck coefficient,” *Rev Sci Instrum*, vol. 82, no. 6, p. 63905, 2011.

[41] L. Abadlia, F. Gasser, K. Khalouk, M. Mayoufi, and J. G. Gasser, “New experimental methodology, setup and LabView program for accurate absolute thermoelectric power and electrical resistivity measurements between 25 and 1600 K: Application to pure copper, platinum, tungsten, and nickel at very high temperatures,” *Rev Sci Instrum*, vol. 85, no. 9, p. 95121, 2014.

[42] Y. Zhou, D. Yang, L. Li, F. Li, and J. F. Li, “Fast Seebeck coefficient measurement based on dynamic method,” *Rev Sci Instrum*, vol. 85, no. 5, p. 54904, 2014.

[43] J. Martin, “Protocols for the high temperature measurement of the Seebeck coefficient in thermoelectric materials,” *Meas. Sci. Technol.*, vol. 24, no. 8, p. 85601, 2013.

[44] C. Wood, A. Chmielewski, and D. Zoltan, “Measurement of Seebeck coefficient using a large thermal gradient,” *Rev. Sci. Instrum.*, vol. 59, no. 6, p. 951, 1988.

[45] S. R. Kumar and S. Kasiviswanathan, “A hot probe setup for the measurement of Seebeck coefficient of thin wires and thin films using integral method,” *Rev Sci Instrum*, vol. 79, no. 2 Pt 1, p. 24302, 2008.

[46] R. J. Korkosz, T. C. Chasapis, S. H. Lo, J. W. Doak, Y. J. Kim, C. I. Wu, E. Hatzikraniotis, T. P. Hogan, D. N. Seidman, C. Wolverton, V. P. Dravid, and M. G. Kanatzidis, “High ZT in p-type (PbTe)1-2x(PbSe)x(PbS)x thermoelectric materials,” *J Am Chem Soc*, vol. 136, no. 8, pp. 3225–3237, 2014.

[47] F. M. Smits, “Measurement of Sheet Resistivities with the Four-Point Probe,” *Bell Syst. Tech. J.*, 1958.

[48] L. J. Van der Pauw, “A method of measuring the resistivity and Hall coefficient on lamellae of arbitrary shape,” *Philips Tech. Rev.*, vol. 20, no. 8, pp. 220–224, 1958.

[49] B. J. Horkstra, L. J. Van der Pauw, and N. V Philips, “Measurement of the Resistivity Constants of Anistotropic Conductors by means of Plane-Parallel Discs of Arbitrary Shape†,” *Int. J. Electron.*, vol. 7, no. 2, pp. 169–171, 1959.

[50] D. W. Koon, “Effect of contact size and placement, and of resistive inhomogeneities on van der Pauw measurements,” *Rev. Sci. Instrum.*, vol. 60, no. 2, p. 271, 1989.

[51] D. W. Koon, A. A. Bahl, and E. O. Duncan, “Measurement of contact placement errors in the van der Pauw technique,” *Rev. Sci. Instrum.*, vol. 60, no. 2, p. 275, 1989.

[52] M. Futamata, “A computer-controlled measurement system for electrical conductivity using the van der Pauw method at various temperatures,” *Meas. Sci. Technol.*, vol. 3, no. 9, pp. 919–921, 1992.

[53] K. A. Borup, E. S. Toberer, L. D. Zoltan, G. Nakatsukasa, M. Errico, J. P. Fleurial, B. B. Iversen, and G. J. Snyder, “Measurement of the electrical resistivity and Hall coefficient at high temperatures,” *Rev Sci Instrum*, vol. 83, no. 12, p. 123902, 2012.

[54] N. D. Lowhorn, W. Wong-Ng, W. Zhang, Z. Q. Lu, M. Otani, E. Thomas, M. Green, T. N. Tran, N. Dilley, S. Ghamaty, N. Elsner, T. Hogan, A. D. Downey, Q. Jie, Q. Li, H. Obara, J. Sharp, C. Caylor, R. Venkatasubramanian, R. Willigan, J. Yang, J. Martin, G. Nolas, B. Edwards, and T. Tritt, “Round-robin measurements of two candidate materials for a Seebeck coefficient Standard Reference Material™,” *Appl. Phys. A*, vol. 94, no. 2, pp. 231–234, 2008.

[55] Z. Q. J. Lu, N. D. Lowhorn, W. Wong-Ng, W. Zhang, E. L. Thomas, M. Otani, M. L. Green, T. N. Tran, C. Caylor, N. R. Dilley, A. Downey, B. Edwards, N. Elsner, S. Ghamaty, T. Hogan, Q. Jie, and Q. Li, “Statistical Analysis of a Round-Robin Measurement Survey of Two Candidate Materials for a Seebeck Coefficient Standard Reference Material,” *J. Res. Natl. Inst. Stand. Technol.*, vol. 114, no. 1, p. 37, 2009.

[56] R. T. Tung, “The physics and chemistry of the Schottky barrier height,” *Appl. Phys. Rev.*, vol. 1, no. 1, p. 11304, Jan. 2014.

[57] R. E. Bentley, *Handbook of Temperature Measurement Vol. 3: The Theory and Practice of Thermoelectric Thermometry*. Springer, 1998.

[58] Y. Zhao, A. Kumar, G. A. Khodaparast, A. Eltahir, H. Wang, and S. Priya, “Sintering Temperature-Dependent Chemical Defects and the Effect on the Electrical Resistivity of Thermoelectric ZnO,” *Energy Harvest. Syst.*, vol. 1, no. 1–2, 2014.

[59] J. D. Weiss, R. J. Kaplar, and K. E. Kambour, “A derivation of the van der Pauw formula

from electrostatics," *Solid. State. Electron.*, vol. 52, no. 1, pp. 91–98, 2008.

[60] "Monel Properties." [Online]. Available: http://www.hightempmetals.com/techdata/hitempMonel400data.php.

[61] C. Kasl and M. J. R. Hoch, "Effects of sample thickness on the van der Pauw technique for resistivity measurements," *Rev. Sci. Instrum.*, vol. 76, no. 3, p. 33907, 2005.

[62] J. Mackey, F. Dynys, and A. Sehirlioglu, "Uncertainty analysis for common Seebeck and electrical resistivity measurement systems," *Rev Sci Instrum*, vol. 85, no. 8, p. 85119, 2014.

[63] W. J. Parker, R. J. Jenkins, C. P. Butler, and G. L. Abbott, "Flash Method of Determining Thermal Diffusivity, Heat Capacity, and Thermal Conductivity," *J. Appl. Phys.*, vol. 32, no. 9, p. 1679, 1961.

[64] I. V Savchenko and S. V Stankus, "Thermal conductivity and thermal diffusivity of tantalum in the temperature range from 293 to 1800 K," *Thermophys. Aeromechanics*, vol. 15, no. 4, pp. 679–682, 2009.

[65] L. A. A. Warnes, *Electronic Materials*. Springer US, 2012.

[66] W. Li, J. Wang, Y. Xie, J. J. Heremans, H.-B. Kang, B. Poudel, and S. T. Huxtable, "High thermoelectric performance by ultra-low thermal conductivity in Yb-single-filed skutterudite," *Manuscr. Submmited Publ.*, 2018.

[67] Y. Wang, J. Mao, Q. Jie, B. Ge, and Z. Ren, "Filling fraction of Yb in $CoSb_3$ Skutterudite studied by electron microscopy," *Appl. Phys. Lett.*, vol. 110, no. 16, p. 163901, 2017.

[68] K.-M. Song, D.-K. Shin, and I.-H. Kim, "Synthesis and thermoelectric properties of double-filled La1−z Nd z Fe4−x Co x Sb12 skutterudites," *J. Korean Phys. Soc.*, vol. 67, no. 9, pp. 1597–1602, 2015.

[69] G. Nolas and J. Cohn, "Effect of partial void filling on the lattice thermal conductivity

of skutterudites," *Phys. Rev. B - Condens. Matter Mater. Phys.*, vol. 58, no. 1, pp. 164–170, 1998.

[70] W. Ren, H. Geng, Z. Zhang, and L. Zhang, "Filling-Fraction Fluctuation Leading to Glasslike Ultralow Thermal Conductivity in Caged Skutterudites," *Phys. Rev. Lett.*, vol. 118, no. 24, pp. 1–6, 2017.

[71] H. Zhang, Y. Wang, K. Dahal, J. Mao, L. Huang, Q. Zhang, and Z. Ren, *Thermoelectric properties of n-type half-Heusler compounds (Hf0.25Zr0.75)1–xNbxNiSn*, vol. 113. 2016.

[72] G. Joshi, R. He, M. Engber, G. Samsonidze, T. Pantha, E. Dahal, K. Dahal, J. Yang, Y. Lan, B. Kozinsky, and Z. Ren, "NbFeSb-based p-type half-Heuslers for power generation applications," *Energy Environ. Sci.*, vol. 7, no. 12, pp. 4070–4076, 2014.

[73] A. Ślebarski, "Electron-correlation effects in a disordered Fe 2 TiSn Heusler alloy," *J. Phys. D. Appl. Phys.*, vol. 39, no. 5, p. 856, 2006.

[74] I. Matsubara, R. Funahashi, T. Takeuchi, S. Sodeoka, T. Shimizu, and K. Ueno, "Fabrication of an all-oxide thermoelectric power generator," *Appl. Phys. Lett.*, vol. 78, no. 23, pp. 3627–3629, 2001.

[75] I. Terasaki, Y. Sasago, and K. Uchinokura, "Large thermoelectric power inNaCo2O4single crystals," *Phys. Rev. B*, vol. 56, no. 20, pp. R12685–R12687, 1997.

[76] K. Koumoto and I. Terasaki, "Complex Oxide Materials for Thermoelectric Applications," *MRS Bull.*, vol. 31, no. March, pp. 206–210, 2006.

[77] J. G. Noudem, D. Kenfaui, D. Chateigner, and M. Gomina, "Toward the enhancement of thermoelectric properties of lamellar Ca3Co4O9 by edge-free spark plasma texturing," *Scr. Mater.*, vol. 66, no. 5, pp. 258–260, 2012.

[78] M. Ohtaki, T. Tsubota, K. Eguchi, and H. Arai, "High-temperature thermoelectric

properties of (Zn1−xAlx)O," *J. Appl. Phys.*, vol. 79, no. 3, p. 1816, 1996.

[79] Y. Kinemuchi, C. Ito, H. Kaga, T. Aoki, and K. Watari, "Thermoelectricity of Al-doped ZnO at different carrier concentrations," *J. Mater. Res.*, vol. 22, no. 07, pp. 1942–1946, 2011.

[80] P. Jood, R. J. Mehta, Y. Zhang, G. Peleckis, X. Wang, R. W. Siegel, T. Borca-Tasciuc, S. X. Dou, and G. Ramanath, "Al-doped zinc oxide nanocomposites with enhanced thermoelectric properties," *Nano Lett*, vol. 11, no. 10, pp. 4337–4342, 2011.

[81] P. Jood, R. J. Mehta, Y. Zhang, T. Borca-Tasciuc, S. X. Dou, D. Singh, and G. Ramanath, "Heavy element doping for enhancing thermoelectric properties of nanostructured zinc oxide," *RSC Adv.*, pp. 6363–6368, 2013.

[82] Y. Yang, W. Guo, K. C. Pradel, G. Zhu, Y. Zhou, Y. Zhang, Y. Hu, L. Lin, and Z. L. Wang, "Pyroelectric nanogenerators for harvesting thermoelectric energy," *Nano Lett*, vol. 12, no. 6, pp. 2833–2838, 2012.

[83] S. Yang, F. Chen, Q. Shen, and L. Zhang, "Microstructure and electrical property of aluminum doped zinc oxide ceramics by isolating current under spark plasma sintering," *J. Eur. Ceram. Soc.*, vol. 36, no. 8, pp. 1953–1959, 2016.

[84] W. Tang and D. C. Cameron, "Aluminum-doped zinc oxide transparent conductors deposited by the sol-gel process," *Thin Solid Films*, vol. 238, no. 1, pp. 83–87, 1994.

[85] Y. TANIGAWA, M. MATSUMOTO, and T. AKAI, "Optimization of Material Composition to Minimize Thermal Stresses in Nonhomogeneous Plate Subjected to Unsteady Heat Supply," *JSME Int. journal. Ser. A, Mech. Mater. Eng.*, vol. 40, no. 1, pp. 84–93, 1997.

[86] A. S. Al-Merbati, B. S. Yilbas, and A. Z. Sahin, "Thermodynamics and thermal stress analysis of thermoelectric power generator: Influence of pin geometry on device performance," *Appl. Therm. Eng.*, vol. 50, no. 1, pp. 683–692, 2013.

[87] S. L. Li, C. K. Liu, C. Y. Hsu, M. C. Hsieh, M. J. Dai, and S. T. Wu, "Thermo-mechanical analysis of thermoelectric modules," in *2010 5th International Microsystems Packaging Assembly and Circuits Technology Conference*, 2010, pp. 1–4.

[88] C. L. Cramer, W. Li, Z.-H. Jin, J. Wang, K. Ma, and T. B. Holland, "Techniques for Mitigating Thermal Fatigue Degradation, Controlling Efficiency, and Extending Lifetime in a ZnO Thermoelectric Using Grain Size Gradient FGMs," *J. Electron. Mater.*, vol. 47, no. 1, pp. 866–872, 2018.

[89] L. D. Zhao, S. H. Lo, Y. Zhang, H. Sun, G. Tan, C. Uher, C. Wolverton, V. P. Dravid, and M. G. Kanatzidis, "Ultralow thermal conductivity and high thermoelectric figure of merit in SnSe crystals," *Nature*, vol. 508, no. 7496, pp. 373–377, 2014.

[90] G. Tan, S. Hao, J. Zhao, C. Wolverton, and M. G. Kanatzidis, "High Thermoelectric Performance in Electron-doped AgBi3S5 with Ultralow Thermal Conductivity," *J. Am. Chem. Soc.*, p. jacs.7b02399, 2017.

[91] J. Lim, H. T. Wang, J. Y. Tang, S. C. Andrews, H. Y. So, J. Lee, D. H. Lee, T. P. Russell, and P. D. Yang, "Simultaneous Thermoelectric Property Measurement and Incoherent Phonon Transport in Holey Silicon," *ACS Nano*, vol. 10, no. 1, pp. 124–132, 2016.

[92] R. Prasher, "Thermal Interface Materials: Historical Perspective, Status, and Future Directions," *Proc. IEEE*, vol. 94, no. 8, pp. 1571–1586, 2006.

[93] Y. Plevachuk, V. Sklyarchuk, S. Eckert, G. Gerbeth, and R. Novakovic, "Thermophysical Properties of the Liquid Ga–In–Sn Eutectic Alloy," *J. Chem. Eng. Data*, vol. 59, no. 3, pp. 757–763, 2014.

[94] Y. Plevachuk, V. Sklyarchuk, N. Shevchenko, and S. Eckert, "Electrophysical and structure-sensitive properties of liquid Ga-In alloys," *Int. J. Mater. Res.*, vol. 106, no. 1, pp. 66–71, Jan. 2015.

[95] M. W. Gaultois, A. O. Oliynyk, A. Mar, T. D. Sparks, G. J. Mulholland, and B. Meredig,

"Perspective: Web-based machine learning models for real-time screening of thermoelectric materials properties," *APL Mater.*, vol. 4, no. 5, p. 053213, 2016.